Institute of Thermoelectricity, Academy of Sciences and Ministry of Education and Science of Ukraine

Journal of THERMOELECTRICITY

International Research

Founded in December, 1993

published 6 times a year

No. 4 *2015*

Editorial Board

Editor-in-Chief LUKYAN I. ANATYCHUK

Petro I. Baransky
Lyudmyla N. Vikhor
Valentyn V. Lysko
Stepan V. Melnychuk
Bogdan I. Stadnyk
Yuri N. Lobunets
Elena I. Rogacheva
Andrey A. Snarskii

International Editorial Board

Lukyan I. Anatychuk, *Ukraine*
Steponas P. Ašmontas, *Lithuania*
Jean-Claude Tedenac, *France*
H.J. Goldsmid, *Australia*
L.P. Bulat, *Russia*
L. Chen, *China*
T. Caillat, *USA*
Yuri Grin, *Germany*
A.I. Casian, *Moldova*
Takenobu Kajikawa, *Japan*
T. Tritt, *USA*
Sergiy O. Filin, *Poland*
M.I. Fedorov, *Russia*
D. Sharp, *USA*
Yuri Gurevich, *Mexico*

Founders – National Academy of Sciences, Ukraine
Institute of Thermoelectricity of National Academy of Sciences and Ministry of Education and Science of Ukraine

Certificate of state registration № КВ 15496-4068 ПР

Editorial office manager O. Pugantseva

Editors:

L. Vikhor, V. Kramar, V. Katerynchuk, O. Luste, A. Farion, O. Bodnaruk

Approved for printing by the Academic Council of Institute of Thermoelectricity of the National Academy of Sciences and Ministry of Education and Science, Ukraine

Address of editorial office:
Ukraine, 58002, Chernivtsi, General Post Office, P.O. Box 86.
Phone: +(380-372) 90 31 65.
Fax: +(380-3722) 4 19 17.
E-mail: jt@inst.cv.ua
http://www.jt.inst.cv.ua

Signed for publication 25.09.15. Format 70×108/16. Offset paper №1. Offset printing.
Printer's sheet 11.5. Publisher's signature 9.2. Circulation 400 copies. Order 5.

Printed from the layout original made by "Journal of Thermoelectricity" editorial board
in the printing house of "Bukrek" publishers,
10, Radischev Str., Chernivtsi, 58000, Ukraine

Copyright © Institute of Thermoelectricity, Academy of Sciences and Ministry of Education and Science, Ukraine, 2015

CONTENTS

General Problems

E. Velmre. Uncovering some hidden pages in the life of thomas johann seebeck 5

Theory

L.N. Vikhor, P.V. Gorskiy. Peculiarities of heat and electric charge transport in "metal-thermoelectric material-metal" miniature layers 10

Material Research

A.A. Nikolaeva, L.A.Konopko, T.E. Huber, A.K.Kobylianskaya, G.I.Para. On the conditions of hifigure of meritand methods of search for promising superlattice thermoelectric materials 19

V.A.Romaka, P.Rogl, L.P.Romaka ,Yu.V.Stadnyk, D. Kaczorowski, V.Ya. Krayovskyy, O.I.Lakh. The study of structural, energy and kinetic characteristics of $Hf_{1-x}Y_xNiSn$ thermoelectric material 30

Technology

S.F. Zaparov Comparative analysis of the efficiency of cutting *Bi*-*Te*-based thermoelectric material using electric erosion method and wires with bound abrasive 39

Design

L.I. Anatychuk, A.V. Prybyla. Optimization of thermal connections in liquid-liquid thermoelectric heat pumps for water purification devices of space application. 44

C.A. Gould, N.Y.A. Shammas, K. Simpson. The modelling and simulation of Bi_2Te_3 thermoelectric generators in synopsys tcad 50

V.Ya.Mykhailovsky., *M.V.Maksimuk* Rational powers of thermal generators for starting pre-heaters of vehicles 66

L.I. Anatychuk, R.V. Kuz, D.D. Taschuk. Differential thermoelectric ac converter in the non-simultaneous comparison mode. 73

Metrology and Standardization

L.I.Anatychuk, M.V.Havrylyuk, V.V.Lysko, V.A.Tyumentsev. Automated equipment for measurement of properties of thermoelectric material rods. 79

Thermoelectric products

R.R.Kobylianskyi, I.A.Moskalyk. The prospects of using thermoelectricity for human head cryotherapy. 85

E Velmre.

E. Velmre.

Tallinn University of Technology, Ehitajate tee 5,
19086 Tallinn, Estonia.

UNCOVERING SOME HIDDEN PAGES IN THE LIFE OF THOMAS JOHANN SEEBECK

Why the long-lasting friendship between Seebeck and Hegel was suddenly interrupted? In what way Goethe was involved in this quarrel? How this conflict influenced Seebeck's further career? Answers to these questions have been found mostly from correspondence of Hegel, Seebeck, Goethe, and their contemporaries.
Key words: Seebeck, Hegel, Goethe.

Introduction

Thomas Johann Seebeck [1, 2], a german-estonian physicist, chemist and physician was born on April 9, 1770 in the Hanseatic town of Reval (now Tallinn). His father Johann Christoph Seebeck, a wealthy merchant, was descending from an old Livonian family with Scandinavian roots. He became a citizen of Tallinn in January 1769, married merchant's daughter Gerdrutha Lohmann and purchased a real estate at the Great Market, today Raekoja plats 4/Dunkri 2. In this house the future scientist was born in 1770. Shortly after graduating from Town Imperial Grammar School (now Tallinn Gustav Adolf Grammar School) at the age of 17, Thomas Johann moved to Germany to study medicine. In 1792, Seebeck passed at Göttingen the final exams in medicine and practical surgery with excellent marks. However, deeply influenced by charismatic professor of physics Georg Christoph Lichtenberg Seebeck decided to devote himself to physics.

In 1795 Seebeck married Juliane Boye and they settled in Bayreuth. Seebeck father's inheritance allowed him to live as an independent private scholar and he did not need to practice as a medical doctor.

Nevertheless, in March 1802, Seebeck received his Dr. Med. degree from the University of Göttingen and in summer Thomas Johann with his wife and six daughters moved to Jena. Later Seebeck lived and worked in Bayreuth, Nuremberg, and Berlin. Thomas Johann Seebeck died in Berlin on December 10, 1831. Only a month earlier, on November 14, 1831, his friend Georg Wilhelm Friedrich Hegel died in Berlin as a victim of a cholera epidemy. Very soon, Johann Wolfgang Goethe, who was a friend both of them died on March 22, 1832 in Weimar.

Seebeck in Jena 1802-1810

In 1802, Seebeck arrived in Jena. His motive was to get acquainted with Schelling and attend his lectures on *Naturphilosophie*. In Jena Seebeck found himself in a very busy intellectual environment. This was a period of transition from the Weimar Classicism to the Preromanticism of Jena. Of course, a central figure of the cultural and social life was Johann Wolfgang Goethe, a great poet and passionate naturalist and researcher. As an influencial administrator at the Court of Weimar

and a personal friend of the Duke of Saxe-Weimar-Eisenach he kindly helped young talents to start their academic career.

At the turn of the 18/19th centuries Goethe's most famous protègès in Jena were:
1789 – F. Schiller (30 years of age), an appointed professor of History and Philosophy;
1798 – F. W. J. Schelling (23), an extraordinary professor of Philosophy of nature;

1801 – G. W. F. Hegel (31), a private docent of German Philosophy and. His inaugural dissertation was „De Orbitis Planetarum“ (Jena, 1801); in 1805/06 – an extraordinary professor of Philosophy without remuneration.

1803 – J. W. Ritter (20) arrived in Jena to study medicine. For a shorter period he, a practically self-taught scholar, collaborated with Goethe and Alexander von Humboldt and in 1803/04 he lectured at the University of Jena. In 1801 Ritter discovered „chemical light“, i.e. the ultraviolett radiation. This discovery was made following the principle of polarity, one of the basic ideas of the Naturphilosophy. Ritter knew that Herschel had recently discovered so-called „thermal light“ beyond the red end of prismatic light and so Ritter expected to find something interesting beyond the violett end of the sunlight spectrum, as well.

Seebeck met Goethe for the first time at a dinner on December 3, 1803. Hegel, at that time a very sociable young man who loved to play cards and drink expensive wines, was also invited. Soon Seebeck's seventh child was born and Hegel and Ritter were among invited godparents. Unfortunately, Seebeck's little son died shortly.

Schelling, entangled in a love affair was forced to leave Jena in 1803. Next year Ritter was elected to the Bavarian Academy of Sciences and he left for Munich. Goethe was seeking a new companion to assist him in his optical studies. Seebeck as a well-educated and experienced researcher was certainly the best choice for Goethe. Their frequent and long-lasting cooperation resulted in many Seebeck's contributions printed in "*Zur Farbenlehre*" (Theory of colors), the most important scholarly work of Goethe.

The battle of Jena/Auerstedt on October 14, 1806 between Napoleonic and Prussian armies ended an idyllic life in the small university town. French canon fire destroyed Hegel's and Seebeck's houses and their common friend bookseller Frommann offered shelter. Under French occupation the university in Jena was temporarily closed and many professors were ejected. Hegel also lost the job. His father's inheritance was spent, and, last but not least, his illegitimate son was born in February. Hegel rushed away to Bamberg. His friend Immanuel Niethammer helped Hegel to find a job as an editor of a local catholic newspaper. However, Seebeck stayed on in Jena to assist Goethe in editing of his book "*Zur Farbenlehre*".

In 1809, Goethe and Hegel urged Seebeck to apply for a vacant professorship of chemistry and technology at the University of Jena. However, Seebeck's refusal was a great disappointment to his friends. Moreover, it came out that Seebeck was not at all seriously interested in teaching, he was expecting to get a position in an Academy. In May 1810 printing of Goethe's *"Zur Farbenlehre"* in 2 volumes [3] was completed successfully, and Seebeck began preparations for leaving. In his letter to Karl Ludwig von Knebel Seebeck wrote that the cost of living has risen so high that it is absolutely necessary to find a cheaper residence. He had soon eight children to maintain – six daughters and two sons. Later on, his sons August and Moritz played a prominent role in German science and education.

Seebeck in Bayreuth 1810 – 1812

Of course, behind of Seebeck's decision to leave Jena was a practical reasoning.

First of all, Seebeck met increasing financial difficulties. Living in Germany Seebeck carried on his father's business through lessees in Estland and Switzerland. However, Napoleonic wars and the Continental Blockade were hindering transit trade to Russia. In May 1811, his tenant in Reval died and Seebeck had to travel to Estland. He spent the whole summer in Reval and Berlin and returned to Bayreuth in November. Very soon, he had to travel to St. Gallen where his lessee of a textile factory was fighting with bad financial difficulties.

Second, Seebeck just needed a rest from Goethe's dominance in order to obtain more freedom and space for his own interests and ideas.

Printing of Goethe's *Zur Farbenlehre* was completed. Seebeck knew that his scientific contribution and practical assistance helped Goethe a lot. But he felt that sometimes Goethe dominated too much and forced upon his speculative theories contradicting to the mainstream physics, i.e. the Newton's optics. Seebeck as an excellent experimental physicist was well informed about the latest achievements of mainstream science and tried to get rid of Goethe's „natural" science.

Seebeck in Nuremberg 1812 – 1819

In July 1812 Seebeck took up residence in Nuremberg, again driven by essential practical considerations.

First of all, Seebeck's sons Moritz and August, both of age 7, were ready to enter to Nuremberg Gymnasium where Hegel was the Rector and Professor of philosophy since 1808.

Second, Nuremberg, in comparison to Bayreuth, was a larger and more secure city and closer to Munich and St. Gallen. It should be noticed that Seebeck was still waiting for an invitation to the Bavarian Academy in Munich. Unfortunately, his dream never came true.

Third, in Nuremberg Seebeck got again a chance to set up a laboratory. In the middle of August 1812 he started experiments which led to discovery of birefringence in annealed and tempered glass [4].

In his letter to Seebeck of 15 January 1813 Goethe proposed to repeat Morichini's experiments in order to verify author's conclusion that violet light can magnetize a steel needle. Seebeck politely rejected Goethe's proposal. He wrote that he is very busy studying light polarization by reflection from a glass plate, an effect discovered a few years ago by French physicist Malus. On the 21th of February 1813, using a polariscope of original construction Seebeck obtained „full entoptic figures", i.e. inference fringes in annealed and tempered glass samples. The term „entoptic" was proposed by Hegel in accordance to the color theory of Goethe which is defining di-, ep-, and paroptic colors depending on conditions of their appearance.

A year later, David Brewster rediscovered the photoelasticity in glass. In 1815, on 26th of December, Seebeck and Brewster shared the French Academy prize (6000 francs) for the best experimental work published between Oct 1, 1813 and Oct 1, 1815. Two Seebeck papers printed in the Schweigger's *Journal für Chemie, Physik und Mineralogie* were submitted to the Academy by François Arago.

In his letter to Goethe of 30 December 1815 Seebeck writes that Vasily Vladimirovich Petrov was elected to the St. Petersburg Academy. Another hope was lost.

On July 30, 1816, Hegel was appointed to the chair of Philosophy at Heidelberg, again by help of Immanuel Niethammer, who at this time was Central Commissioner of Education of Bavaria. Hegel and Niethammer were old friends. For the first time they met in 1784 as schoolmates at the Tübingen Stift. Later on, Niethammer studied und lectured Philosophy in Jena up to 1804.

In the letter to Goethe of 9 September 1816 Seebeck writes that he submitted an application to

Heidelberg university for the professorship of physics. At the same time, his friend physicist Johann Schweigger applied for the membership of Bavarian Academy of Sciences in Munich. Schweigger was elected, but Seebeck – not! Why?

Heinrich Paulus, professor of philosophy and church history at Heidelberg asked Hegel for an opinion of Dr. Seebeck in regard to coming elections at the University. Paulus was interested in what Hegel thinks of Seebeck's character and intellectual abilities considering his possible appointment to the post of professor of physics. At that time Hegel was still living in Nuremberg. Paulus was aware that Hegel and Seebeck have had close and friendly relations for many years. For instance, Seebeck was among godfathers of Hegel's newborn child, whose christen name Thomas Immanuel Christian was combined from the given names of Seebeck, Niethammer, and Hegel's sister Christiane [5].

In a letter of 13 September 1816 Hegel wrote to Paulus that Seebeck "was indeed a fine fellow but not a first-rate thinker"[6]. As a result, Seebeck was not elected. A little-known physicist G. W. Muncke was elected instead of Seebeck.

Later on, Paulus unintentionally revealed Hegel's confidential evluation of Seebeck's intellectual abilities (Hegel used here the word *die Genialität*) and this unpleasant incident broke forever all ties between two friends.

Goethe tried to reconcile the parties. In a letter of 8 July 1817 Goethe wrote to Seebeck and repeated his proposal to start a new research on color theory. However, he added accidentally that "smart and capable" Hegel will also take part. This was too much for Seebeck! He was offended and in his letter of 29 July 1817 Seebeck politely rejected Goethe's proposal. He advised Goethe to arrange his own experiments and publish obtained results independently.

Seebeck in Berlin 1819 – 1831

At long last, on Juni 25, 1818 Seebeck was elected corresponding member of the Berlin Academy for his works on optics. From the 1th of January, 1819 Seebeck was a full member of the Academy and on March 13 1819 Seebeck delivered his first report at a session of the Berlin Academy. His speech, entitled *Ueber die ungleiche Erregung der Wärme im prismatischen Sonnenbilde* covered so far unpublished experimental results from years 1806, 1807, and 1809.

Hegel, succseeding J. G. Fichte as a professor of philosophy moved to Berlin, and on October 22, 1818 he delivered his inaugural lecture at the University of Berlin.

In July 1819 Seebeck's wife and children also moved to Berlin. While traveling through Jena they met Goethe. On December 11, 1819 Seebeck wrote his last letter to Goethe. Now, at last, he was free and open for new challenges.

On July 21, 1820 Oersted published his famous essay *Experiments about the Effects of an Electrical Current on the Magnetic Needl*e [7]. He sent the booklet to many leading scientists and societies in Europe and America. Oersted's discovery opened the door to a new field of science – the electromagnetism.

Seebeck immediately put aside his experiments on optics and began to examine Oersted's findings. And very soon, within a few months Seebeck achieved his most important result – he discovered the "thermomagnetism". On December 14 1820 Seebeck reported for the first time on his discovery to the Berlin Academy. However, his first comprehencive publication on this issue appeared only in 1822 [8]. In November Oersted arrived in Berlin and on December 2, 1822 he writes to his wife that recently he visited Seebeck's laboratory to see his new experiments. In January Oersted was soon in Paris and on March 23, 1823 he reported to the French Academy about Seebeck's discovery

giving physically correct interpretation of the new phenomenon and coining the term "thermoelectricity".

In his letter of 4 April 1823 Oersted writes from Paris to his wife in Copenhagen that Seebeck's discovery is «the most beautiful of the discoveries which have so far grown out of mine» [9].

Acknowledgements

I would like to thank Prof. Dr. L. Anatychuk who encouraged me to undertake this study and to summarize results in an article

References

1. Velmre, E. Thomas Johann Seebeck (1770 – 1831). Proc. of the Estonian Academy of Sciences, vol. 13, 2007, № 4, p. 276 – 282.
2. Velmre, E. Thomas Johann Seebeck and his contribution to the modern science and Technology. Proc. of the 12th Biennial Baltic Electronics Conference. Tallinn University of Technology, 2010, p. 17 – 24.
3. Goethe, J. W. Zur Farbenlehre. Cotta, Tübingen, 1810.
4. Aben, H. On the role of T. J. Seebeck in the discovery of the photoelastic effect in glass. Proc. of the Estonian Academy of Sciences, vol. 13, 2007, № 4, p. 283 – 294.
5. Pinkard, T. Hegel: A Biography. Cambridge University Press, 2001. p. 314.
6. Briefe von und an Hegel: 1813 bis 1822, Eds. J. Hoffmeister and F. Nicolin. Meiner Verlag, 1969, p. 132.
7. Oersted, H. C. Experimenta circa effectum conflictus electrici in acum magneticam. Hafniae, 1820, 4 pages.
8. Seebeck, T. J. Magnetische Polarisation der Metalle und Erze durch Temperatur-Differenz. Abhandlungen der Königlichen Akademie der Wissenschaften in Berlin, Abhandlungen von 1820-21, 1822, p. 289 – 346.
9. Breve fra og til Hans Christian Ørsted. Ed. Mathilde Ørsted. 2 vols. Copenhagen:Th. Linds Forlag, 1870.

Submitted 10.09.2015

L.N. Vikhor

L.N. Vikhor, P.V. Gorskiy

Institute of Thermoelectricity of the NAS and MES
of Ukraine, 1, Nauky Str., Chernivtsi,
58000, Ukraine

P.V. Gorskiy

PECULIARITIES OF HEAT AND ELECTRIC CHARGE TRANSPORT IN “METAL-THERMOELECTRIC MATERIAL-METAL” MINIATURE LAYERS

Phonon thermal conductivity and electric conductivity of miniature thermoelectric structure “metal-thermoelectric material-metal” was calculated. The impact of thickness of thermoelectric material (TEM) layer between metal layers was taken into account. Calculations of thermal conductivity were made in two approximations: constant phonon mean free path and with regard to the frequency dependence of phonon relaxation time with phonon-phonon scattering due to anharmonicity of lattice thermal vibrations. In the latter case, both Umklapp processes and normal processes were considered, capable of modifying electron scattering at the layer boundaries. The electric conductivity was considered with regard to the energy dependence of charge carrier mean free path. By the example of thin layers of $Bi_2Te_{2.7}Se_{0.3}$ *it was shown that with reduction of their thickness to 50μm, lattice thermal conductivity is reduced at most by 1.5%, and electric conductivity – at most by 1% as compared to single crystal. Owing to this, the expected growth of thermoelectric figure of merit when passing from a single crystal to a 50 μm layer does not exceed 0.5%.*

Key words: lattice thermal conductivity, electric conductivity, phonons, charge carriers, relaxation time, normal processes, Umklapp processes.

Introduction

Microminiature thermoelectric modules are based on thin TEM layers contacting with metal layers. In particular, [1] is dedicated to a thermoelectric microcooler with thermoelements 4 μm high. For such microthermoelements, the impact on heat and electric charge transport of charge carrier energy barriers and diffused phonon scattering at the boundary between TEM and metal was investigated. Based on this approach, the electric and thermal resistances of “TEM-metal” boundary were calculated and their impact on the microcooler characteristics was analyzed. However, in this case no account was taken of the impact of TEM layer thickness on its kinetic coefficients due to commensurability with this thickness of charge carrier and phonon mean free paths.

The purpose of the present wok is to analyze the impact of thickness of single crystal TEM layer on its thermal conductivity, electric conductivity and thermoelectric figure of merit. In so doing, with regard to the fact that the object of study is a layered thermoelectric material, we will consider temperature gradient and electric current to be parallel to crystal layer planes.

Lattice thermal conductivity of a thin layer

Thermal conductivity of a single crystal does not depend on its size in cases when it is much in excess of phonon mean free path caused, for instance, by phonon-phonon scattering due to

anharmonicity of lattice thermal vibrations. However, if the thickness of a single crystal layer becomes commensurate with phonon mean free path, the time of phonon path in a layer becomes commensurate with phonon relaxation time caused by phonon-phonon scattering. In this case, the reverse phonon relaxation time, constant or frequency dependent, should be added to the reverse time of their path in the layer, and the resulting relaxation time is reduced essentially. This reduction has to be taken into account in the calculation of lattice thermal conductivity.

When considering lattice thermal conductivity, we will assume acoustic wave front to be flat and parallel to TEM layer planes. Then, by analogy with [2] that studied the impact of phonon scattering at the boundaries of powder spherical particles and their contacts on lattice thermal conductivity in the approximation of constant mean free path of phonons, we obtain the following expression for the ratio of thermal conductivity κ of a plane layer of thickness d_0 to thermal conductivity κ_{mono} of a single crystal:

$$\kappa/\kappa_{mono} = \frac{d_0}{l_{ph}}\ln\left(1+\frac{l_{ph}}{d_0}\right), \tag{1}$$

where phonon mean free path $l_{ph} = 3\kappa_{mono}/c_V\rho v_{\|}$, c_V is the specific heat, ρ is the density, $v_{\|}$ is the sound velocity in layer plane. This formula was derived by averaging the expression for thermal conductivity over all phonon mean free paths in a layer, including the shortest. Formula (1) is different from the expressions obtained in [2] only in the method of averaging over possible phonon mean free paths in a layer with regard to its thickness.

We now consider the lattice thermal conductivity of TEM thin layer with regard to frequency dependence of phonon relaxation time. In this case, by analogy with the results obtained in [2] according to procedure described in [3], the thermal conductivity of a thin layer relative to a single crystal is determined by the following relation:

$$\kappa/\kappa_{mono} = \int_0^1\int_0^1 \frac{x^4\exp(x/\theta)}{[\exp(x/\theta)-1]^2}\left(\frac{k_{\|}^* z}{1+k_{\|}^* Q_{l\|}(x)z} + \frac{2k_{\|}^* z}{1+k_{\|}^* Q_{t\|}(x)z}\right)\mathrm{d}z\mathrm{d}x\left\{\int_0^1 \frac{x^4\exp(x/\theta)}{[\exp(x/\theta)-1]^2}\left(\frac{1}{Q_{l\|}(x)}+\frac{2}{Q_{t\|}(x)}\right)\mathrm{d}x\right\}^{-1}. \tag{2}$$

In this formula, $\theta = T/T_D$, T is the absolute temperature, T_D is the Debye temperature of material. A dimensionless parameter $k_{\|}^*$ is calculated as follows:

$$k_{\|}^* = \frac{d_0\gamma^2\theta}{\rho}\left(\frac{k_B T_D}{\hbar v_{\|}}\right)^4\left(\frac{k_B T_D}{v_{\|}^2}\right), \tag{3}$$

where γ, ρ and $v_{\|}$ are the Gruneisen parameter, density and sound velocity in TEM, respectively, k_B is the Boltzmann constant, the rest of designations are common. Index "$\|$" means that the corresponding parameter is taken in the direction parallel to TEM layer plane. Moreover, frequency polynomials $Q_{l\|}(x)$ and $Q_{t\|}(x)$, respectively, are given by:

$$Q_{l\|}(x) = x^4 + 0.082x, \tag{4}$$

$$Q_{t\|}(x) = (0.082 + 3.125\theta^3)x. \tag{5}$$

These formulae take into account both normal processes and Umklapp processes for the longitudinal (*l*) and transverse (*t*) phonon modes. Component 0.082*x* is responsible for Umklapp processes, the numerical coefficient being selected such as to assure matching of theoretical and experimental thermal conductivity values for material based on bismuth telluride in the temperature range 100 to -600K [4] with regard to contribution of electron thermal conductivity to full thermal conductivity. It was also taken into account that phonon scattering due to normal processes takes place differently for the longitudinal and transverse modes, as described by other components in (4), (5).

Calculation of lattice thermal conductivity of a thin layer was done by the example of $Bi_2Te_{2.7}Se_{0.3}$ material with the following parameters: $\gamma = 1.5$ [4], $\rho = 6854\,\text{kg/m}^3$ [1], T_D=157K [5], $v_{\|} = 2900\,\text{m/s}$ [1]. The results of calculation of relative lattice thermal conductivity in the approximation of a constant phonon mean free path and with regard to the frequency dependence of phonon relaxation time are given in Fig. 1.

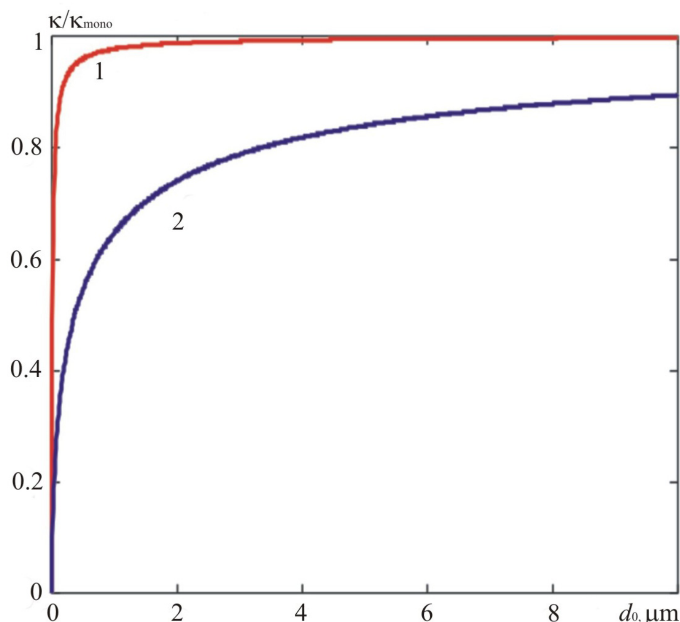

Fig. 1. Dependences of lattice thermal conductivity κ of a thin layer relative to lattice thermal conductivity κ_{mono} of $Bi_2Te_{2.7}Se_{0.3}$ single crystal on layer thickness d_0 at T = 300K: 1 – in the approximation of a constant phonon mean free path, 2 – with regard to the frequency dependence of phonon relaxation time.

From the figure it is evident that with a constant mean free path the thermal conductivity of a thin layer tends to the thermal conductivity of a single crystal considerably faster than with regard to the frequency dependence of phonon relaxation time. Thus, in the approximation of a constant relaxation time, the thermal conductivity of a single crystal is achieved already at the layer thickness equal to 2 μm. At the same time, with regard to the frequency dependence of relaxation time even with the layer thickness equal to 10 μm, only 90% of lattice thermal conductivity of a single crystal is achieved.

Dependences of correction to lattice thermal conductivity of $Bi_2Te_{2.7}Se_{0.3}$ single crystal on the temperature and layer thickness are given in Fig. 2*a*, *b*. These dependences were calculated by formulae (2) – (5).

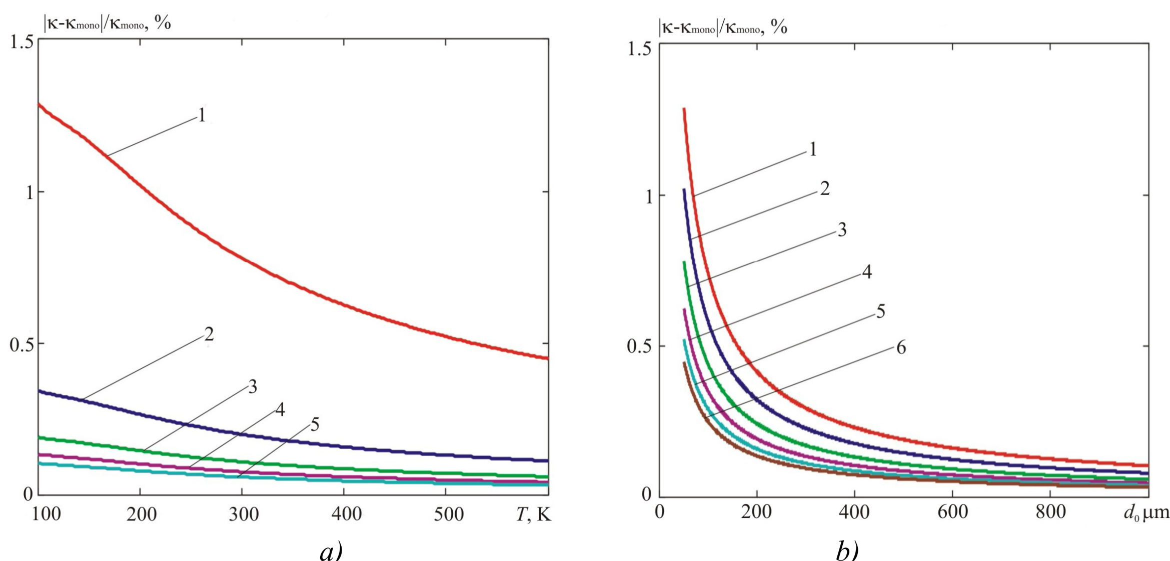

a) *b)*

Fig. 2. Dependences of correction to lattice thermal conductivity κ_{mono} *of* $Bi_2Te_{2.7}Se_{0.3}$ *single crystal: a) on the temperature for layer thicknesses:1 – 50 μm;2 – 250 μm;3 – 500 μm; 4 – 750 μm;5 – 1000 μm; b) on the layer thickness for temperatures:1 – 100; 2 – 200; 3 – 300; 4 – 400; 5 – 500; 6 – 600K.*

From the figure it is evident that correction value decreases with temperature due to reduction of phonon mean free path, and that correction decreases with increasing layer thickness due to the fact that phonon relaxation time ceases to be limited by the layer thickness. In the temperature range 100 to 600K for the layers more than 50 μm thick correction to thermal conductivity of a single crystal does not exceed 1.5%. Hence, the thickness of TEM layer exceeding 50 μm scarcely affects the lattice thermal conductivity.

Impact of charge carrier scattering at the boundaries of thin layers on the electric conductivity

Let us assume that the mean free path of charge carriers in a bulk material depends on their energy by the power law $l_e \propto \varepsilon^q$. We take into account that restriction of layer thickness affects charge carrier relaxation time for the same reason and in the same way as on the phonon relaxation time. Then, by analogy with [6 – 8] that considered electron scattering at the boundaries of powder particles on the contacts between them, we obtain the following formula for the electric conductivity σ of a thin single crystal layer of TEM relative to single crystal electric conductivity σ_{mono}:

$$\frac{\sigma}{\sigma_{mono}} = \frac{1}{\Gamma(q+2)} \int_0^\infty \int_0^1 \frac{k^* z x^{q+1} \exp(-x)}{x^q + k^* z} \mathrm{d}z\mathrm{d}x, \tag{6}$$

where $k^* = [\Gamma(q+1.5)/\Gamma(1.5)](d_0/l_e)$, l_e is the average charge carrier mean free path, q is the power exponent in the law of mean free path energy dependence. Formula (6) differs from similar formulae derived earlier in [6] only in the method of averaging over possible charge carrier mean free paths.

The results of calculation of the electric conductivity of a thin single crystal layer of $Bi_2Te_{2.7}Se_3$ relative to a bulk single crystal are given in Fig. 3.

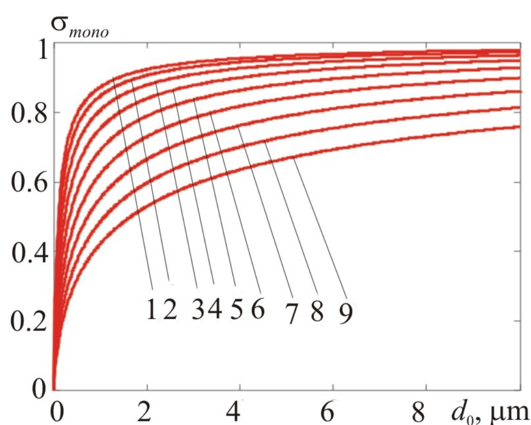

Fig. 3. Dependences of electric conductivity σ of a thin layer of $Bi_2Te_{2.7}Se_{0.3}$ relative to a single crystal σ_{mono} on the layer thickness d_0 at 300K. Dependences 1 – 9 were built for q values in the range of 0 – 4 s with an increment 0.5.

From the results of calculation it follows that for power exponent $q = 0$ that is most common in semiconductor TEM in the temperature range relevant to use, the thickness of a plane layer needed to keep the electric conductivity at a level of 90% relative to single crystal at 300 K, is about 1.5 μm.

Note that due to the Casimir effect [3] the lattice thermal conductivity (Fig. 1) and electric conductivity (Fig. 3) of a thin layer are always less than the respective characteristics of a single crystal.

To calculate the electric conductivity of a single crystal layer versus its thickness, preliminary estimate of electron mean free path in $Bi_2Te_{2.7}Se_3$ material was made and the lattice component of thermal conductivity was separated from the electron component. It was done from the data on electron concentration n_0, effective mass of electron states density m_e^* and electric conductivity σ_{mono} at 300K by known relationships [4] on the assumption that electron mean free path does not depend on energy, hence, scattering factor used in [4], $r = -0.5$. This assumption is justified on condition of electron scattering both on acoustic phonon deformation potential and on impurities, at least at high doping levels. The only difference is that with acoustic phonon scattering the electron mean free path is inversely proportional to temperature, and at impurity scattering it is temperature independent.

At first, in the temperature range 100 to 600 K an equation was solved that determines normalized to thermal motion energy chemical potential η of electron gas and has the form:

$$n_0 = \frac{4\left(2\pi m_e^* k_B T\right)^{3/2}}{\sqrt{\pi} h^3} F_{1/2}(\eta). \tag{7}$$

Following that, the mean free path l_e was estimated on the basis of relation for single crystal electric conductivity:

$$\sigma_{mono} = \frac{2 n_0 e^2 l_e \sqrt{\pi} F_0(\eta)}{3\Gamma(1.5)\sqrt{2 m_e^* k_B T}\, F_{1/2}(\eta)}, \tag{8}$$

where $F_r(\eta)$ are the Fermi integrals of respective indices determined by the relation:

$$F_r(\eta) = \int_0^\infty \frac{x^r \mathrm{d}x}{\exp(x-\eta)+1}. \tag{9}$$

Taking into account that for $Bi_2Te_{2.7}Se_{0.3}$ single crystal $n_0 = 3\cdot 10^{19}$ cm^{-3}, $m^* = 1.25 m_0$, $\sigma_{mono} = 1100\ \Omega^{-1}$cm^{-1}, we obtain l_e=21 nm at a temperature of 300 K. Then, with regard to relations (7) – (9), the temperature dependence of electric conductivity of $Bi_2Te_{2.7}Se_{0.3}$ single crystal was calculated.

Dependences of correction to electric conductivity of *n*-type single crystal $Bi_2Te_{2.7}Se_{0.3}$ on the temperature and layer thickness are presented in Fig. 4. These dependences were calculated by formula (6), assuming that $q = 0$ and electron mean free path is proportional to temperature [4], i.e. the relation is valid:

$$l_e(T) = \frac{300 l_e(300)}{T}, \qquad (10)$$

where $l_e(300)$ is mean free path at a temperature of 300 K.

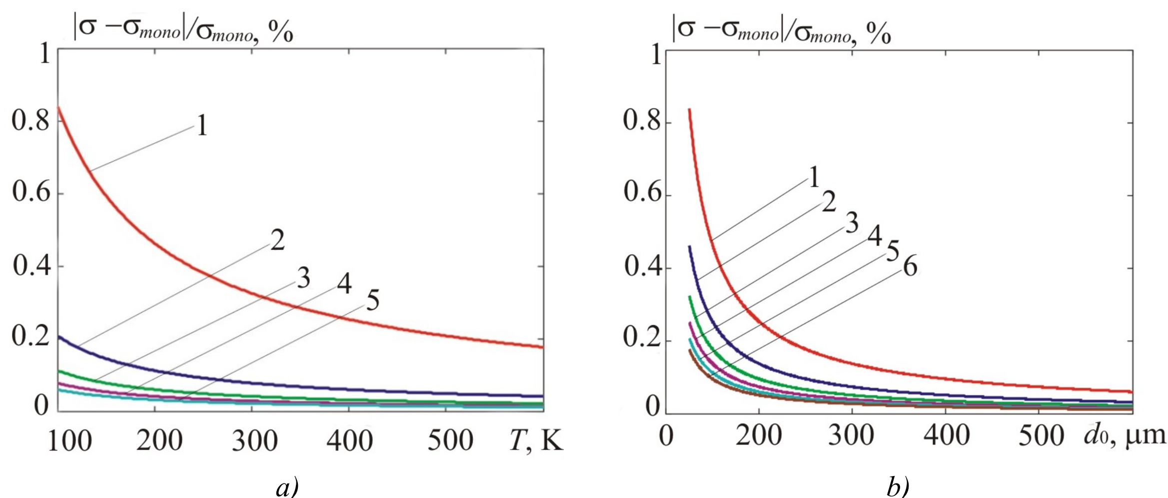

Fig. 4. Dependences of correction to the electric conductivity of $Bi_2Te_{2.7}Se_{0.3}$ single crystal:
a) on temperature at layer thicknesses, μm: 1 – 50; 2 – 250; 3 – 500; 4 – 750; 5 – 1000;
b) on layer thickness at temperatures, K: 1 – 100; 2 – 200; 3 – 300; 4 – 400; 5 – 500; 6 – 600K.

Dependences of correction to single crystal electric conductivity on temperature and layer thickness are determined by the same factors as the temperature and thickness dependences of lattice thermal conductivity, namely a reduction of electron mean free path with a rise in temperature and gradual leveling the role of scattering at the layer boundaries with its thickness increase. In the temperature range 100 to 600 K for layers more than 50 μm thick a correction to single crystal electric conductivity does not exceed 1%. Therefore, TEM layer thickness over 50 μm scarcely affects its electric conductivity.

Thermoelectric figure of merit of thin layers

Consider now the temperature and thickness dependences of thermoelectric figure of merit of a thin layer relative to single crystal. We take into account that in the approximation of constant relative to energy mean free path, charge carrier scattering at the layer boundaries does not affect thermopower. Indeed, a general formula for the Seebeck coefficient in the case of a quadratic and isotropic law of electron dispersion is given by:

$$\alpha = \frac{1}{eT} \frac{\int_0^\infty \tau(\varepsilon)\varepsilon(\varepsilon-\zeta) f_0'(\varepsilon)\sqrt{\varepsilon}\, d\varepsilon}{\int_0^\infty \tau(\varepsilon)\varepsilon f_0'(\varepsilon)\sqrt{\varepsilon}\, d\varepsilon} \qquad (11)$$

where $f_0'(\varepsilon)$ is a derivative of the Fermi-Dirac distribution function with respect to energy. For relaxation time $\tau(\varepsilon)$ on condition of constant with respect to energy mean free path l^* of charge carriers the following relation is valid:

$$\tau(\varepsilon) = \frac{l^* \sqrt{m^*}}{\sqrt{2\varepsilon}}, \tag{12}$$

where l^* is determined by scattering both in the bulk and at the layer boundaries, i.e. by the formula:

$$l^* = l_e \left\langle \frac{L^*}{l_e + L^*} \right\rangle, \tag{13}$$

where l_e is electron mean free path in a single crystal, L^* is mean free path due to scattering at the layer boundaries, angular brackets denote averaging over layer thickness. Therefore, l^* appears in the numerator and denominator of formula (11) as a constant multiplier which is taken out of the integral and does not affect thermopower. Hence, thermopower is not affected by scattering at the layer boundaries.

The electron component of single crystal thermal conductivity κ_{emono}, needed to calculate the figure of merit of material, is found from the Wiedemann-Franz ratio:

$$\kappa_{e\,mono} = L\sigma_{mono}T, \tag{14}$$

where the Lorentz number L is

$$L = \left(\frac{k_B}{e}\right)^2 \left[\frac{3F_2(\eta)}{F_0(\eta)} - \frac{4F_1^2(\eta)}{F_0^2(\eta)}\right]. \tag{15}$$

We now turn directly to calculation of thermoelectric figure of merit of a thin layer relative to a single crystal with regard to electron thermal conductivity contribution. For this purpose we will use a subsidiary expression written with regard to relations (2) and (6) as follows:

$$Z_a = \left(\int_0^1 \frac{d_0 l_e^{-1}(T)z}{d_0 l_e^{-1}(T)z + 1}\mathrm{d}z\right)\left[\int_0^1\int_0^1 \frac{x^4 \exp(x/\theta)}{[\exp(x/\theta)-1]^2}\left(\frac{k_\parallel^* z}{1 + k_\parallel^* Q_{l\parallel}(x)z} + \frac{2k_\parallel^* z}{1 + k_\parallel^* Q_{t\parallel}(x)z}\right)\mathrm{d}z\mathrm{d}x\right]^{-1}\left\{\int_0^1 \frac{x^4 \exp(x/\theta)}{[\exp(x/\theta)-1]^2}\left(\frac{1}{Q_{l\parallel}(x)} + \frac{2}{Q_{t\parallel}(x)}\right)\mathrm{d}x\right\}. \tag{16}$$

Taking into account that scattering at the layer boundaries does not affect thermopower and electron thermal conductivity and electric conductivity in case of electron mean free path independence of energy depend on layer thickness through the same multiplier, we obtain the following final expression for thermoelectric figure of merit Z of a thin layer relative to single crystal Z_{mono}:

$$Z/Z_{mono} = \frac{1 + \kappa_{e\,mono}/\kappa_{mono}}{Z_a^{-1} + \kappa_{e\,mono}/\kappa_{mono}}. \tag{17}$$

The thickness and temperature dependences of the figure of merit of $Bi_2Te_{2.7}Se_{0.3}$ thin layer are given in Fig. 5.

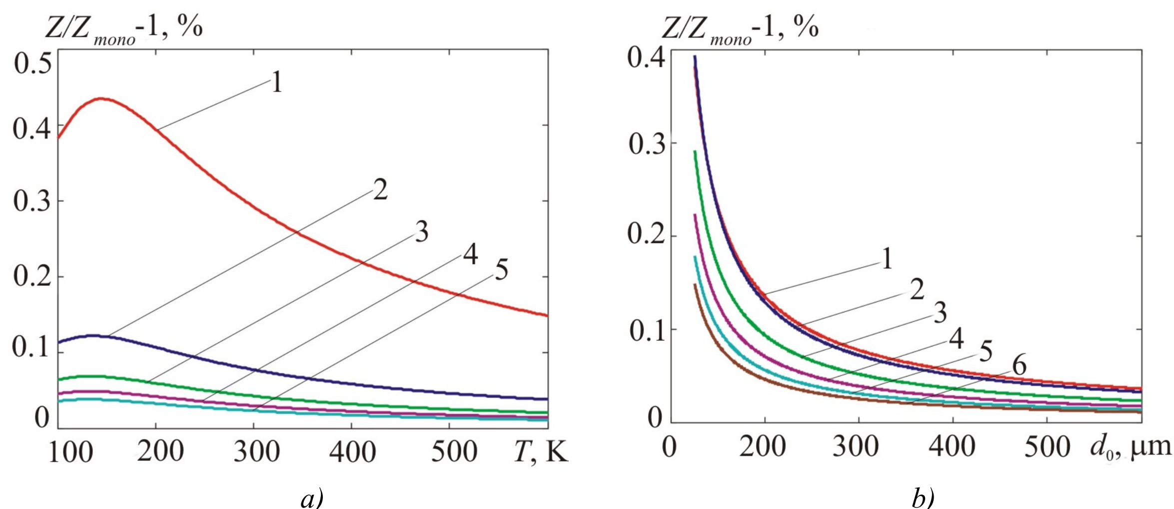

Fig. 5. Dependences of the figure of merit Z of a thin layer of $Bi_2Te_{2.7}Se_{0.3}$ relative to a single crystal Z_{mono}: a) on temperature at layer thicknesses, μm:1 – 50; 2 – 250; 3 – 500; 4 – 750; 5 – 1000; b) on layer thickness at temperatures, K:1 – 100; 2 – 200; 3 – 300;4 – 400; 5 – 500; 6 – 600K.

From the figure it is seen that with a rise in temperature and layer thickness, the figure of merit of a layer tends to the figure of merit of a single crystal. The temperature and thickness dependences of the figure of merit of a layer relative to a single crystal are determined by reduction in electron and phonon mean free paths, as well as by leveling of scattering at layer boundaries with its thickness increase. In the thickness range 50 to 1000 μm at temperatures 100 to 600 K the expected figure of merit increase of thin layers of *n*-type $Bi_2Te_{2.7}Se_{0.3}$ relative to a single crystal does not exceed 0.5%.

It should be noted that depending on the ratio between charge carrier and phonon mean free paths the figure of merit of TEM in going from a single crystal to a thin layer can be both increased and decreased.

Conclusions

1. The impact of phonon and charge carrier scattering at the boundaries of microminiature layers on the electric conductivity and lattice thermal conductivity is most essential at thicknesses less than 10 μm.
2. Account of the frequency dependence of phonon relaxation time and the energy dependence of charge carrier mean free path increases the impact of scattering at the boundaries of micromimiature layers on their kinetic coefficients.
3. A stronger reduction of lattice thermal conductivity as compared to electric conductivity creates prerequisites for TEM figure of merit improvement in going from the bulk single crystals to microminiature layers.
4. With the thicknesses exceeding 50 μm and the temperatures 100 – 600 K the expected figure of merit increase of thin layers of *n*-type $Bi_2Te_{2.7}Se_{0.3}$ relative to a single crystal does not exceed 0.5%.

References

1. L.W.Da Silva, M.Kaviany, Microthermoelectric Cooler: Interfacial Effects on Thermal and Electrical Transport, *International Journal of Heat and Mass Transfer* **47**(10 – 11), 2417 – 2435 (2004).
2. P.V.Gorskiy, V.P.Mikhalchenko, Reduction of Thermoelectric Material Lattice Thermal Conductivity Using Shape-Forming Element Optimization, *J.Thermoelectricity* 1, 19 – 27 (2013).

3. P.G. Klemens, Lattice Thermal Conductivity, In: *Solid State Physics. Advances in Research and Applications, Vol.7, pp.1 – 98 (Academic Press. Inc. Publ., New York, 1958), 526 p.*
4. B.M.Goltsman, V.A.Kudinov, and I.A.Smirnov, Semiconductor Thermoelectric Materials Based on Bi_2Te_3. (Moscow: Nauka, 1972), 320 p.
5. *CRC Handbook of Thermoelectrics, edited by D.M.Rowe* (CRC Press, London, New York, 1995).
6. P.V.Gorskiy, V.P.Mikhalchenko, Electric Conductivity of Contacting Particles of Thermoelectric Material, *J.Thermoelectricity* 2, 13 – 19 (2013).
7. P.V.Gorskiy, V.P.Mikhalchenko, On the Issue of the Mechanism for Increasing the Thermoelectric Figure of Merit of the Bulk Nanostructured Materials, *J.Thermoelectricity* 5, 5 – 11 (2013).
8. L.I. Anatychuk, P.V. Gorskiy, and V.P. Mikhalchenko, Impact of Size Effects on the Properties of Thermoelectric Materials, *J.Thermoelectricity* 1, 5 – 13 (2014).

Submitted 4.09.2015

A.A. Nikolaeva[1,2], L.A.Konopko[1,2], T.E. Huber[3], A.K.Kobylianskaya[1], G.I.Para[1]

[1]D.Gitsu Institute of Electronic Engineering and Nanotechnologies of the Academy of Sciences of Moldova, Academiei str., 3/3, Kishinev, MD-2028, Republic of Moldova;
[2]International Laboratory of High Magnetic Fields and Low Temperatures, ul. Gajowicka 95, Wroclaw, 53-421, Poland
[3]Department of Chemistry, Howard University, 500, DC 20059, Washington, USA

EFFECT OF THE LIFSHITZ TOPOLOGICAL TRANSITIONS INDUCED BY TENSILE DEFORMATION ON THE THERMOPOWER AND RESISTANCE OF BISMUTH WIRES

This paper presents the results of studying the effect of elastic deformation on the resistance and thermopower of bismuth nanowires at 4.2 - 300 K. Glass-coated single-crystal Bi wires of different diameters (70 and 320 nm) were prepared by high-frequency liquid phase casting by the Ulitovsky method. According to X - Ray diffraction, all the wires had the same (10$\underline{1}$1) orientation along the wire axis. Methods of investigation of Shubnikov-de Haas oscillations in the pure and Sn - doped Bi wires have conclusively proven that the point of the thermopower sign inversion on the deformation dependences $\alpha(\xi)$, which coincides with the position of the maximum resistance on $R(\xi)$, is associated with an electronic topological transition induced by the elastic deformation whereby the T - holes at T - point of the Brillouin zone disappear. The enhancement of the thermoelectric figure of merit of Bi wires under high-temperature deformation is discussed.

Key words: thermoelectricity, bismuth wires, elastic deformation, Shubnikov-de Haas oscillations, quantum size effect, topological transitions.

Introduction

A rising tide of interest in thermoelectricity in recent years is due to development of new concepts, theories and nanotechnologies, opening up new ways for enhancement of thermoelectric figure of merit both in the nanostructures and the bulk nanostructured materials [1 – 4]. Thermoelectric figure of merit is defined by the expression: $Z = \alpha^2\sigma/\chi$, where α is thermopower, σ is electric conductivity, $\chi = \chi_e + \chi_p$, χ_p is lattice thermal conductivity, χ_e is electron thermal conductivity.

Of particular interest are nanowires based on bismuth and its alloys [1 – 3, 5]. Quantum and classical size effects observed in nanowires open up the prospects for electron and phonon transport control by means of structural engineering. The authors of [1 – 3] demonstrated the enhancement of thermoelectric figure of merit in size-restricted structures, specifically in *Bi* nanowires. Increase in Z can be due to quantum size effect leading to semimetal - semiconductor transition with an increase in the density of states close to the Fermi level, which, in turn, results in considerable thermopower increase. As a result of this, power factor ($\alpha^2\sigma$) grows as compared to the bulk samples. On the other hand, carrier and phonon scattering on the boundary will lead to reduction of thermal conductivity, which also leads to Z increase. In so doing, realization of phonon scattering mechanism (impairing figure of merit) must not impede effective

transport of charge carriers [6]. Small diameter of nanowires leads to efficient phonon scattering by the surface and gigantic reduction of thermal conductivity [7, 8].

Only a few papers pursued experimental research of thermal conductivity in bismuth nanowires [5, 9, 10] of different structure and manufactured by different methods. Both in single crystal and polycrystal wires there was a considerable suppression of thermal conductivity as the wire diameter d was reduced. Moreover, in single crystal *Bi* wires there was considerable thermal conductivity anisotropy [10] exceeding that value in the bulk samples of *Bi*. In [5] it was shown that in single crystal *Bi* nanowires grown with (110) orientation (i.e. normal to trigonal axis) the thermal conductivity is a factor of 4 smaller than in the wires with (102) orientation and is considerably reduced with decreasing diameter, which points to strong scattering of hot carriers at the boundaries.

A search for materials with a combination of such properties as high electric conductivity is the task of optimization and thermoelectric figure of merit enhancement. Complex properties control can be realized with the knowledge of interrelation between the structure and properties of semimetals and semiconductors of different composition, relying upon the theoretical concepts of condensed matter physics.

One of possible methods of thermoelectric parameters control is elastic deformation whereby there is an essential change in the Fermi surface topology in *Bi* and its alloys [11, 12, 13].

In [13] it was shown that elastic deformation in glass – coated single crystal *Bi* nanowires can reach 2 – 3 % of relative elongation, which brings about essential changes in the Fermi surface topology.

This work presents the results of research on the conductivity and thermopower changes under elastic deformation of glass-coated single crystal *Bi* wires of different diameters in the temperature range 4.2 to 300 K. A change in the Fermi surface topology was controlled by means of Shubnikov - de Haas (ShH) oscillations in the wires of pure and *Sn* – doped bismuth.

Samples, experimental procedure

Glass-coated pure and *Sn* – doped *Bi* wires were prepared by liquid phase casting by the Ulitovsky-Taylor method [13 – 16] and had the form of a strictly cylindrical single crystal with diameters from 75 nm to several microns with (1011) orientation along the wire axis (Fig. 1).

Tests performed with the help of rotation *X* - ray diagrams of submicron *Bi* wires showed that the resulting wires were single crystal, as a rule, of the same orientation: wire axis coincides with ΓL – orientation in reduced Brillouin zone, which is located in bisector – trigonal plane and makes with bisector axis an angle of 19.5° (Fig. 1).

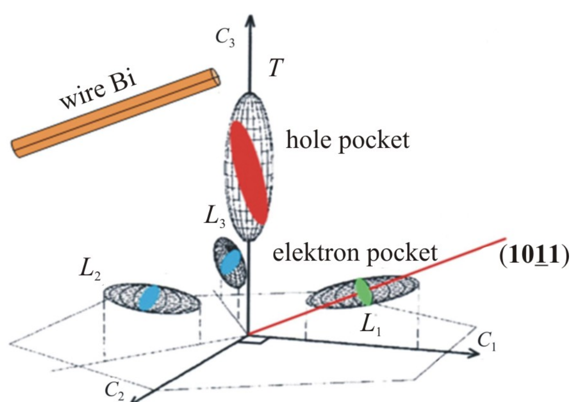

Fig. 1. (10$\underline{1}$1) *orientation of Bi Fermi surface with respect to wire axis.*

In so doing, trigonal axis C_3 is inclined to the wire axis at an angle of 70°, and one of the binary C_2 axes is normal to that axis.

Orientation of crystallographic axes in *Bi* and its alloys and structural perfection were also confirmed by the investigations of angular diagrams of revolution of transverse magnetoresistance, as well as by means of studying SdH oscillations [13 – 16].

To study the deformation curves of resistance $R(\xi)$, thermopower $\alpha(\xi)$ and SdH oscillations, a special holder was designed (Fig. 2) making possible investigations in the temperature range 4.2 to 300 K both pointwise and in the automatic mode with elastic wire tension to 2 – 3% of relative elongation in magnetic fields up to 14*T* [17].

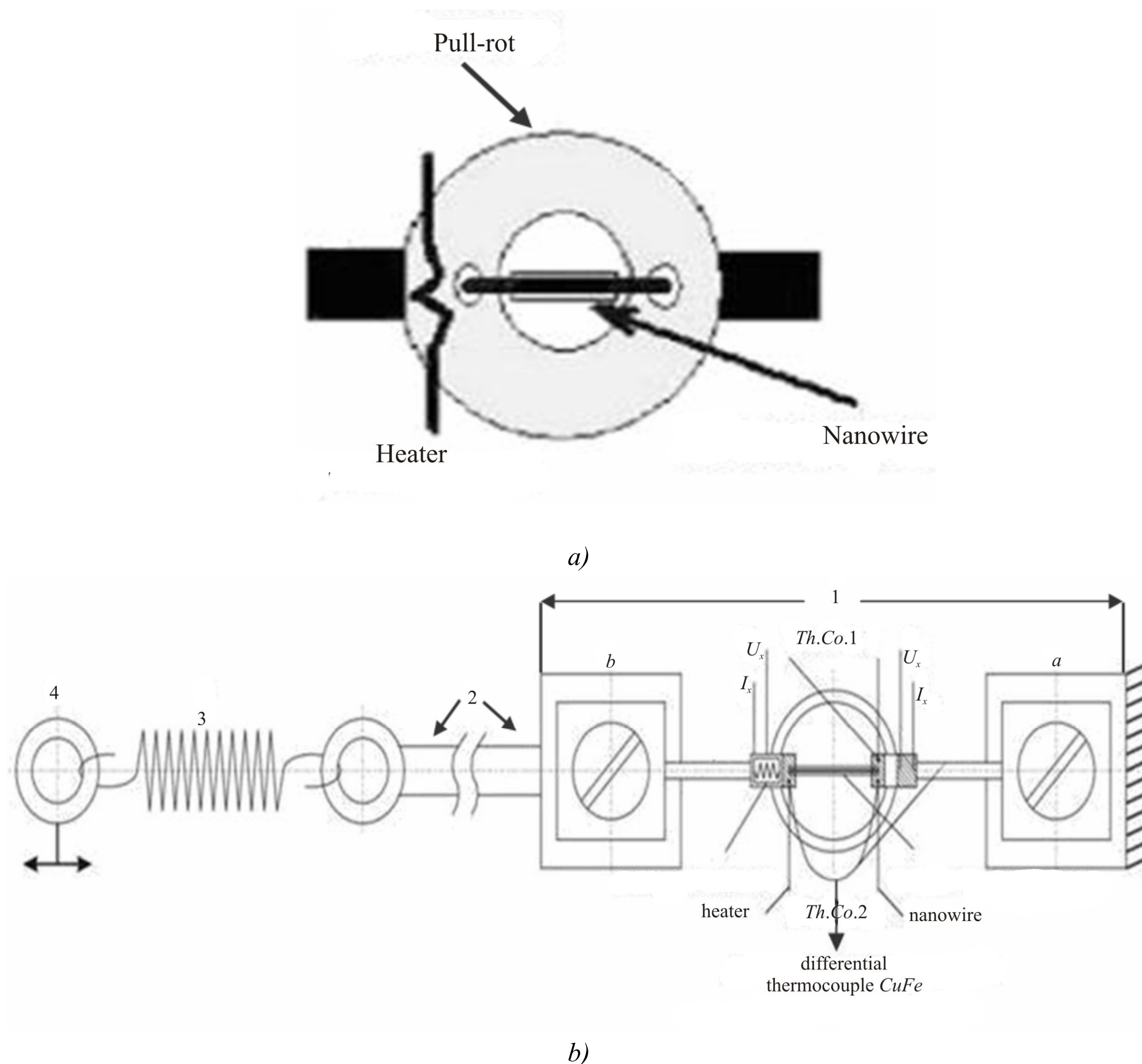

Fig.2. (a) – schematic of sample mounting on a ring of beryllium bronze when measuring kinetic properties of wires under elastic tension. b) – schematic of sample (wire) holder allowing investigations under elastic tension in the temperature range 2 to 300 K. (1 – construction of beryllium bronze ring, Th. Co. 2 – differential thermocouple CuFe, 2 – rod regulating stress from spring to collar, 3 – spring, 4 – screw).

When studying the wires exposed to elastic tension, the wire was mounted on a ring of beryllium bronze, diameter ≈ 5 mm (Fig. 2, *a*). Two contact pads of copper clad fiberglass of size 2 mm × 1 × 0.5 mm fastened on a ring at the distance of 2 – 3 mm from each other served as contact

pads for mounting a sample and a heater for creation of temperature gradient when measuring thermopower. Temperature gradient was maintained by a miniature heater and measured by a differential $Cu-Fe$ thermocouple. All the data, namely a signal from the sample, temperature, temperature gradient and the rated value of thermopower were output to computer and observed in the process of measurement on a display. The whole construction – a ring of beryllium bronze with the sample – was placed in the holder (Fig. 2, *b*).

One ring end (*a*) was secured immovably, and the other (*b*) was connected to a stretching moving member. Travel of screw (4) on rotation is passed to the free end of the spring (3), connected by rod (2) with beryllium ring. This leads to a change in force action on a ring of thermally processed beryllium bronze and, hence, to a change in the deformation of this ring, and to a change in the elongation *Bi* microwire section rigidly attached to the opposite points of beryllium ring. Screw axis by means of gear mechanism is connected to DC motor, as well as to a multiturn potentiometer. By the change in potentiometer resistance one can determine the turn angle of the screw and, accordingly, determine a change in sample elongation. Such a schematic allowed operating the experiment automatically. In this case, on switching the motor, program commands digital multimeters to measure potentiometer resistance and to measure sample resistance or thermopower, displays onscreen curve $R(\xi)$ or $\alpha(\xi)$ and saves the measured data in a file.

Preliminary calibration of ring stretched due to applied force was performed with the microscope at $T = 300$ K. The above construction allowed gradual stretching of sample to 2 – 3% of relative elongation $\xi = \frac{\Delta l}{l_0} = \frac{l - l_0}{l_0} \cdot 100\%$, where l_0 is sample length prior to stretching. The accuracy of measuring tensile force was ~ 2 %.

Special attention was focused on the observance of elastic deformation condition. For this purpose, numerous deformation cycles were performed, and reproducibility of results was estimated. Temperature dependences of resistance and thermopower both with and without elastic deformation were obtained automatically on a computerized setup in the temperature range 77 to 300 K in the Laboratory of Electronics of Size-Restricted Structures, D.Gitsu Institute of Electronic Engineering and Nanotechnologies of the Academy of Sciences of Moldova, and in the range 4.2 to 300 K - in the International Laboratory of High Magnetic Fields and Low Temperatures (Wroclaw, Poland) in magnetic fields up to 14 *T*.

Results and discussion

Complex measurements of temperature dependences of resistance $R(T)$, thermopower $\alpha(T)$, as well as deformation dependences of resistance $R(\xi)$ and $\alpha(\xi)$ of *Bi* wires of different diameters were performed in the temperature range 4.2 to 300 K.

For an unambiguous interpretation and recording of change in the section of the Fermi surface due to T - holes at elastic deformation, use was made of the wires doped with *Sn* acceptor impurity wherein the Fermi level is shifted down the energy scale and the concentration of T - holes increases essentially. This made it possible to study SdH oscillations at elastic deformation on $R(B)$ dependences, rather than on $\partial R/\partial B(B)$ derivatives, which simplified the experiment considerably.

It is known that SdH oscillations from T - holes in the longitudinal configuration $B \parallel I$ of pure *Bi* wires (at $\xi = 0$) are observed only in strong magnetic fields, on $\partial R/\partial B(B)$ derivatives, as a rule on the wires where longitudinal magnetoresistance is not saturated in a strong magnetic field, but starts to increase [18] at $B > 8$ T. Though at precise orientation of magnetic field $B \parallel I$ and parallel to

(10$\underline{1}$1) direction in *Bi* wires with $d < 500$ nm the magnetoresistance is saturated in magnetic fields 6 T < *B* < 14 T [16, 19].

Note that, as was found earlier, on the wires with $d < 75$ nm there was a semimetal-semiconductor transition caused by quantum size effect that manifested itself in "semiconductor" nature of dependence $R(T)$ and inversion of thermopower sign to $\alpha(T)$ [13 – 15, 19].

The figure represents deformation dependences of resistance *R* on the tension of *Bi* wires of diameters *d* at 4.2 K. The elasticity of deformation (tension) process was confirmed by the reproducibility of results with multiple cycles of elastic tension. For *Bi* wires with $d \geq 90$ nm a typical feature is that in low temperature region (4.2 K) on the deformation curve $R(\xi)$ there is a minimum, at $\xi = 0.8 - 1.2$ % in the area of electron topological transition $3e^L{+}1h^T{\rightarrow}2e^L{+}1h^T$, then the resistance is drastically increased by a factor of 2 – 4, and in the area of maximum tensions an abnormal maximum is formed which was followed by plasticity area. Such a nonmonotonous dependence of resistance on tensile force is typical of wires with $d > 90$ nm.

At wire diameters smaller than 80nm, the shape of deformation curves at 4.2 K is changed, the maximum on $R(\xi)$ is reduced and at wire diameters 60 – 45nm the deformation curve $R(\xi)$ is declining (Fig. 3, curve 1). Resistance $R(\xi)$ is reduced by 20 – 30%. Such a shape of deformation curve of resistance $R(\xi)$ is typical of bismuth wires doped with *Te* (Fig. 3, curve 2), when holes at *T* - point disappear and conductivity is defined only by *L* - electrons. Thus, this fact is an indirect proof of semimetal-semiconductor transition in *Bi* wires with $d < 80$ nm due to quantum size effect.

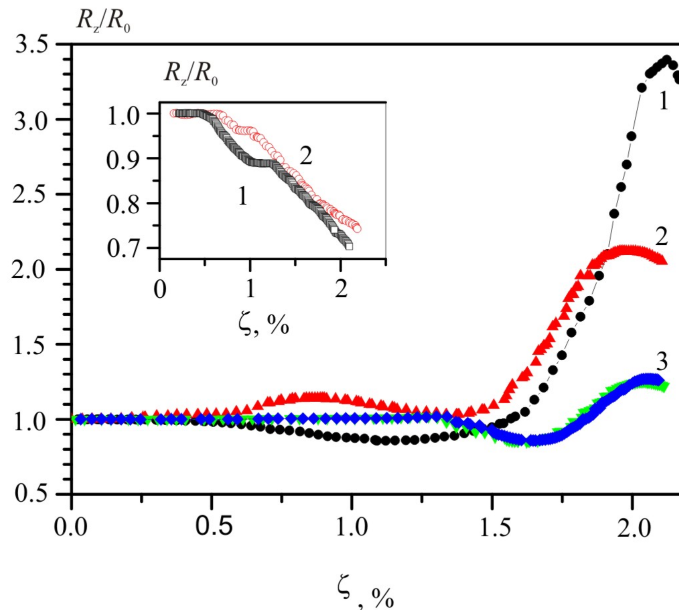

Fig. 3. Deformation curves of reduced resistance $R_\xi/R_0(\xi)$ of Bi wires of different diameters at T = 4.2 K. 1. d = 300 nm, 2. d = 110 nm, 3. d = 80nm. On the insert: deformation dependences of resistance R(ξ) of Bi wire (1), T = 4.2K, d=50nm and (2) Bi - 0.025 at % Te, d = 200nm. The scale for curve 2 is doubled.

Figs. 4, 5 represent transformation of deformation curves of resistance $R(\xi)$ and thermopower $\alpha(\xi)$ of *Bi* wires, $d = 320$ nm, with a rise in temperature from 4.2 K to 300 K. There is a gradual transition from a nonmonotonous dependence $R(\xi)$ at 4.2 K to a linear dependence (with two slopes) of resistance decrease with tensile deformation at temperatures 250 – 300 K (Fig. 4, curve 9).

The smaller wire diameter d, the higher the temperature of transition from a nonmonotonous dependence $R(\xi)$ to a linear resistance decrease with a rise in temperature. The value of resistance maximum $R(\xi)$ and the behaviour of deformation dependence $R(\xi)$ are essentially dependent on temperature T (Fig. 4).

With a rise in temperature, the value of maximum on the deformation curve of resistance was reduced essentially (Fig. 4). The insert in Fig. 4 shows exponential growth of maximum resistance value by $R(\xi)$ with temperature decrease, which points to reduction of charge carrier concentration.

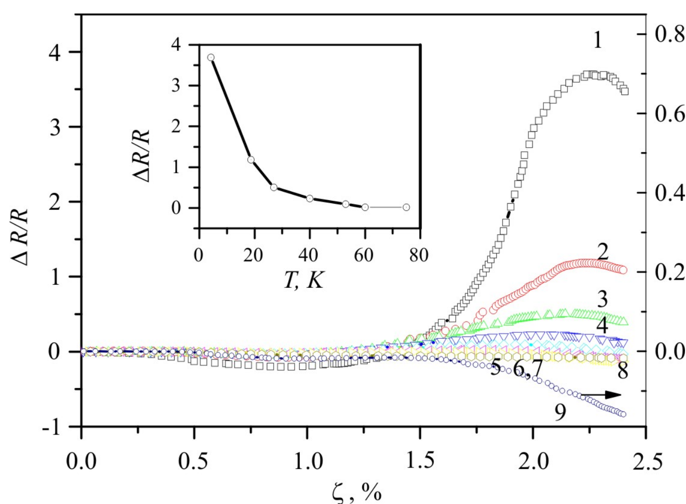

Fig. 4. Deformation dependences of relative resistance $\Delta R/R(\xi)$ of Bi wire with d = 320 nm: 1- T = 4.2, 2 – T = 18,7, 3 – T = 27, 4 – T = 40, 5 – T = 53, 6- T = 60, 7- T = 75, 8- T = 187, 9 – T = 203K. On the insert: maximum resistance value $(\Delta R/R)_{max}$ on the deformation dependences of resistance versus temperature T.

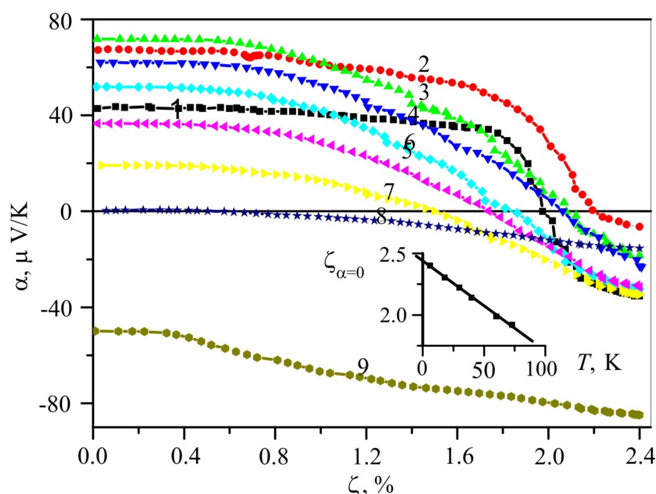

Fig. 5. Deformation dependences of thermopower $\alpha(\xi)$ at different temperatures of Bi wire with d = 320 nm 1- T = 4.2, 2- T = 18.7, 3- T = 27, 4- T = 40, 5- T = 53, 6- T = 60, 7- T = 75, 8- T = 187, 9- T = 203K. On the insert: elastic deformation value ξ, whereby thermopower inverts sign under tension versus temperature T.

Fig. 5 represents deformation dependences of thermopower $\alpha(\xi)$ of *Bi* wire with d = 320nm at different temperatures. It has been established that with a rise in temperature the inversion of thermopower sign is shifted to the area of weaker elastic deformations (insert in Fig. 5).

Dependence of temperature of thermopower sign inversion from (+) to (-) on the deformation curves of thermopower α(ξ) is almost linear (insert in Fig. 5). Different temperature dependences of resistance and thermopower anomalies are proof of the fact that resistance behaviour is due to other mechanism than thermopower, but both facts point to reduction of *T* - holes concentration at tensile deformation of *Bi* wires with (10<u>1</u>1) orientation along the axis.

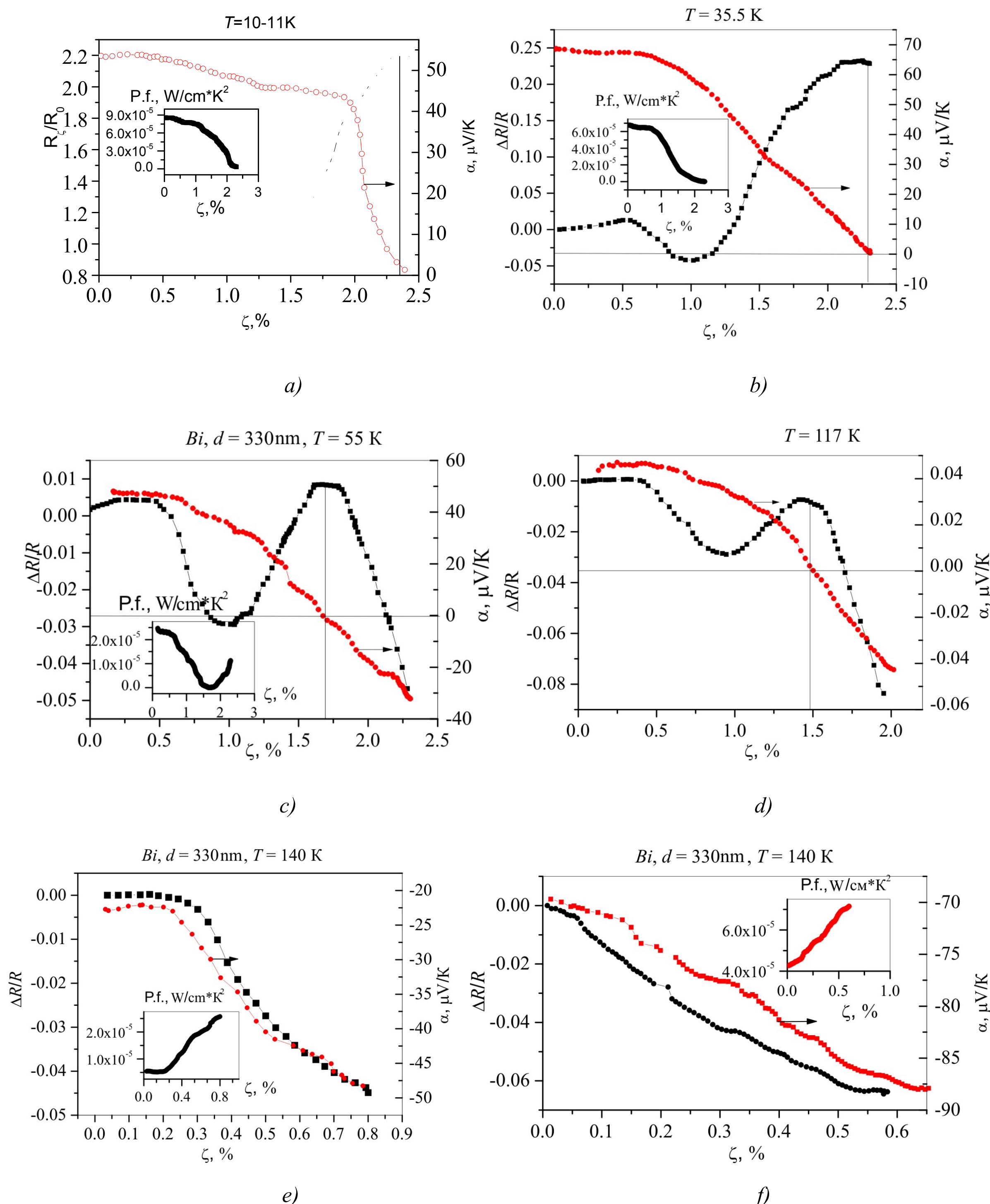

Fig. 6. Deformation dependences of relative resistance ΔR/R(ξ) and thermopower α(ξ) of Bi wire, d = 330nm at different temperatures: a) T = 11, b) T = 35.5, c) T = 55, d) T = 117, e) T = 140 K, f) T = 300K. On the inserts – deformation dependences of power factor P.f. = $\alpha^2\sigma$.

Figs. 6, 7 represent deformation dependences of resistance and thermopower of *Bi* wires with $d = 320$ nm and $d = 75$ nm at different temperatures.

As was shown in [12, 20], anisotropic deformation of crystal lattice of *Bi* wires leads to a strong nonequivalent change in the volume of individual parts of the Fermi surface, causing no essential change in the anisotropy and slope angles of increasing electron ellipsoids.

Resistance decrease on $R(\xi)$ at deformation in tensile region 0 – 1 % and formation of minimum at $\xi = 0.8 - 1.1$ % is explained in terms of electron topological transition, whereby carriers from electron ellipsoid L_1 elongated along the wire axis with less mobile carriers flow over to $L_{2,3}$ electron ellipsoids with more mobile charge carriers up to electron topological transition $3e^L+1h^T \rightarrow 2e^L+1h^T$. Exactly at these values of ξ a minimum is formed on the deformation curve of resistance $R(\xi)$ at 4.2 K (Fig. 6 *a*, *b*, *c*, *d*, *e*, *f*, Fig. 7).

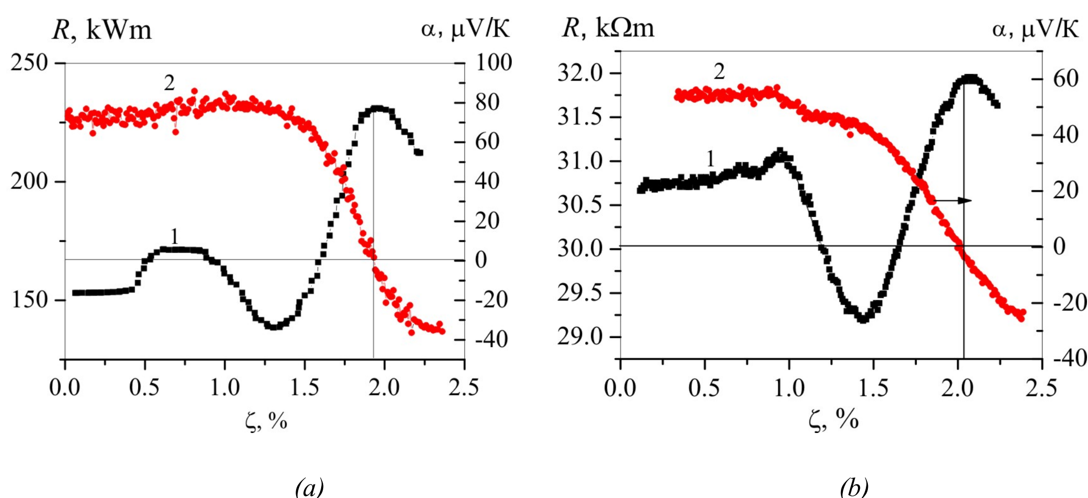

Fig. 7. Deformation dependences of resistance R(ξ) (1) and thermopower α(ξ) (2) in Bi nanowires Bi, d = 70 nm, at different temperatures: a)curve 1 – T = 4.2K, curve 2- T = 6.6 K);b)T = 55 K.

For the first time the availability of transition under anisotropic deformation of bulk *Bi* crystals was mentioned in [12, 20], and under tension of whiskers - in [21]. In the deformation area prior to vanishing of S^e, carrier concentration of electron ellipsoid L_1 at extreme point is so small that contribution to electric conductivity is observed no more. In the bulk samples of *Bi*, critical deformation whereby the electron ellipsoid L_1 disappears $\xi_k \approx 0.5\%$, which is in good agreement with the value of $\xi_k = 0.4$ % in *Bi* whiskers [21]. According to estimates made in [20], such electron topological transition should occur at $\xi = 0.4$ %.

At 200 K the resistance is reduced in the entire area of elastic tension, the absolute value $\Delta R/R$ in the temperature range 250 to 300 K being not more than 10 – 15 %. The temperature whereby there is a quantitative change in dependence $R(\xi)$ is a function of the wire diameter *d*. A nonmonotonous dependence $R(\xi)$ is observed in the wires of almost all diameters under study ($d > 80$ nm) and takes place up to temperatures 100 to 200 K, shifting towards higher temperatures with decreasing diameter.

Conspicuous is the fact that maximum on the deformation curves of resistance at different temperatures coincides with the point of inversion of thermopower sign from (+) to (-) on the deformation curves of thermopower (Fig. 6 *a* – *d*, Fig. 7).

The most precise information on the change in the Fermi surface (FS) and its variation with lattice deformation was obtained from the Shubnikov - de Haas effect (SdH).

As already mentioned above, SdH oscillations from T - holes (from the hole section close to maximum) are poorly seen on the wires at $B \parallel I$ on $R(B)$, i.e. on the longitudinal magnetoresistance, particularly if ellipsoid is reduced under deformation and there is a sharp drop of oscillation amplitude. However, experiments on the bulk Bi samples on recording $\partial R/\partial B(B)$ derivatives both in $\perp$ and $\parallel$ magnetic fields have shown that under tensile deformation along bisector axis there is a reduction in the volume of hole ellipsoid at T - point [12, 20]. Experiments on the wires doped with Sn acceptor impurity, when the Fermi level is determined down the energy scale, and concentration of T - holes is increased on doping, lead to manifestation of ShH oscillations from T - holes on the longitudinal magnetoresistance even on $R(B)$ (Fig. 8), so it is easy to trace a change in the period of ShH oscillations from T - holes (Fig. 8) under deformation of the wires with (10$\underline{1}$1). orientation.

For clarity, Fig. 8 shows ShH oscillations on the longitudinal magnetoresistance $R(B)$ of Bi – 0.07at % Sn wire with d = 600 nm under different values of tensile deformation. The insert in Fig. 8 shows a change in the frequency of ShH oscillations from T - holes, L_1 and $L_{2,3}$ hole ellipsoids at L - point of the Brillouin zone $f = [\Delta(1/H)]^{-1} = \frac{S_{ex}c}{eh}$, where S_{ex} is extreme section of the Fermi surface normal to magnetic field direction (shaded cross - sectional area of the Fermi surface in Fig. 1). From Fig. 8 (insert) it follows that the volumes of the Fermi surface of T - holes (f_1) and $L_{2,3}$ – hole ellipsoids at point L (f_3) are reduced, and the volume of hole ellipsoid L_1 (f_2) is increased.

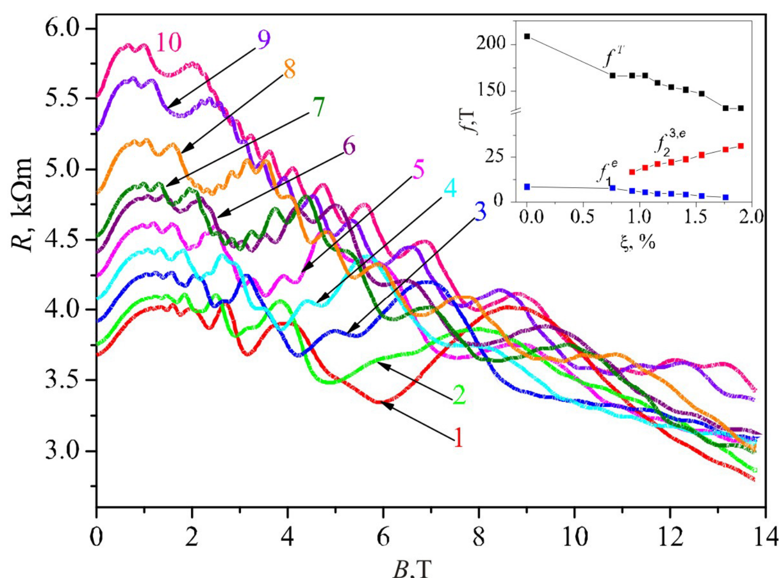

Fig. 8. ShH oscillations on longitudinal magnetoresistance R(B) (B || I) of Bi wire - 0.07at % Sn with (10$\underline{1}$1) orientation along the axis of wire d = 600 nm with fixed values of elastic tension from ξ = 0 to ξ = 1.9 %, T = 4.2 K. On the insert: Deformation dependences of ShH oscillation frequencies on the sections of the Fermi surface: T- holes (f_1), L_1 - hole (f_2) and $L_{2,3}$ - hole ellipsoids (f_3) at T = 4.2 K.

Estimation of elastic deformation whereby T - ellipsoid will disappear was done with regard to the data on ShH oscillations on the bulk Bi samples (method of extrapolation to 2 % of relative elongation) yielded the value of ξ = 1.2%, when a tensile force is directed along the bisector C_1 axis. Taking into account that the axis of Bi wires is deflected by 20 % from the bisector C_1 axis and that topological transition $3e^L+1h^T \rightarrow 2e^L+1h^T$ occurs in Bi wires at the values of ξ= 0.8 – 1 %, i.e. twice those in the bulk samples of Bi (ξ_k = 0.4 %), oriented along C_1. Thus, the value of relative elongation

ξ = 2.2 % is a real one, indicating the disappearance of T - ellipsoid in pure *Bi* wires at maximum point on $R(\xi)$ dependence. Exactly at this point there occurs inversion of thermopower sign from (+) to (-).

From the standpoint of practical applications, in the context of thermoelectricity it would be interesting to trace as a whole a change in resistance $R(\xi)$, thermopower $\alpha(\xi)$ and power factor $\alpha^2\sigma$ due to elastic tensile deformation in the temperature range 200 to 300 K. In Fig. 6 $a - f$ (inserts) are shown calculated values of power factor as a function of tension of *Bi* wire with d = 320 nm at different temperatures. It is established that power factor growth occurs only in the temperature range where resistance is reduced, i.e. at high temperatures. In the low temperature region, where $R(\xi)$ is of nonmonotonous nature, power factor is reduced as well. A simultaneous resistance decrease and increase in the absolute thermopower value at tensile deformation in *Bi* wires in the high temperature range T > 250 K results in power factor duplication $P.f. = |\alpha|^2\sigma$ (Fig. 6, *a*), which achieves the value 7.2*10^{-5} W/cm*K^2 at temperatures 250 – 300 K, at ζ = 0.6 % for a wire with d = 330 nm. Restriction of power factor growth is related to restriction of the area of elastic tension of *Bi* wires to 1.5 % in the temperature range T > 250 K.

Taking into account the fact that thermal conductivity in *Bi* nanowires with d = 200 nm at 300 K is at least 3 times lower [5, 10] than in the bulk samples, one should expect the value of ZT more than unity at 300 K in *Bi* wires at elastic tension deformation along the bisector axis.

Conclusions

Integrated studies of the deformation dependences of resistance and thermopower of glass-coated single crystal *Bi* wires of different diameters in the temperature range 4.2 to 300 K have been performed. It is shown that anomalies on the deformation dependences of resistance $R(\xi)$ and thermopower $\alpha(\xi)$ correspond to deformation-induced topological transitions.

The method of investigation of Shubnikov - de Haas oscillations in the pure and acceptor impurity - doped bismuth has proved conclusively that the point of thermopower sign inversion to $\alpha(\xi)$, which coincides with the position of maximum on $R(\xi)$ in low temperature region is related to electronic topological transition induced by strong (up to 6 GPa) elastic deformation whereby holes at T - point of the Brillouin zone disappear. The thermoelectric figure of merit is increased to Z > 1 at 300 K with elastic deformation of single crystal *Bi* wires with (10$\underline{1}$1) orientation along the axis.

The work was performed with the support of Institutional project 15.817.02.09A.

References

1. L.D.Hicks, M.S.Dresselhaus, Thermoelectric Figure of Merit of a One-Dimensional Conductor, *Phys. Rev. B* 47, 16631 – 16634 (1993).
2. Y.-M. Lin, X.Sun, and M.S.Dresselhaus, Theoretical Investigation of Thermoelectric Transport Properties of Cylindrical Bi Nanowires, *Phys. Rev. B* 62, 4610 – 4623 (2000).
3. J.Heremans and C.M.Thrush, Thermoelectric Power of Bismuth Nanowires, *Phys. Rev. B* 59, 12579 – 12583 (1999).
4. R.Saleh, P.Thomas, and I.P.Zvyagin, Internal Currents in Multi-Layer Structures, *Superlattices and Microstructures* **10**(1), 59 – 62 (1991).
5. J.P.Heremans, Low-Dimensional Thermoelectricity, *Acta Physica Polonica* 108,609 – 634 (2005).
6. G.S.Nolas, J.Poon, and M.G.Kanatzidis, Recent Developments in Bulk Thermoelectric Materials, *Mater. Res. Soc. Bull*. 31, 199 – 205 (2006).

7. Y.V.Ivanov, Ballistic Thermoelectric Transport in a Lattinger Liquid, *J. Phys. Cond. Matter.* **22**(24), 245602 (2010).
8. A.Weathers, L.Shi, Thermal Transport Measurement Techniques for Nanowires and Nanotubes, arXiv:1504.05128 [cond-mat.mes-hall], 20 Apr 2015.
9. Arden L.Moore, Michael T.Pettes, Feng Zhou, and Li Shi, Thermal Conductivity Suppression in Bismuth Nanowires, *J. Appl. Phys*. 106, 034310 (2009).
10. Jong Wook Roh, Kedar Hippalgaonkar, Jin Hee Ham, Renkun Chen, Ming Zhi Li, Peter Ercius, Arun Majumdar, Woochul Kim, and Wooyoung Lee, Observation of Anisotropy in Thermal Conductivity of Individual Single-Crystalline Bismuth Nanowires, *ACS Nano* **5**(5), 3954 – 3960 (2011).
11. N.B.Brandt, V.S.Yegorov, M.Yu.Lavrenyuk, E.Ya,Minina, and A.M.Savin, Specific Features of Thermopower and Resistance at Electronic Topological Transitions in Bismuth and its Alloys, *JETP* **89**(6), 2257 – 2269 (1985).
12. N.B.Brandt, V.A.Kulbachinskii, N.Ya.Minina, and V.D. Shirokikh, Change in the Band Structure of *Bi* and $Bi_{1-x}Sb_x$ at Deformations of Uniaxial Tension Type, *JETP* 78(3), 1114 – 1131 (1980).
13. D.Gitsu, L.Konopko, A.Nikolaeva, and T.Huber, Pressure-Dependent Thermopower of Individual Bi Nanowires, *Appl. Phys. Lett*. 86, 10210 (2005).
14. N.B.Brandt, D.V.Gitsu, A.A.Nikolaeva, and Ya.G.Ponomarev, Investigation of Size Effects in Thin Cylindrical Bismuth Single Crystals in a Magnetic Field, Sov. Phys. *JETP* **45** (6), (1977).
15. A.A.Nikolaeva, L.A.Konopko, A.K.Tsurkan, and T.E.Huber, Thermoelectric Properties of Single-Crystal $Bi-Sn$ Wires with Different Crystallographic Orientation at Elastic Strains, *J. Thermoelectricity* 3, 41 – 59 (2009).
16. A.Nikolaeva, L.Konopko, T.Huber, G.Para, and A.Tsurkan, Effect of Weak and High Magnetic Fields in Longitudinal and Transverse Configurations on Magneto-Thermoelectric Properties Quantum *Bi*-wires, *J. Surface Engineering and Applied Electrochemistry* **50**(1), 57 – 62 (2014).
17. P.P.Bodiul, V.F.Garabadzhiu, E.P.Kondria, and A.A.Nikolaeva, Method for Creation of Elastic Anisotropic Deformation of Single Crystals under their Uniaxial Tension, *Certificate of Authorship № 48100511/9 of 30.01.91.*
18. G.I.Para, Thermomagnetic and Thermoelectric Properties of Nano- and Microwires Based on Bi Semimetal, *Doctoral Thesis in Physics and Mathematics, Kishinev, 2012, 197 p.*
19. D.V.Gitsu, T.E.Huber, L.A.Konopko, and A.A.Nikolaeva, Size Effects in Quantum Single Crystal Bismuth Wires in Glass Cover, *J. Nanoelectron. Optoelectron*. **4**(1), 40 – 51 (2009).
20. N.B.Brandt, V.A.Kulbachinskii, N.Ya.Minina, and V.D. Shirokikh, Change in the Band Structure of *Bi* and $Bi_{1-x}Sb_x$ at Deformations of Uniaxial Tension Type, *JETP* 78(3), 1114 – 1131 (1980).
21. Yu.P.Gaidukov, N.P.Danilova, and M.B.Scherbina-Samoilova, Strength and Electric Properties of Bismuth Whiskers, *Low Temperature Physics* **4**(2), 250 – 255 (1978).
22. N.A.Redko, Thermal Conductivity of Bismuth Based Alloys under Combined Phonon-Impurity Phonon Scattering, *Letters to JETP* 16 (22), 52 – 56 (1990).

Submitted 10.07.2015.

V.A.Romaka[1,2], P.Rogl[3], L.P.Romaka[4], Yu.V.Stadnyk[4], D. Kaczorowski[5], V.Ya. Krayovskyy[2], O.I.Lakh[6]

[1] Ya. Pidstryhach Institute for Applied Problems of Mechanics and Mathematics National Academy of Sciences of Ukraine, 3-b, Naukova Str., Lviv, 79060, Ukraine;
[2] National University "Lvivska Polytechnika", 12, S.Bandera Str., Lviv, 79013,Ukraine;
[3] Universität Wien, 42, Währinger Str., A-1090, Wien, A-1090, Österreich;
[4] Ivan Franko National University of Lviv, 6, Kyryla and Mefodiya Str., 79005, Lviv, Ukraine;
[5] W.Trzebiatowski Institute of Low Temperature and Structural Research Polish Academy of Sciences, 2, Okolna Str., Wroclaw, 50-950 Poland
[6]Science and Production Company (NVO) "Thermoprylad", 3-b, Naukova Str., Lviv, 79060, Ukraine

THE STUDY OF STRUCTURAL, ENERGY AND KINETIC CHARACTERISTICS OF $Hf_{1-x}Y_xNiSn$ THERMOELECTRIC MATERIAL

The crystal and electronic structures, temperature and concentration dependencies of resistivity, the Seebeck coefficient and magnetic susceptibility of the $Hf_{1-x}Y_xNiSn$ thermoelectric material were studied in the ranges $T = 80 \div 400$ К К, $x = 0.01 \div 0.30$. The mechanism of simultaneous generation of defects of acceptor nature was established. They change the compensation ratio of material and determine the mechanism of conduction.
Keywords: electronic structure, resistivity, Seebeck coefficient.

Introduction

Performance optimization of $Hf_{1-x}Lu_xNiSn$ thermoelectric material obtained by doping of *n-HfNiSn* intermetallic semiconductor with the atoms of rare-earth *Lu* metal [1], which will provide for high efficiency of thermal into electric energy conversion [2], revealed the non-reproducibility of material performance at high temperatures ($T \leq 1000$ K). It was established that in the process of doping there is a predictable generation of structural defects of acceptor nature in a crystal with substitution of *Hf* ($5d^26s^2$) atoms by *Lu* ($5d^16s^2$) atoms (*Lu* atoms possesses one $5d$ – electron less than *Hf*), and an uncontrolled generation of vacancies in the position of *Sn* (4*b*) atoms. Exactly uncontrolled generation of *Sn* structural defects (vacancies), apart from redistributing the electron density, accounts for the non-reproducibility of $Hf_{1-x}Lu_xNiSn$ performance, as long as at temperatures $T \leq 1000$ K vacancies are the cores of localization of uncontrolled defects. It was assumed that one of the reasons for generation of vacancies is deformation of $Hf_{1-x}Lu_xNiSn$ unit cell, caused by the difference in atomic radii of *Hf* ($r_{Hf} = 0.158$ nm) and *Lu* ($r_{Lu} = 0.173$ nm).

On the other hand, in the investigation of $Zr_{1-x}Y_xNiSn$ thermoelectric material [3] obtained by doping with *Y* atoms of *n-ZrNiSn* intermetallic semiconductor whose characteristics are close to *n-HfNiSn*, no mechanism of uncontrolled generation of vacancies in the position of *Sn* (4*b*) atoms was revealed. And this is despite the fact that the difference in atomic radii of *Zr* ($r_{Zr} = 0.1602$ nm) and *Y* ($r_Y = 0.180$ nm) is greater than in the case of *Hf* and *Lu* atoms, which causes even greater deformation of $Zr_{1-x}Y_xNiSn$ crystalline structure. And it means that generation of vacancies is not caused by deformation of $Hf_{1-x}Lu_xNiSn$ crystalline structure. This problem should be investigated further.

Based on the results of [3], an idea has started up to obtain a thermoelectric material with stable and reproducible characteristics by doping of *n-HfNiSn* intermetallic semiconductor with *Y* atoms. That is, like in the case of $Zr_{1-x}Y_xNiSn$ [3], one can expect that in $Hf_{1-x}Y_xNiSn$ crystal there will be also generated only structural defects of acceptor nature with a substitution of *Hf* atoms by *Y* ($4d^15s^2$) atoms (*Y* atom possesses one $5d$ – electron less than *Hf* atom). *The purpose* of the paper is to study conduction mechanisms of *Y*-doped *n-HfNiSn*, which will allow predicting the behaviour of the kinetic characteristics of $Hf_{1-x}Y_xNiSn$ and study the conditions of obtaining a heat-resistant material with high efficiency of thermal into electrical energy conversion [1, 4].

Investigation procedures

The object to be investigated included crystalline structure, electron density distribution (DOS), the magnetic, electrokinetic and energy characteristics of $Hf_{1-x}Y_xNiSn$. The samples were synthesized in the laboratory of Institute for Physical Chemistry, Vienna University. The X-ray structural analysis (powder method) was used to obtain the data arrays (diffractometer Guinier-Huber image plate system, $CuK\alpha_1$), and Fullprof program [5] was employed for the calculation of structural characteristics. The chemical and phase compositions of samples were controlled by microprobe analyzer (EPMA, energy-dispersive X-ray analyzer). The electronic structure calculations were performed by the Korringa-Kohn-Rostoker (KKR) method in coherent potential approximation (CPA) and local density approximation (LDA) [6] with the use of Moruzzi-Janak-Williams exchange-correlation potential [7]. The accuracy of calculating the position of the Fermi level ε_F is ± 8 meV. The temperature and concentration dependences of the electrical resistivity (ρ) and the Seebeck coefficient (α) were measured with respect to copper and magnetic susceptibility (χ) (Faraday method) of $Hf_{1-x}Y_xNiSn$ samples in the ranges: $T = 80 \div 400$ K, $N_D^Y \approx 1.9 \cdot 10^{20}$ cm^{-3} ($x = 0.01$) ÷ $5.7 \cdot 10^{21}$ cm^{-3} ($x = 0.30$) and the magnetic field intensity $H \leq 10$ kE.

Research on the structural peculiarities of $Hf_{1-x}Y_xNiSn$

The microprobe analysis of the concentration of atoms on the surface of $Hf_{1-x}Y_xNiSn$ samples has shown their conformity to the initial charge compositions, which is one of the experimental proofs of the predicted substitution of *Hf* atoms by *Y*. In turn, X-ray phase and structural analyses have revealed no traces of other phases in all $Hf_{1-x}Y_xNiSn$ samples up to and including $x = 0.30$. As was expected, replacement of smaller-size *Hf* atoms by larger-size *Y* atoms leads to increase in the values of unit cell period $a(x)$ of $Hf_{1-x}Y_xNiSn$ (Fig. 1). The fact that the values of $a(x)$ in the concentration range $Hf_{1-x}Y_xNiSn$, $x = 0 \div 0.30$ practically coincide with the calculated ones points to realization of substitutional solid solution. A deviation of the values of unit cell period $a(x)$ from the linear dependence at $x > 0.30$ fixes the limit for the existence of $Hf_{1-x}Y_xNiSn$ solid solution. The $Hf_{1-x}Y_xNiSn$ samples at $x > 0.30$ are two-phase.

Investigations have also confirmed the result of [8] as regards crystal structure disorder of base semiconductor *n-HfNiSn*, the key point of which lies in a partial, up to ~ 1%, occupancy by *Ni* ($3d^84s^2$) atoms of the crystallographic position 4*a* of *Hf* atoms (*Ni* atoms possesses a larger number of *d*-electrons than *Hf* atom), which creates structural defects of donor nature (“a priori” doping with donors [4]), and electrons are the majority carriers.

Refinement of $Hf_{1-x}Y_xNiSn$ crystalline structure by powder method with a simultaneous refinement of the isotropic parameters of atomic substitution and occupancy of (4*a*) crystallographic

position of *Hf* has shown that the lowest value of coefficient of mismatch between a model of crystalline structure and an array of Bragg reflections was obtained for a model where the occupancy of position of *Hf*(*Y*) atoms for $x \geq 0.01$ is 100%. In other words, the introduced *Y* atoms put into order $Hf_{1-x}Y_xNiSn$ crystalline structure ("heal" structural defects) by displacement of *Ni* atoms from the position of *Hf* (4*a*) atoms. In turn, ordering of $Hf_{1-x}Y_xNiSn$ crystalline structure makes it resistant to temperature and time changes, which creates prerequisites for preparation of material with stable and reproducible characteristics.

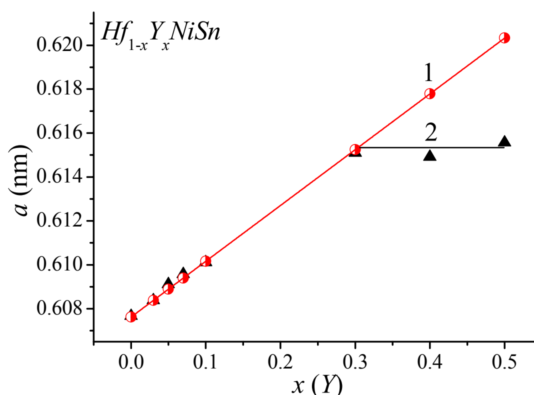

Fig. 1. Change in the values of unit cell period a(x) of $Hf_{1-x}Y_xNiSn$:
1 – calculation; 2 – experiment.

Apart from the structural peculiarities, ordering of $Hf_{1-x}Y_xNiSn$ crystalline structure contributes essentially to the redistribution of the electron density of states. Thus, while in the initial *HfNiSn* compound there exist structural defects of donor nature as a result of displacement of up to ~1% of *Hf* atoms by *Ni* atoms [8], the process of semiconductor doping with *Y* atoms and ordering of crystalline structure is accompanied, on the one hand, by the reduction in the number of donors, as long as *Ni* atoms leave the position of *Hf* atoms. On the other hand, as long as *Y* atom has one 5*d* – electron less than *Hf* atom, structural defects of acceptor nature are generated in the crystal.

Therefore, in $Hf_{1-x}Y_xNiSn$, in the concentration range $x = 0 \div 0.01$ there is a simultaneous reduction of the number of donors (*Ni* atoms leave position 4*a* of *Hf* atoms) and increase in the number of acceptors (*Y* atoms occupy the position of *Hf* atoms). In this case, doping of *n-HfNiSn* semiconductor with lower concentrations of acceptor impurity will be accompanied, as expected, by increase in semiconductor compensation ratio (the ratio between donors and acceptors) [4]. With concentrations of $x > 0.01$, when *Ni* atoms will leave position 4*a* of *Hf* atoms, the concentration of acceptors in a crystal will increase, the type of majority carriers will change and the compensation ratio will decrease.

Research on the electron structure of $Hf_{1-x}Y_xNiSn$

To predict the behaviour of Fermi level ε_F, the energy gap ε_g and the kinetic characteristics of *n-HfNiSn* doped with *Y*, the electron density of states (DOS) of $Hf_{1-x}Y_xNiSn$, $0 \leq x \leq 0.10$ was calculated (Fig. 2*a*). Taking into account the results of structural investigations that introduction into *HfNiSn* compound of *Y* atoms puts into order its crystalline structure, calculation of DOS was performed for the case of ordered variant of $Hf_{1-x}Y_xNiSn$ structure. As we can see from Fig. 2*a*, on introducing into *n-HfNiSn* of minimum attainable in experiment concentrations of acceptor impurity *Y*, Fermi level ε_F (dashed line in Fig.2*a*) starts drifting from conduction band ε_c, spaced ~81.3 meV from

it [8], to the midgap ε_g (shaded area in Fig. 2*a*), and then to the valence band ε_V which will be crossed by it at certain *Y* concentrations.

When crossing by Fermi level ε_F of the midgap ($x \approx 0.025$) and its further motion to valence band, the semiconductor changes its conductivity type, and holes become the majority carriers. Note that apart from the drift of Fermi level ε_F caused by a change in semiconductor compensation ratio, there is also a reduction in the energy gap ε_g from the values of $\varepsilon_g(x = 0) = 514.3$ meV to $\varepsilon_g(x = 0.10) = 426$ meV.

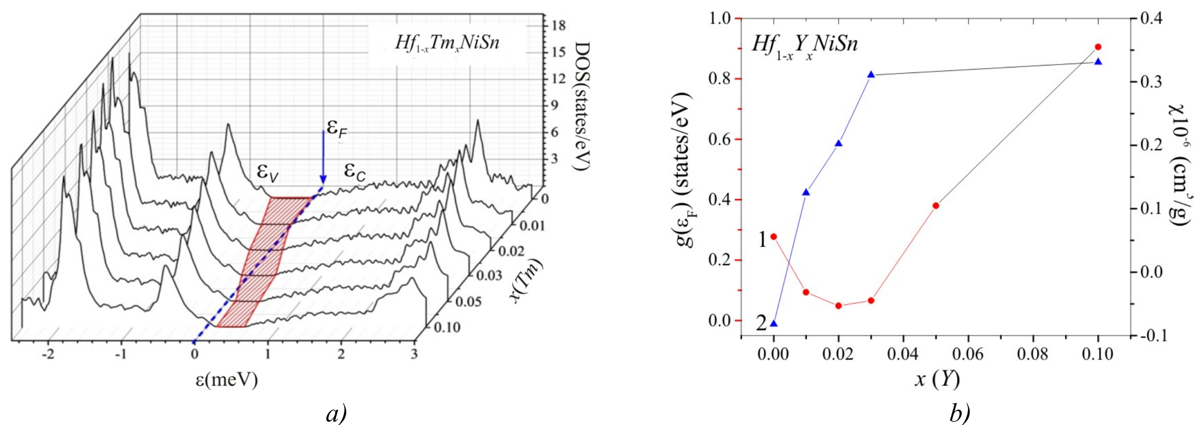

Fig. 2. Calculation of the electron density of states DOS (a) and density of states at Fermi level $g(\varepsilon_F)$ (curve 1) and change in the values of magnetic susceptibility χ (curve 2) (b) $Hf_{1-x}Y_xNiSn$.

The predicted behaviour of Fermi level ε_F is accompanied by interesting behavior of the density of states at Fermi level $g(\varepsilon_F)$ (Fig. 2*b*). Thus, doping of *n-HfNiSn* with acceptor impurity *Y* leads, as expected, to density of states reduction at Fermi level, and minimum dependence $g(\varepsilon_F)$ corresponds at ($x \approx 0.025$) to crossing by Fermi level ε_F of the midgap ε_g of $Hf_{1-x}Y_xNiSn$. At *Y* concentrations, when Fermi level ε_F will cross the midgap and will be approaching the valence band ε_V, the density of states at Fermi level will increase in a predictable fashion.

The above results of calculations of a change in the density of state at Fermi level $g(\varepsilon_F)$ agree with the results of experimental measurements of magnetic susceptibility of χ $Hf_{1-x}Y_xNiSn$ (Fig. 2*b*, curve 2). The research has shown that samples of $Hf_{1-x}Y_xNiSn$, $x > 0.01$, are Pauli paramagnetics, where the magnetic susceptibility is defined exceptionally by electron gas in proportion to density of states at Fermi level. As can be seen from Fig. 2*b*, dependence $\chi(x)$ at $x > 0.03$ drastically changes the slope and achieves plateau, which we attribute, according to calculations, exactly to a change in the density of states at Fermi level $g(\varepsilon_F)$ when crossing of valence band by Fermi level. Note that *n-HfNiSn* semiconductor is not Pauli paramagnetic, but a weak diamagnetic, as testified by the negative values of magnetic susceptibility: $\chi(x = 0) = -0.082$ cm^3/g [4]. So, supposedly, the growth of dependence $\chi(x)$ in the concentration area $x = 0 \div 0.01$ cannot be attributable to increase in the density of states at Fermi level.

Calculation of the electronic structure of $Hf_{1-x}Y_xNiSn$ allows predicting its characteristics, in particular, the Seebeck coefficient, the electric resistivity, etc. To calculate the Seebeck coefficient α, use was made of ratio [9] as a working formula [9]:

$$\alpha = \frac{2\pi^2}{3}\frac{k^2 T}{e}\left(\frac{d}{d\varepsilon}\ln g(\varepsilon_F)\right),$$

where $g(\varepsilon_F)$ is density of states at Fermi level. As an example, Fig. 3 shows a change in the values of the Seebeck coefficient $\alpha(x)$ of $Hf_{1-x}Y_xNiSn$ at different temperatures. It is seen that at different

concentrations of *Y* one can get in thermoelectric material high positive and negative values of the Seebeck coefficient and conductivity, which is one of the reasons for obtaining high thermoelectric figure of merit values.

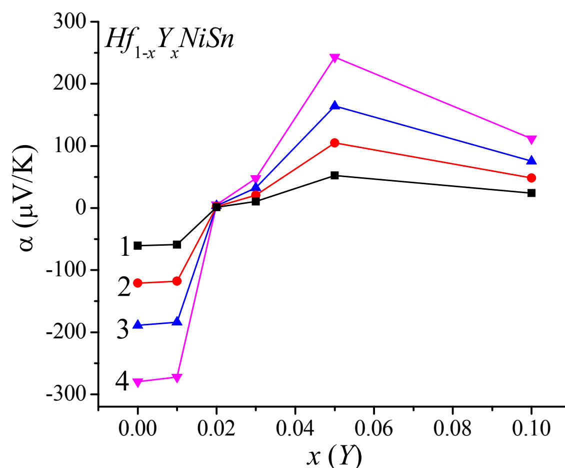

Fig. 3.Calculation of the change in the Seebeck coefficient of $Hf_{1-x}Y_xNiSn$ at temperatures: 1 – 80; 2 – 160; 3 – 250; 4 – 380 K.

Thus, the results of calculation of the electron density of states of $Hf_{1-x}Y_xNiSn$ based on the results of structural research prove the predicted acceptor nature of structural defects. The results of experimental investigations given below will show correspondence of calculated results to real processes in thermoelectric material.

Research on the electrokinetic and energy characteristics of $Hf_{1-x}Y_xNiSn$

The temperature dependences of resistivity $\ln\rho(1/T)$ and the Seebeck coefficient $\alpha(1/T)$ for $Hf_{1-x}Y_xNiSn$, $x = 0 \div 0.30$, are typical for semiconductors (Fig. 4) and vary in conformity with the results of calculation of density of states distribution. We can see that in $Hf_{1-x}Y_xNiSn$, $x = 0 \div 0.10$ samples, on the $\ln\rho(1/T)$ dependences there are high-temperature activation areas, which points to arrangement of Fermi level ε_F in the energy gap, from where charge carriers are activated from continuous energy band. Thus, the negative values of the Seebeck coefficient at $x = 0$ are understandable and related to “a priori doping” of base *n-HfNiSn* semiconductor with donors (position of *Hf* atoms up to ~1% is occupied with *Ni* atoms) [8].

In turn, the negative values of the Seebeck coefficient for the case of $x = 0.01$ (Fig. 4, 5*b*) testify that concentration of generated defects of acceptor nature with substitution of *Hf* atoms by *Y* atoms is lower than concentration of defects of donor nature due to disordered structure of *HfNiSn* compound, hence, the Fermi level ε_F is arranged on the impurity donor band and closer to conduction band.

For cases of $Hf_{1-x}Y_xNiSn$, $x = 0.02 \div 0.10$, the positive values of the Seebeck coefficient indicate that concentration of defects of acceptor nature has exceeded that of donor nature, and Fermi level ε_F is now fixed on the impurity acceptor band generated in a crystal as a result of substitution of *Hf* atoms by *Y*. High-temperature activation area on $\ln\rho(1/T)$ dependences reflects thermal ejection of holes from acceptor to valence band, which is accompanied by increase in the number of free holes. Instead, the metallic variation of $\ln\rho(1/T)$ dependence and positive coefficient values for $Hf_{1-x}Y_xNiSn$, $x = 0.30$, testify that Fermi level ε_F has crossed the valence band ceiling, as was predicted by calculations of electron structure of $Hf_{1-x}Y_xNiSn$, namely, dielectric-metal transition has occurred [9]. In so doing, it

must be understood that $Hf_{1-x}Y_xNiSn$, $x = 0.30$ sample will continue to be a semiconductor, and the mechanism of activation conduction in the investigated temperature range is absent due to the entrance of Fermi level ε_F into valence band.

At first sight, the behaviour of $\rho(x)$ dependence in the area of $x = 0 \div 0.10$ (Fig. 5*a*) is somewhat contradictory. Thus, introduction into *HfNiSn* compound of the lowest in experiment concentration of *Y* atoms is attended with a drastic decrease in the electric resistivity values, for instance, at 160 K, from the values of $\rho(x = 0) = 487.2$ μΩ·m to $\rho(x = 0.01) = 121.1$ μΩ·m.

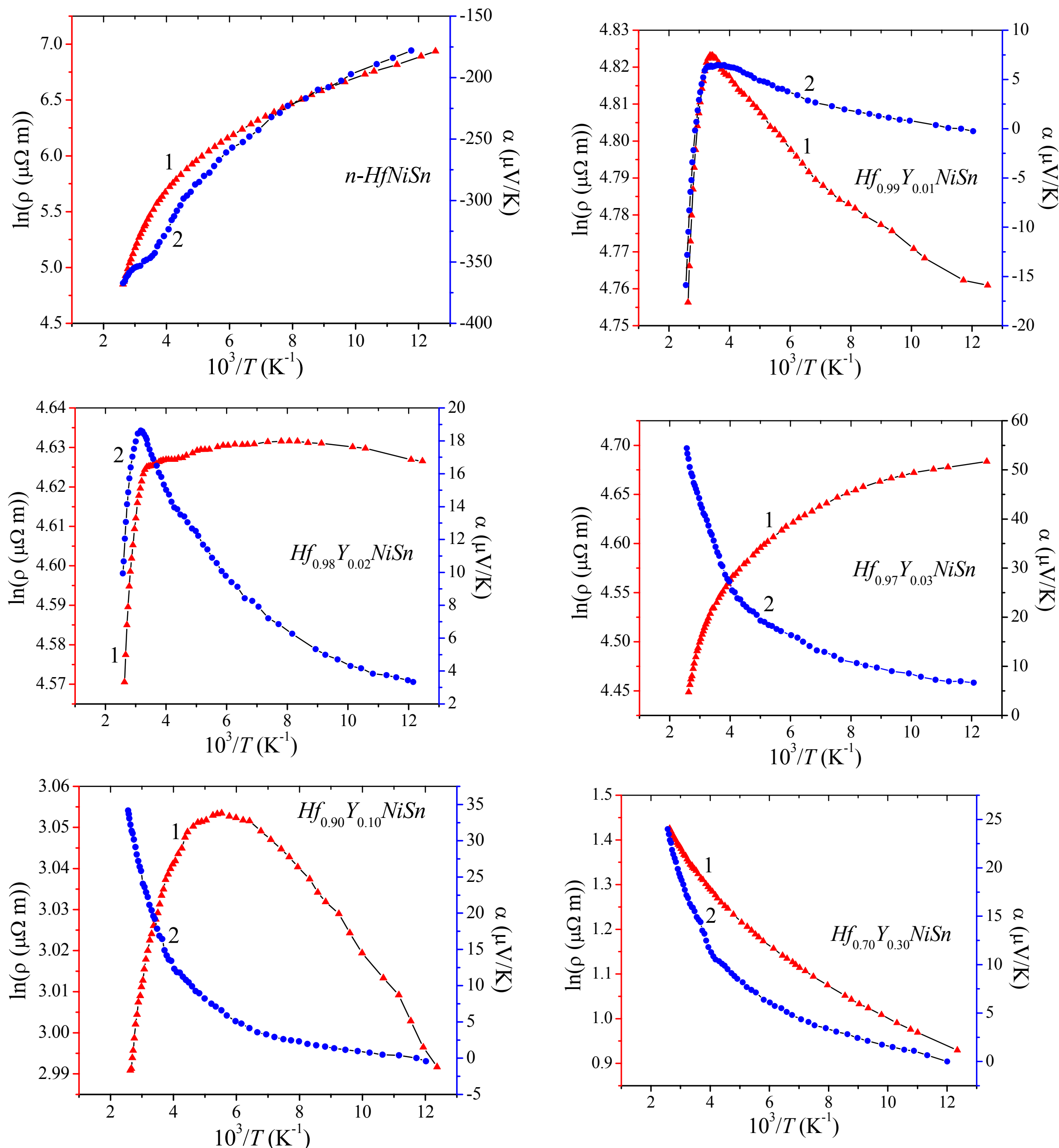

Fig. 4. Temperature dependences of the electrical resistivity and the Seebeck coefficient of $Hf_{1-x}Y_xNiSn$.

The point is that the concentration of acceptors generated in $Hf_{1-x}Y_xNiSn$ on introducing the lowest concentration of *Y* ($x = 0.01$) is too high, and we jump over the concentration gap whereby

Fermi level ε_F would move from conduction band edge to the midgap, which would be accompanied by growth of electric resistivity values due to reduction of density of states at Fermi level $g(\varepsilon_F)$ in the n-type semiconductor doped with acceptors. Thus, with the lowest concentration of acceptor impurity Y ($x = 0.01$) the values of the Seebeck coefficient become positive. For instance, the values of the Seebeck coefficient at 160 K vary from $\alpha(x=0) = -252.5$ μVK^{-1} to $\alpha(x=0.01) = 3.4$ μVK^{-1}, which points to increase in the concentration of holes as Fermi level ε_F approaches valence band. That is, in $Hf_{1-x}Y_xNiSn$, $x = 0.01$, the concentration of acceptors is sufficient to change the type of semiconductor conductivity.

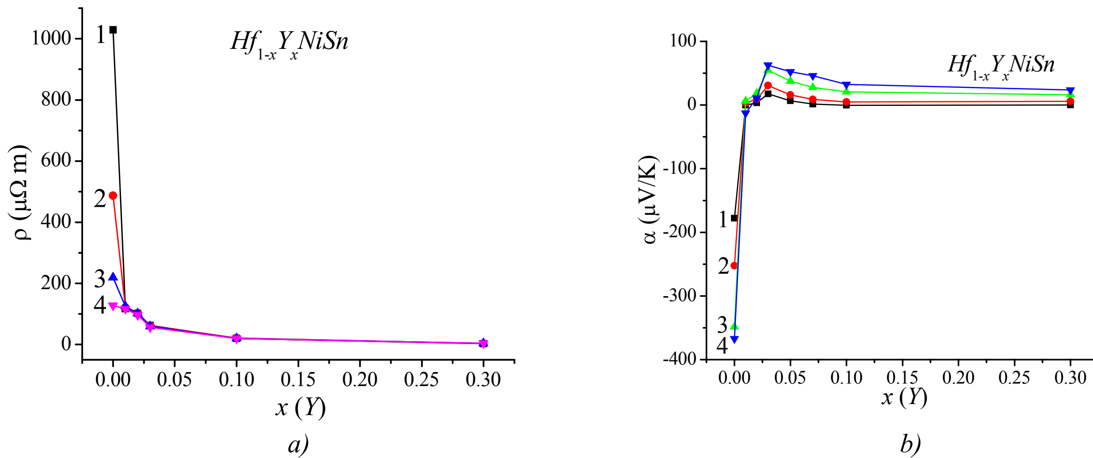

Fig. 5. Change in the values of electric resistivity $\rho(x)$ *(a) and the Seebeck coefficient* $\alpha(x)$ *(b) of* $Hf_{1-x}Y_xNiSn$ *at temperatures: 1 – 80 K; 2 – 160 K; 3 – 250 K; 4 – 380 K.*

In this context it is interesting to trace the character of change in the energy characteristics of $Hf_{1-x}Y_xNiSn$ obtained from the experimental investigations (Fig. 6), which also allow for the conclusion that introduction of Y impurity atoms into the structure of $HfNiSn$ compound is accompanied by generation of structural defects of acceptor-like nature. From the activation areas of dependences $\ln\rho(1/T)$ (Fig. 4) the values of activation energies were calculated from Fermi level ε_F to percolation level of conduction band $\varepsilon_1^{\rho}(x)$, and from the activation areas of dependences $\alpha(1/T)$ (Fig. 4) – the values of activation energies $\varepsilon_1^{\alpha}(x)$ that yield the values of modulation amplitude of continuous energy bands [4].

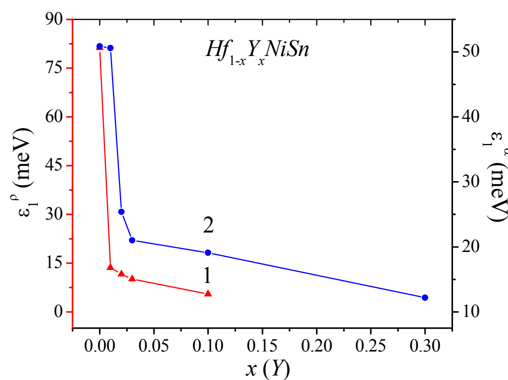

Fig. 6. Change in activation energies $\varepsilon_1^{\rho}(x)$ *(1) and* $\varepsilon_1^{\alpha}(x)$ *(2) of* $Hf_{1-x}Y_xNiSn$.

From Fig. 6 it is evident that doping of semiconductor results in the reduction of activation energy y $\varepsilon_1^{\rho}(x)$. It is important to explain that the value of energy $\varepsilon_1^{\rho}(x)$ for *n-HfNiSn* reflects the energy gap between the position of Fermi level ε_F and conduction band edge. At the same time, the

values of activation energy $\varepsilon_1^{\rho}(x)$ for the lowest and all subsequent concentrations of *Y* atoms reflect the energy gap between the position of ε_F and conduction band edge. From the almost linear behaviour of $\varepsilon_1^{\rho}(x)$ in the concentration area $x = 0.01 \div 0.10$ one can estimate the velocity of Fermi level ε_F motion to valence band edge: $\Delta\varepsilon_F / \Delta x \approx 0.9$ meV/% *Y*. This result is quite logical, as long as we increase the concentration of impurity *Y* by the linear law, which by the same law generates structural defects of acceptor nature in $Hf_{1-x}Y_xNiSn$ crystal.

A change in the values of activation energy $\varepsilon_1^{\alpha}(x)$ proportional to modulation amplitude of continuous energy bands in $Hf_{1-x}Y_xNiSn$ seems to be interesting. From Fig. 6 it is seen that in the case of undoped *n-HfNiSn* semiconductor the modulation amplitude is $\varepsilon_1^{\alpha}(x=0) = 50.9$ meV, and introduction into *n*-type semiconductor of the lowest in experiment concentration of *Y* impurity practically does not change the semiconductor compensation ratio, as indicated by the modulation amplitude $\varepsilon_1^{\alpha}(x=0.01) = 50.6$ meV. This result would be discrepant, if it were not for the change in the type of majority carriers. However, as shown above, the concentration of *Y* $x = 0.01$ is sufficient for semiconductor overcompensation, hence the proximity of values $\varepsilon_1^{\alpha}(x=0) = 50.9$ meV and $\varepsilon_1^{\alpha}(x=0.01) = 50.6$ meV is of random character.

Adding to now *p*-type $Hf_{1-x}Y_xNiSn$, $x = 0.01$ semiconductor of *Y* acceptor impurity naturally changes compensation ratio, that is, the difference in the number of ionized acceptors and donors will increase. This effect is manifested in the reduction of modulation amplitude values to $\varepsilon_1^{\alpha}(x=0.02) = 25.4$ meV. It is clear that further doping of *p*-type semiconductor with acceptor impurity will only reduce the compensation ratio, and the values of modulation amplitude of continuous energy bands $\varepsilon_1^{\alpha}(x)$ will be reduced either (Fig. 6).

Conclusions

Thus, as a result of integrated research on the crystalline and electron structures, the kinetic and magnetic characteristics of *Y*-doped *n-HfNiSn* intermetallic semiconductor, the mechanisms of generation of only structural defects of acceptor nature have been revealed, that change compensation ratio and determine electric conduction mechanisms. The investigated $Hf_{1-x}Y_xNiSn$ solid solution is a promising thermoelectric material, and ordered crystalline structure is a guarantee of stability and reproducibility of characteristics.

The `work was performed in the framework of grants of the National Academy of Sciences and Ministry of Education and Science of Ukraine, № 0113U007687 і № 0114U005464.

References

1. V.A.Romaka, P.Rogl, V.V.Romaka, D.Kaczorowski, Yu.V.Stadnyk, R.O.Korh, V.Ya.Krajovskii, and T.M.Kovbasyuk, Features of the Band Structure and Conduction Mechanisms of *n*-HfNiSn Semiconductor Heavily Lu-Doped, *Semiconductors* **49**(3), 290 – 297 (2014).
2. L.I.Anatychuk, *Thermoelements and Thermoelectric Devices* (Kyiv: Naukova Dumka, 1979), 768 p.
3. V.V.Romaka, E.K.Hlil, O.V.Bovhira, L.P.Romaka, V.M.Davydov, and R.V.Krayovskyy, Mechanism of Defect Formation in *n-ZrNiSn* heavily doped with Y atoms. I. Study of Crystalline and Electronic Structure, *Ukrainian Journal of Physics* **54**(11), 1120 – 1125 (2009).

4. V.A.Romaka, V.V.Romaka, and Yu.V.Stadnyk, *Intermetallic Semiconductors: Properties and Application* (Lviv:Lvivska Polytechnika, 2011), 488 p.
5. T.Roisnel, J.Rodriguez-Carvajal, WinPLOTR: a Windows Tool for Powder Diffraction Patterns Analysis, *Mater. Sci. Forum, Proc. EPDIC7* 378-381, 118 – 123 (2001).
6. M.Schruter, H.Ebert, H.Akai, P.Entel, E.Hoffmann, and G.G.Reddy, First-Principles Investigations of Atomic Disorder Effects on Magnetic and Structural Instabilities in Transition-Metal Alloys, *Phys. Rev. B* **52**, 188 – 209 (1995).
7. V.L.Moruzzi, J.F.Janak, and A.R.Williams, *Calculated Electronic Properties of Metals* (NY: Pergamon Press, 1978), 348 p.
8. V.Romaka, P.Rogl, L.Romaka, Yu.Stadnyk, A.Grytsiv, O.Lakh, and V.Krayovsky, Peculiarites of Structural Disorder in *Zr*- and *Hf*- Containing Heusler and Half-heusler Stannides, *Intermetallics* 35, 45 – 52 (2013).
9. H.Mott, T.Davis, *Electronic Processes in Non-Crystalline Substances* (Moscow: Mir, 1982), 368p.

Submitted 25.08.2015

S.F.Zaparov

S.F. Zaparov

Institute of Thermoelectricity of the NAS and MES of Ukraine,
1 Nauky str., Chernivtsi, 58029, Ukraine

COMPARATIVE ANALYSIS OF THE EFFICIENCY OF CUTTING BI-TE-BASED THERMOELECTRIC MATERIAL USING ELECTRIC EROSION METHOD AND WIRES WITH BOUND ABRASIVE

The problem of quality enhancement of thermoelectric cooling modules and generator modules whose legs comprise Bi_2Te_3- based semiconductor thermoelectric material continues to be relevant. On the one hand, quality enhancement and cost reduction of thermoelectric modules is attained by design solutions, on the other hand, by selection of manufacturing process and maintenance of the achieved reliability level in operation. The process of manufacturing semiconductor thermoelectric legs of n- and p-types is adequately tried and tested, and quality here is primarily assured by the level of technological equipment and staff qualification. Comparative analysis is performed of Bi_2Te_3- based thermoelectric material dimensional processing using electric spark method and diamond-coated wires. The optimal methods for cutting thermoelectric material (TEM) into discs and legs providing for the best quality with retention of high throughput are determined. The advantage of cutting method using a wire with bound abrasive is demonstrated.

Key words: TEM processing methods, TEM processing tools, benefits and drawbacks.

Introduction

In the manufacture of thermoelectric module legs (half-elements) the following process flowchart is widely used:

- preparation of thermoelectric material ingots;
- cutting of ingots into discs and discs into half-elements of *n*- and *p*-type thermoelectric materials by one of defect-free methods (electric erosion method with a wire electrode or mechanical method using a wire with bound or free abrasive, diamond discs).

Thermoelectric material cutting is associated with damaged layers. The properties of damaged layers are essentially different from the properties of the main material. These layers have a lot of defects, owing to which the figure of merit of thermoelectric material in the near-surface layer is considerably lower than in the bulk. Thus, each of the resulting legs is a parallelepiped enclosed by surface layer of material with degraded performance.

The purpose of the work is comparative analysis of thermoelectric material dimensional processing by two methods (electric erosion and diamond-coated wire), their advantages and shortcomings.

Electric erosion processing

Electric erosion processing is a controlled destruction of material by the electric discharges formed as a result of pulsed current flow between electrodes 1, 2 (Fig. 1) that are in the immediate vicinity from each other in liquid dielectric medium, that is, material processing through electric erosion. As a result of these

discharges, microparticles are knocked out of material to be taken away from the interelectrode gap by dielectric flush. Moreover, a dielectric acts as a catalyst of decay process, since at high discharge temperature in the zone of erosion it is vaporized. These methods include electric pulse, electric contact, high-frequency electric spark and electric spark processing.

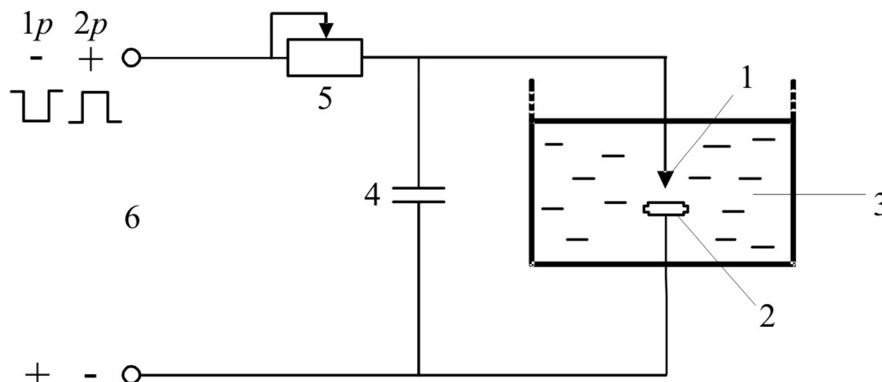

Fig. 1. Schematic of electric erosion processing of material:
1 – electrode tool, 2 – work material, 3 – discharge environment,
4 – capacitor, 5 – rheostat, 6 – supply source,
1p – electric spark processing mode, 2p – electric pulse processing mode.

For electric pulse processing electric pulses of long duration (500 – 10000 μs) are used, resulting in arc discharge. Electric pulse processing is reasonable to be used for primary machining of dies, turbine blades, profiled parts of heat-resistant alloys. This kind of processing is not used for thermoelectric materials due to very large depth of layers damage.

Electric contact processing is based on local heating of a billet at point of contact to electrode tool and removal of softened or even molten metal from processing zone by mechanical method, i.e. relative motion of the billet and tool. Pulse arc discharges serve as the source of heat in processing zone. Electric contact processing by fusion is recommended for large-size parts of carbon and alloyed steels, cast iron, non-ferrous alloys, refractory and special alloys. It is not recommended for processing of TEM due to strong violation of TEM properties in the near-surface layers.

High-frequency electric spark processing is used for increasing the accuracy and reducing the roughness of surfaces processed by electric erosion method. The method is based on the use of low-power electric pulses at a frequency of 100 – 150 kHz.

Electric spark processing employs pulse spark discharges between electrodes, one of which is a billet being processed (anode), and the other is a wire tool (cathode). Thermoelectric material based on Bi_2Te_3 serves as a billet. The surface of the tool is destructed, so the wire must be constantly stretched. The range of used wire tool diameters is 0.03 mm – 0.1 mm. Brass, molybdenum and tungsten can serve as the wire material. The use of brass can result in the penetration of electroactive impurities into thermoelectric material. Repeated use of wire tool is not recommended, since it will cause uncontrolled variation of cut material parameters and frequent break of the wire. It is necessary to use liquids that cool electrodes and stabilize the process of cutting thermoelectric material ingots into discs (Fig. 2).

The disadvantages of this method include: relatively low processing throughput, electrode wire wear, the use of mostly relaxation (i.e. depending on the state of interelectrode gap) pulse-generating circuits of duration 10 – 200 μs with the frequency of 2 to 5 kHz, the use of direct current polarity. On the processed surface of bismuth telluride-based thermoelectric material there appear near-surface damaged layers of depth 20 – 30 μm which reduce the figure of merit of legs. Therefore, removal of damaged layer by chemical etching is a mandatory operation.

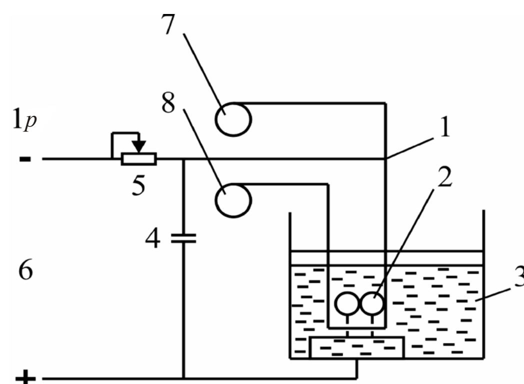

Fig. 2. Schematic of electric spark processing of TEM:
1 – wire tool, 2 – ingots (TEM), 3 – discharge environment,
4 – capacitor, 5 – rheostat, 6 – supply source, 7 – wire coil,
8 – spent wire coil, 1p-electric spark processing mode.

It should be kept in mind that electric erosion processing results in work space air contamination and, as a consequence, in environmental pollution, with harmful substances released in operation. Such substances are nitrogen dioxide, sulphur dioxide, carbon monoxide, and xylol.

Cutting by wires with bound abrasive

The method of cutting by wires with bound abrasive allows cutting Bi_2Te_3 ingots into discs, discs into legs of *n*- and *p*-types (Fig. 3).

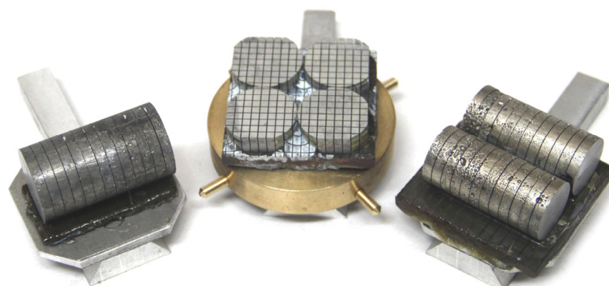

Fig. 3. Disks and branch of n-and p-type.

Cutting tool is based on a replaceable frame (Fig. 4) with a uniformly stretched diamond-coated wire. The winding pitch of tungsten wire is set by the grooves of spacer bars.

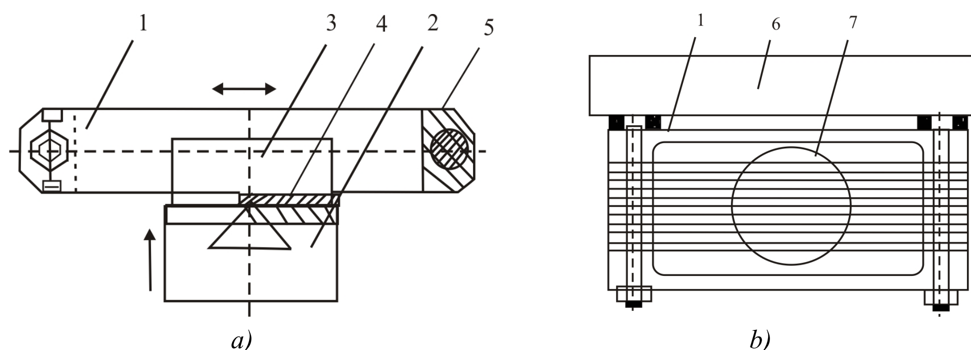

Fig. 4. Replaceable frame coated with diamond grains: 1 – frame, 2 – table,
3 – TEM, 4 – gasket, 5 – spacer bars, 6 – carriage, 7 – wire coated with diamond grains.

Cutting layer on the wire is formed by galvanic deposition of synthetic diamond grains of size 40/28. As a metal binder, nickel is used.

As compared to electric spark method, wire cutting yields cut discs and *n*- and *p*-type legs with much smaller structural damages on the surface of cut material. By virtue of low thermodynamic voltages that arise in destruction zone, the depth of damaged thermoelectric material layers does not exceed 10 – 25 μm.

Optimal cutting is 1 mm/min. A specially developed wire cutting machine Altec–13005M (Fig. 5) assures high throughput with a simultaneous use of 4 cutting tools.

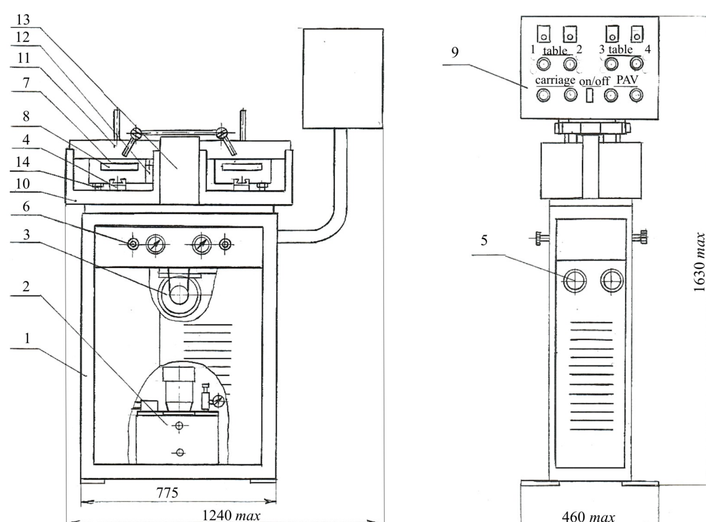

Fig. 5. Wire cutting machine Altec – 13005M.
1 – bed, 2 – hydro station, 3 – main drive, 4 – tables with hydraulic drives,
5 – table lift-lowering servodrive motors, 6 – controllers of table delivery pressure,
7 – carriage with hydrostatic guides, 8 – cutting frame with deposited diamonds,
9 – control panel, 10 – tray, 11 – left lid, 12 – protective angle of left tray,
13 – case, 14 –cutting depth microscrews.

During 8 hours of machine operation when cutting discs of *n*- and *p*-type thermoelectric material of diameter 24.0 mm and thickness 1.5 mm one can get at least 210000 half-elements of section 1.4 × 1.4 mm^2.

Control cuts made it possible to determine waste ratio in the process of cutting thermoelectric material discs ∅ 24.00 mm and thickness 1.5. mm into legs in powder form, and on washing and rejecting – in solid state.

Table

Size of legs	1.0×1.0×1.5 mm
Number of discs 1 pcs	weight 5 g.
Number of cuts	19
Yield ratio 283 pcs.	weight 3.02 g. 60.4%
Total amount of waste	weight 1.98 g. 39.6%
Solid waste	weight 0.34 g. 6.8%
Powder waste	weight 1.64 g. 32.8%
Size of legs	1.4×1.4×1.5 mm
Number of discs 1 pcs.	weight 5 g.
Number of cuts	14
Yield ratio 143 pcs.	weight 3.23 g. 64.6%
Total amount of waste	weight 1.77 g. 35.4%
Solid waste	weight 0.47 g. 9.4%
Powder waste	weight 1.3 g. 26%

Percentagewise, powder waste is considerably greater than solid waste. On termination of 8 – hour work of wire cutting machine Altec – 13005M, powder waste settles in waste tank in the form of pulp. To facilitate further recovery, the waste of *n*- and *p*-type thermoelectric materials should be separated.

Machine Altec – 13005M allows separate collection of *n*- and *p*-type powder waste that appears at cutting of Bi_2Te_3 – based thermoelectric material.

Conclusions

1. The advantage of method for cutting by wire with bound abrasive as compared to electric erosion method with dimensionless processing of alloys based on bismuth telluride on wire cutting machines Altec-13005M is high throughput, minimal depth of damaged layer, lower electric energy consumption per unit of product, low cost of cutting process.

2. A method for separate collection of powder waste of *n*- and *p*-type Bi_2Te_3 – based thermoelectric material in cutting for subsequent recovery is described.

3. The use of wire cutting machine assures ecological safety of processing, as long as in operation (unlike electric spark method) no toxic vapors of semiconductor material volatile components get into environment.

References

1. Z.Yu.Hotra, *Handbook on the Technology of Microelectronic Devices* (Lviv: Kamenyar, 1986), 287p.
2. B.M. Goltsman, V.A. Kudinov, and I.A. Smirnov, *Semiconductor Thermoelectric Materials Based on* Bi_2Te_3 (Moscow: Nauka, 1972), 320p.
3. Machine for Cutting of Semiconductor Materials Altec 13005 M. *Leaflet.*

Submitted 12.08.2015.

L.I. Anatychuk

L.I. Anatychuk[1,2], A.V. Prybyla[1]

[1]Institute of Thermoelectricity of the NAS and MES of Ukraine, 1, Nauky str., Chernivtsi, 58029, Ukraine
[2]Yu. Fedkovych Chernivtsi National University, 2, Kotsyubinsky str., Chernivtsi, 58000, Ukraine

A.V. Prybyla

OPTIMIZATION OF THERMAL CONNECTIONS IN LIQUID-LIQUID THERMOELECTRIC HEAT PUMPS FOR WATER PURIFICATION DEVICES OF SPACE APPLICATION

The paper presents the results of computer simulation of liquid-liquid thermoelectric heat pump. Multi-parameter computer optimization was used to determine parameters and arrangement of thermoelectric modules and heat exchangers to achieve the highest efficiency.

Key words: thermoelectric heat pump, computer simulation, liquid-liquid system.

Introduction

General characterization of the problem. The use of thermoelectric heat pumps in air-conditioning systems is related to their unique properties [1 – 5]: environmental friendliness (such devices have no toxic coolants); reliability (mechanical stability, long operational life); independence of orientation in space (possibility of work in the absence of gravitation) [6, 7].

An example of efficient application of thermoelectric heat pumps is provided by systems of water recovery from liquid biowaste on board of manned spacecrafts (urine, atmosphere humidity condensate, sanitary-hygiene water). Efficiency tests of such equipment on NASA stand have shown that in the most important parameters, namely specific power consumption, dimensions, weight and quality of distillate produced the system of water purification with thermoelectric heat pump outperforms known analogs of space application [4, 5].

However, new, more stringent requirements are imposed on such devices due to the possibility of their new applications (piloted missions for exploration of Mars and other planets). This is mainly related to the reduction of their weight, dimensions, as well as energy consumption for the operation of thermoelectric heat pump. The problem of further quality improvement of such devices is very complicated, since the attained values of their efficiency are close to boundary.

One of the methods for solving this problem is optimization of thermoelectric heat pump not as a whole, but of each thermoelectric module and heat exchanger in particular. This approach involves creating such optimal operating conditions for each thermoelectric converter that will assure the best efficiency values of the entire device.

This multi-factor problem was solved with the use of modern methods of computer object-oriented programming.

The purpose of this paper is efficiency increase of thermoelectric heat pump via multi-parameter computer optimization of the arrangement of thermoelectric modules and heat exchangers of the heat pump.

Physical model of thermoelectric heat pump

A physical model of thermoelectric heat pump is presented in Figs.1 – 3. It comprises heat exchangers 1 assuring passage of heat flux Q_h through the hot side of thermoelectric modules, thermoelectric modules 3 as such, heat exchangers 2 assuring passage of heat flux Q_c through the cold side of thermoelectric modules and a system of hydraulically bound channels 4 providing for circulation of liquid in the thermoelectric heat pump.

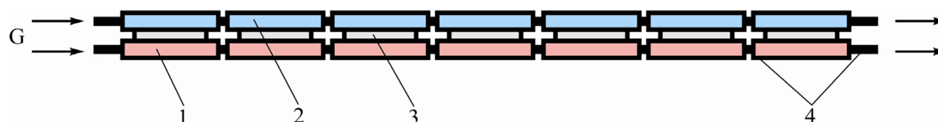

Fig. 1. The simplest physical model of thermoelectric heat pump.

In the simplest case this model represents series-connected hot 1 and cold 2 heat exchangers with thermoelectric modules 3 arranged between them (Fig. 1). However, practical implementation of such design is not always rational. This is due to considerable dimensions of such device.

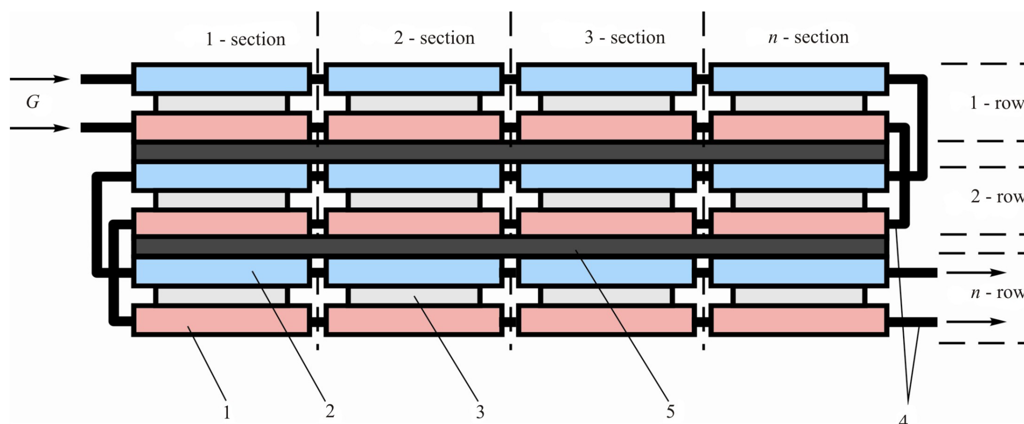

Fig. 2. Physical model of thermoelectric heat pump with thermal insulation.

In practice it is more convenient to connect heat exchangers 1 and 2 with thermoelectric modules 3 in rows with a different number of sections having thermal insulation 5 between them.

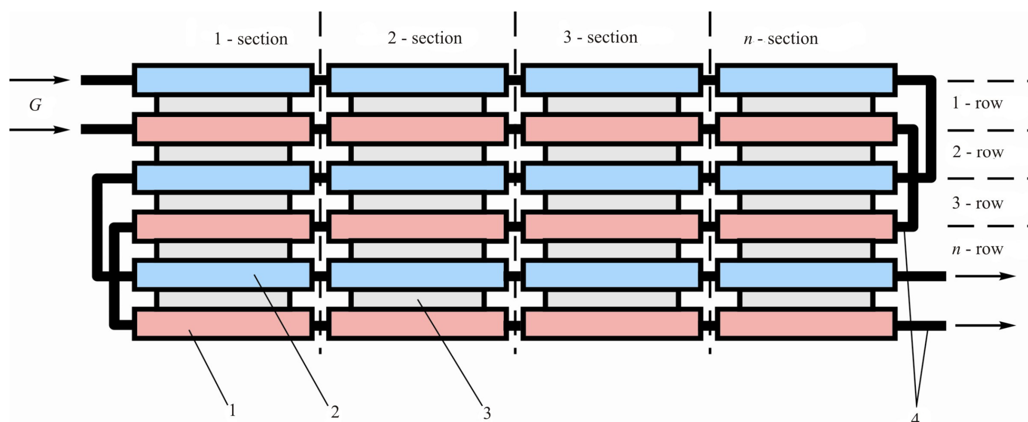

Fig. 3. Physical model of thermoelectric heat pump.

However, to reduce the weight and dimensions of such device, one can simplify the design proposed

in Fig. 2. In this case a row of heat exchangers will assure the operating conditions of two rows of thermoelectric modules (Fig. 3). Owing to this, the number of heat exchangers, hence, the weight and dimensions of such device will be reduced considerably.

Mathematical and computer description of the model

To describe heat and electric current fluxes, let us use the laws of conservation of energy

$$div\vec{E} = 0 \tag{1}$$

and electric charge

$$div\vec{j} = 0, \tag{2}$$

where

$$\vec{E} = \vec{q} + U\vec{j}, \tag{3}$$

$$\vec{q} = \kappa\nabla T + \alpha T\vec{j}, \tag{4}$$

$$\vec{j} = -\sigma\nabla U - \sigma\alpha\nabla T. \tag{5}$$

Here $\vec{E}$ is the energy flux density, $\vec{q}$ is the thermal flux density, $\vec{j}$ is the electric current density, U is the electric potential, T is a temperature, α, σ, κ are the Seebeck coefficient, electric conductivity and thermal conductivity.

With regard to (3) – (5) one can obtain

$$\vec{E} = -(\kappa + \alpha^2\sigma T + \alpha U\sigma)\nabla T - (\alpha\sigma T + U\sigma)\nabla U. \tag{6}$$

Then the laws of conservation (1), (2) will acquire the form:

$$-\nabla\left[(\kappa + \alpha^2\sigma T + \alpha U\sigma)\nabla T\right] - \nabla\left[(\alpha\sigma T + U\sigma)\nabla U\right] = 0, \tag{7}$$

$$-\nabla(\sigma\alpha\nabla T) - \nabla(\sigma\nabla U) = 0. \tag{8}$$

Nonlinear differential equations of second order in partial derivatives (7) and (8) determine the distribution of temperature T and potential U in thermoelements.

An equation describing the process of heat transport in the walls of heat exchangers in the steady-state case is written as follows:

$$\nabla(-k_1 \cdot \nabla T_1) = Q_1, \tag{9}$$

where k_1 is the thermal conductivity of heat exchanger walls, ∇T_1 is a temperature gradient, Q_1 is a heat flux.

The processes of heat-and-mass transfer of heat carriers in heat exchanger channels in the steady-state case are described by equations [8]

$$-\Delta p - f_D \frac{\rho}{2d_h} v|\vec{v}| + \vec{F} = 0, \tag{10}$$

$$\nabla(A\rho\vec{v}) = 0, \tag{11}$$

$$\rho A C_p \vec{v} \cdot \nabla T_2 = \nabla \cdot A k_2 \nabla T_2 + f_D \frac{\rho A}{d_h}|\vec{v}|^3 + Q_2 + Q_{wall}, \tag{12}$$

where p is a pressure, ρ is a heat carrier density, A is a cross-section of the tube, $\vec{F}$ is the sum of all forces, C_p is the heat carrier heat capacity, T_2 is a temperature, $\vec{v}$ is a velocity vector, k_2 is the heat carrier thermal

conductivity, f_D is the Darcy coefficient, $d = \frac{4A}{Z}$ is an effective diameter, Z is the perimeter of tube wall, Q_2 is the heat which is released due to viscous friction [W/m] on the unit length of heat exchanger, Q_{wall} is the heat flux coming from the heat carrier to the tube walls [W/m]

$$Q_{wall} = h \cdot Z \cdot \left(T_1 - T_2\right), \tag{13}$$

where h is the heat exchange coefficient which is found from equation

$$h = \frac{Nu \cdot k_2}{d}. \tag{14}$$

Here Nu is the Nusselt number found from equation:

$$Nu = \frac{\left(\frac{f_d}{8}\right)\left(Re - 1000\right)Pr}{1 + 12.7\left(\frac{f_d}{8}\right)^{\frac{1}{2}}\left(Pr^{\frac{2}{3}} - 1\right)}, \tag{15}$$

where $Pr = \frac{C_p\,\mu}{k_2}$ is the Prandtl number, μ is the dynamic viscosity, $Re = \frac{\rho v d}{\mu}$ is the Reynolds number, $3000 < Re < 6 \cdot 10^6$, $0.5 < Pr < 2000$.

The Darcy coefficient f_D is found with the use of the Churchill equation for the entire spectrum of the Reynolds number and all the values of e / d (e is roughness of wall surface)

$$f_D = 8\left[\frac{8}{Re}^{12} + \left(A + B\right)^{-1.5}\right]^{1/12}, \tag{16}$$

where $A = \left[-2.457 \cdot \ln\left(\left(\frac{7}{Re}\right)^{0.9} + 0.27\left(e / d\right)\right)\right]^{16}$, $B = \left(\frac{37530}{Re}\right)^{16}$.

Solving Eqs.(7) – (12), we obtain the distributions of temperatures, electric potential (for thermoelements), velocities and pressure (for heat carrier).

The above differential equations with the respective boundary conditions were solved using Comsol Multiphysics package of applied programs.

Computer simulation results

Below are given the results of optimization of the arrangement of thermoelectric modules and heat exchangers for real thermal and temperature operating conditions of heat pump for water purification device of space application. The results of computer investigations of heat exchanger design, as well as electric power supply to thermoelectric modules are very important and will be presented in detail in the next work.

The initial data:

electric power supply to thermoelectric modules – 300 W;

the number of thermoelectric modules – 80 pcs;

heat carrier temperature at inlet to hot heat transfer loop – 36 ºC;

heat carrier temperature at inlet to cold heat transfer loop – 31.5 ºC;

hydraulic resistance of each heat-transfer loop – 0.07 atm;
heat carrier flow rate in each loop – 22 ml/s.

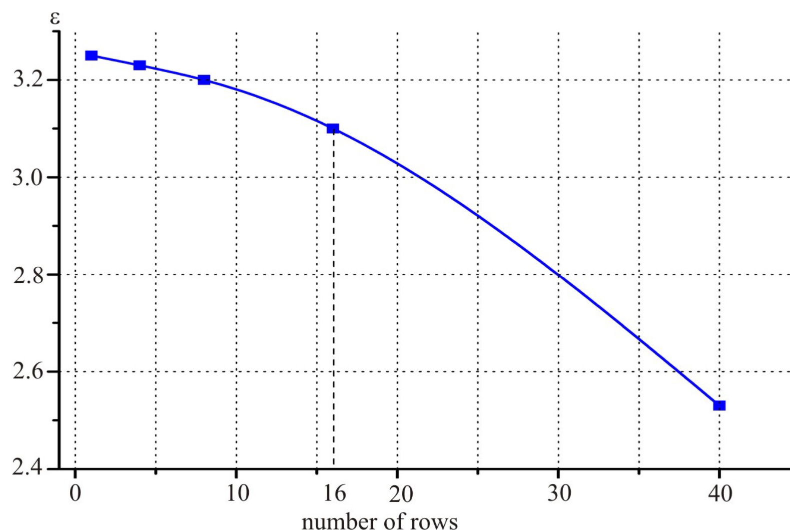

Fig. 4. Dependence of the heating coefficient of thermoelectric heat pump on the number of rows.

In this fashion, the values of the integral heating coefficient and device weight reduction (percentagewise) were calculated for different design variants of thermoelectric heat pump:

1) 1 row of 80 thermoelectric modules and 160 heat exchangers (Fig.1 *a*);
2) 4 rows of 40 thermoelectric modules and 120 heat exchangers (Fig.1 *b*);
3) 8 rows of 10 thermoelectric modules and 90 heat exchangers (Fig.1 *b*);
4) 16 rows of 5 thermoelectric modules and 85 heat exchangers (Fig.1 *b*);
5) 40 rows of 2 thermoelectric modules and 82 heat exchangers (Fig.1 *b*).

Fig. 2 represents a dependence of the heating coefficient of thermoelectric heat pump ε on the number of rows. As was to be expected, the idealized model version (Fig. 1) has the highest efficiency.

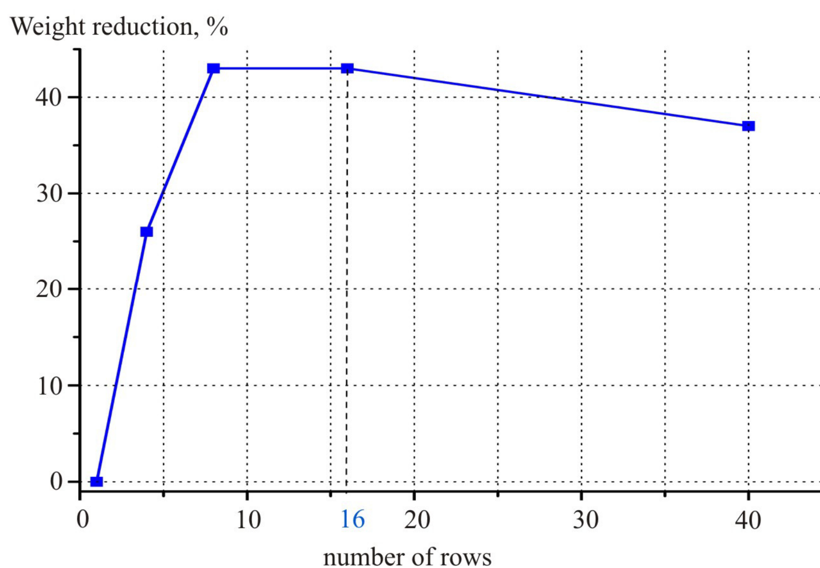

Fig. 5.Dependence of percentage weight reduction of thermoelectric heat pump on the number of rows.

For the selection of the most rational design of thermoelectric heat pump, of great importance are mass-dimensional parameters. Analysis of percentage weight reduction of thermoelectric heat

pump depending on the number of rows in it (Fig. 3) suggests the presence of an optimum, since decreasing the number of heat exchangers is attended with increasing the number of connecting elements, which makes the design heavy. Therefore, an optimum has been found which is in the area of 16 rows including 5 thermoelectric modules with 85 heat exchangers.

Comparison of computer simulation results to previous investigations [5] testifies that the efficiency (heating coefficient) of thermoelectric heat pump with the proposed arrangement of thermoelectric modules and heat exchangers is improved by 15 – 20 %.

Conclusions

1. The efficiency of thermoelectric heat pump as a function of its design parameters was calculated.
2. It was established that dependence of percentage weight reduction of thermoelectric heat pump on the number of rows has an optimum in the area of 16 rows.
3. Comparison of the obtained results to previous investigations [5] testifies that the efficiency of thermoelectric heat pump with the proposed arrangement of thermoelectric modules and heat exchangers is improved by 15 – 20 %.

References

1. Yu.Yu.Rozver, Thermoelectric Air-Conditioner for Vehicles, *J.Thermoelectricity* 2, 52 – 56 (2003).
2. L.I.Anatychuk, L.M.Vikhor, and Yu.Yu.Rozver, Investigation on Performance of Thermoelectric Cooler of Liquid or Gas Flows, *J.Thermoelectricity* 1, 73 – 80 (2004).
3. L.I.Anatychuk, N.Suzuki, and Yu.Yu.Rozver, Indoor Thermoelectric Air-Conditioner, *J.Thermoelectricity* 3, 53 – 56 (2005).
4. V.G.Rifert, V.I.Usenko, P.A.Barabash at al., Development and Test of Water Regeneration System from Liquid Biowaste on Board of Manned Spacecrafts with the Use of Thermoelectric Heat Pump *J.Thermoelectricity* 2, 63 – 74 (2011).
5. L.I.Anatychuk, P.A.Barabash, V.G.Rifert, Yu.Yu.Rozver, V.I.Usenko, and R.G.Cherkez, Thermoelectric Heat Pump as a Means of Improving Efficiency of Water Purification Systems for Biological Needs on Space Missions, *J.Thermoelectricity* 6, 78 – 83 (2013).
6. L.I.Anatychuk, Rational Areas of Thermoelectric Research and Applications, *J.Thermoelectricity* 1, 3 – 14 (2001).
7. L.I. Anatychuk, Current Status and Some Prospects of Thermoelectricity, *J.Thermoelectricity* 2, 7 – 20 (2007).
8. Michael V. Lurie, *Modeling of Oil Product and Gas Pipeline Transportation* (WILEY-VCH Verlag Gmbh & Co. KGaA, Weinheim, 2008), 214 p.

Submitted 20.08.2015

C.A. Gould[1], N.Y.A. Shammas[1], K. Simpson[2]

[1]Staffordshire University, College Road, Stoke-on-Trent, Staffordshire,
ST4 2DE, United Kingdom;
[2]European Thermodynamics UK Ltd, 8 Priory Business Park,
Kibworth, Leicester, LE8 0RX. United Kingdom

THE MODELLING AND SIMULATION OF Bi_2Te_3 THERMOELECTRIC GENERATORS IN SYNOPSYS TCAD

This paper demonstrates the modelling and simulation of thermoelectric generators using Synopsys Technology Computer Aided Design (TCAD) semiconductor design and simulation software. A single Bi_2Te_3 thermoelectric couple, and a seven couple Bi_2Te_3 thermoelectric module, have been modelled in Synopsys TCAD and simulated for thermoelectric power generation. The simulation results correctly demonstrate that when a thermoelectric couple or module is subjected to a temperature gradient, electrical power is generated at the load, with higher power levels output as the temperature gradient increases, or as the number of thermoelectric couples contained within the device increases. The simulation results obtained in TCAD, which uses in-built semiconductor physics equations, have been compared to results obtained through numerical calculation using a different set of thermoelectric equations, and the two results are in close agreement. The Synopsys TCAD models can be developed further to investigate novel device structures, and will enable new thermoelectric materials to be investigated within the framework of the simulation environment in an attempt to improve the performance, efficiency, and cost of thermoelectric devices.
Key words: TCAD, modelling and simulation, thermoelectric power generation.

Introduction

The use of computer based modelling and simulation techniques in the design of commercial thermoelectric modules is limited, with numerical calculation and bulk semiconductor manufacturing techniques common practice. This is partly due to the large geometry size of the modules, and the use of bulk semiconductor material such as Bismuth Telluride in the construction of the thermoelectric pellets. However, as the industry develops the next generation of micro-thermoelectric devices based on thin-film and nanotechnology, the use of semiconductor design and simulation tools is likely to increase. Published research in the area of thermoelectric modelling and simulation has demonstrated the use of SPICE, ANSYS, and COMSOL, but little evidence can be found for the use of Synopsys TCAD for the modelling and simulation of thermoelectric devices. TCAD is extensively used to model and simulate semiconductor devices in the electronic semiconductor industry, and has the ability to model and simulate the semiconductor manufacturing process, i.e. lithography, deposition, and diffusion, along with 2D and 3D semiconductor device design and electrical and thermal device behaviour. TCAD is very well positioned to be developed as a tool for thermoelectric device modelling and simulation as the next generation of devices, materials, and manufacturing processes converge closer to those seen in the wider electronic semiconductor industry. This paper begins with a brief introduction to Synopsys TCAD, followed by the TCAD modelling and simulation of an *n*-type and *p*-type Bi_2Te_3 pellet, and a single Bi_2Te_3 thermoelectric couple. Simulation results are then presented for the electrical power generated by the thermoelectric couple under different temperature gradients, along with a comparison between the results obtained in the TCAD simulation, and the results obtained by applying a different set of thermoelectric equations. The paper then moves to the

development of a single Bi_2Te_3 thermoelectric couple with ceramic outer plates, and a seven couple Bi_2Te_3 thermoelectric module. An overall discussion of the work is then presented and appropriate conclusions made.

Computer based modelling and simulation techniques used in the field of thermoelectricity

The aim of this work is to demonstrate that Synopsys TCAD can be used to model and simulate the behaviour of thermoelectric devices when they are configured to operate as a thermoelectric generator. Published work in this area has focused on the use of other simulation packages, notably SPICE, ANSYS, and COMSOL, and this work will identify the advantages, and demonstrate that, Synopsys TCAD can also be used to model and simulate thermoelectric devices. The use of SPICE software has generally focused on the development of a SPICE equivalent circuit model to describe the behaviour of a single thermoelectric couple, or a more generic thermoelectric module or system [1 – 6]. It can be argued that although SPICE equivalent circuit models can be used to describe the behaviour of a thermoelectric couple, module, or system, it is difficult to use this technique as a design aid to develop the next generation of thermoelectric modules that use new materials or device structures, where information on the electrical and thermal performance of the device or system is limited or not readily available. Similarly, ANSYS has been used to take advantage of the relative power of finite-element analysis techniques, with examples amongst others from [7 – 11] describing published work into the modelling and simulation of the power generation and cooling properties of a thermoelectric couple and module in ANSYS. Work in this area has demonstrated that ANSYS is a capable tool for modelling thermoelectric behaviour, with the ability to model device structures in three dimensions, although it is necessary to have a good understanding of the thermoelectric, electrical, and thermal properties of the materials within the device simulation at each temperature of interest before any simulation can be fully executed. The third simulation tool that has recently started to be used by the thermoelectric community is COMSOL, with published work by [12 – 13] demonstrating the modelling and simulation technique for thermoelectric power generation and cooling. The simulation package is similar to ANSYS, in that it uses finite-element analysis, but also allows for direct equation entry when building a simulation model. It is anticipated that successfully modelling a thermoelectric couple and module in Synopsys TCAD will allow for a more detailed electrical and thermal analysis to be made than can currently be achieved by using SPICE, ANSYS or COMSOL.

Synopsys TCAD modelling and simulation

TCAD comprises of a suite of programs that can be executed independently or together in the form of a Workbench Project, in order to simulate the electrical characteristics and thermal properties of a semiconductor device. It is a finite-element and SPICE compatible computer simulation program, and solves the fundamental, physical partial differential equations, such as diffusion and transport equations, and supports a broad range of semiconductor applications. A simulation project is first created in Sentaurus Workbench in order to control the flow of the simulation, define experiment parameters and variables. Specific TCAD tools are then added to the Workbench project in order to create a working simulation. Sentaurus Structure Editor is executed first, and a two or three dimensional structure is created within this environment, and then meshed using Sentaurus Mesh. The meshed device is then passed to Sentaurus Device, where the electrical and thermal simulation of the device is executed. The behaviour of the device is simulated numerically by calculating terminal currents, voltage and charges, using a set of physical device equations that describe the carrier distribution and conduction mechanisms, with specific physics models executed according to the models specified within the Sentaurus Device command structure. Sentaurus

device will calculate, amongst others, the; electrostatic potential by solving the semiconductor Poisson equation; continuity equations relating to the thermodynamic carrier transport model; the lattice, electron, and hole temperatures; the electron and hole absolute thermoelectric powers; and the Peltier effect at metal-semiconductor interfaces. The output of Sentaurus Device can then be represented graphically using Sentaurus Visual and Inspect [14]. According to Sentaurus [15], TCAD calculates the electrostatic potential as:

$$\nabla \cdot (\varepsilon \nabla \phi + \vec{p}) = -q(p - n + N_D - N_A) - \rho_{trap}, \tag{1}$$

where ε is the electrical permittivity; $\vec{p}$ is the ferroelectric polarization; q is the elementary electronic charge; n and p are the electron and hole densities; N_D is the concentration of ionized donors; N_A is the concentration of ionized acceptors; and ρ_{trap} is the charge density contributed by traps and fixed charges [15]. The thermodynamic model for current densities accounts for self-heating and includes the temperature gradient as the driving term as:

$$\vec{J}_n = -nq\mu_n(\nabla\Phi_n + P_n\nabla T) \tag{2}$$

$$\vec{J}_p = -nq\mu_p(\nabla\Phi_p + P_p\nabla T). \tag{3}$$

where P_n and P_p are the absolute thermoelectric powers, n is the electron density, p is the hole density, q is the elementary electronic charge, μ_n and μ_p are the electron and hole mobility, Φ_n and Φ_p are the electron quasi-Fermi potential and hole quasi-Fermi potential, and T is the lattice temperature [16]. Sentaurus Device can compute up to three different temperatures; lattice temperature; electron temperature; and hole temperature. The lattice temperature describes the self-heating of devices, and within the TCAD environment, the lattice temperature can be computed non-uniformly using the thermodynamic model [17]. According to Sentaurus [18], the electron and hole absolute thermoelectric powers P_n and P_p for nondegenerate semiconductors can be written as:

$$P_n = -k_n \frac{k}{q}\left[\left(\frac{5}{2} - S_n\right) + \ln\left(\frac{N_C}{n}\right)\right], \tag{4}$$

$$P_p = -k_p \frac{k}{q}\left[\left(\frac{5}{2} - S_p\right) + \ln\left(\frac{N_V}{p}\right)\right], \tag{5}$$

where the parameters κ_n, κ_p, S_n and S_p can be adjusted in the parameter file. Although the Seebeck effect has the most influence for thermoelectric power generation, it can also be noted that the Peltier effect at metal-semiconductor interfaces is accounted for in TCAD using:

$$Q_n = J_n(\alpha_n \Delta E_n + (1-\alpha_n)\Delta\varepsilon_n, \tag{6}$$

$$Q_p = J_p(\alpha_p \Delta E_p + (1-\alpha_p)\Delta\varepsilon_p, \tag{7}$$

where Q is the heat density at the interface (when $Q > 0$ there is heating; when $Q < 0$ there is cooling), and J_n and J_p are the electron and hole densities normal to the interface, ΔE_n and ΔE_p are the energy differences for electrons and holes across the interface, and α_n, α_p, $\Delta\varepsilon_n$, and $\Delta\varepsilon_p$ are fitting parameters with $0 \le \alpha_n, \alpha_p \le 1$ [19].

Background thermoelectric theory

If a single thermoelectric couple, as shown in Fig. 1(*a*), is subjected to a temperature difference between the two two sides of the thermoelectric couple, thermal energy will move through the *p*-type and *n*-type pellets, and as these pellets are electrically conductive, charge carries are transported by this heat. This movement of heat and charge carriers creates an electrical voltage called the Seebeck voltage. If a resistive load is connected across the thermoelectric couple's output terminals, shown in Fig. 1(*b*), current will flow in the load and an electrical voltage will be generated at the load [20]. A single thermoelectric

couple is generally of limited practical use, as the rate of useful power generated due to the Seebeck effect is very small. Practical thermoelectric modules are constructed with several of these thermoelectric couples connected electrically in series and thermally in parallel, with modules typically containing a minimum of three thermoelectric couples, rising to one hundred and twenty seven couples for larger devices [21].

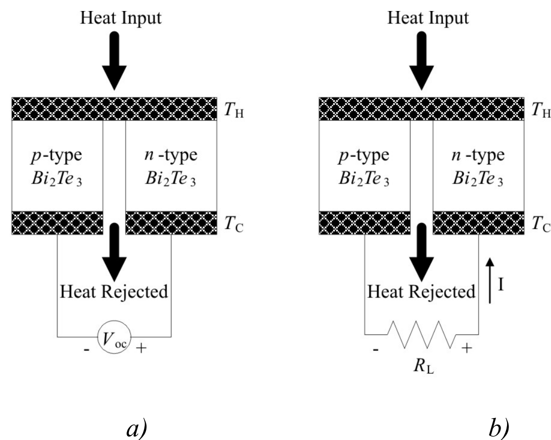

Fig. 1. A single thermoelectric couple configured as a thermoelectric generator with a volt meter measuring the open-circuit voltage V_{oc} (a) and in (b) with a load resistor R_L connected across the couple's output terminals [22].

Synopsys TCAD modelling and simulation of *p*-type and *n*-type Bi_2Te_3 thermoelectric pellets

Single pellets of both *p*-type and *n*-type Bismuth Telluride (Bi_2Te_3) have been modelled in Sentaurus Structure Editor with the material properties given in Table 1, and are typical values used in commercial thermoelectric modules kindly provided by [23]. A single *p*-type Bi_2Te_3 pellet, shown in Fig. 2 and Fig. 3, has been modelled between two copper connectors, *Copper* 1 and *Copper* 2. These copper connectors act as electrodes for the negative and positive terminals of a DC input voltage source V_{in}. The pellet was simulated at an average temperature of 300.5 K, and as a TCAD mixed-mode simulation. A TCAD compact model voltage source V_{in} of 1 mV was connected between the negative terminal *Copper* 1 and the positive terminal *Copper* 2 of the device, and the resulting circuit current *I* has been measured in TCAD. The pellets electrical resistivity ρ_p, Seebeck coefficient α_p, and thermal conductivity λ_p has also been measured in TCAD, and the pellets resistance R_P calculated. A simulated input voltage V_{in} of 1 mV has then been applied to the input terminals of each pellet resulting in a circuit current *I* of 104.51 mA. The pellets properties with an average pellet temperature of; 300.5 K; 312.5 K; 325 K; 337.5 K; and 350 K; are summarised in Table 2.

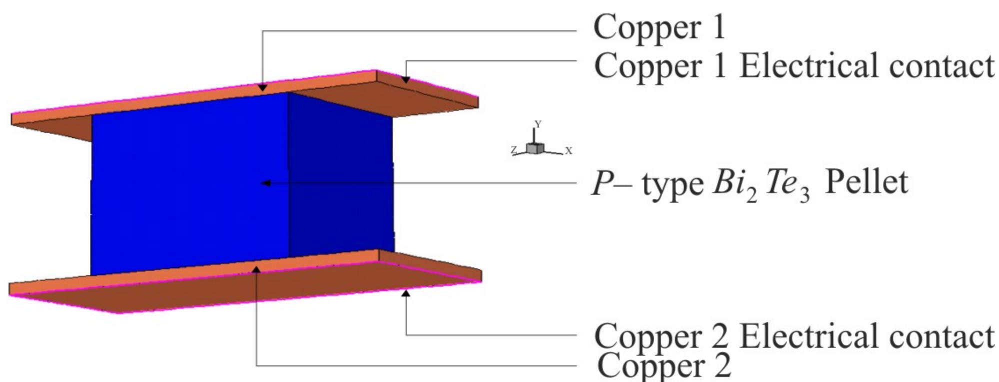

Fig. 2. p-type Bi_2Te_3 thermoelectric pellet modelled in Sentaurus Structure Editor.

Table 1

Typical material properties and dimensions of a p-type and n-type Bi_2Te_3 thermoelectric pellet at an average temperature of 300.5 K obtained from [23]

Parameter	Value	Unit	Description
α_p	215×10^{-6}	V/K	Seebeck coefficient *p*-type
α_n	-212×10^{6}	V/K	Seebeck coefficient *n*-type
ρ_p	0.00104	Ω cm	Electrical resistivity *p*-type
ρ_n	0.00104	Ω cm	Electrical resistivity *n*-type
λ_p	0.0137	W/cm K	Thermal conductivity *p*-type
λ_n	0.0146	W/cm·K	Thermal conductivity *n*-type
l_p or l_n	0.14	cm	Pellet length (*p*-type or *n*-type)
w_p or w_n	0.14	cm	Pellet width (*p*-type or *n*-type)
d_p or d_n	0.11	cm	Pellet depth (*p*-type or *n*-type)
A_p or A_n	0.0154	cm^2	Cross-sectional area(*p*-type or *n*-type)

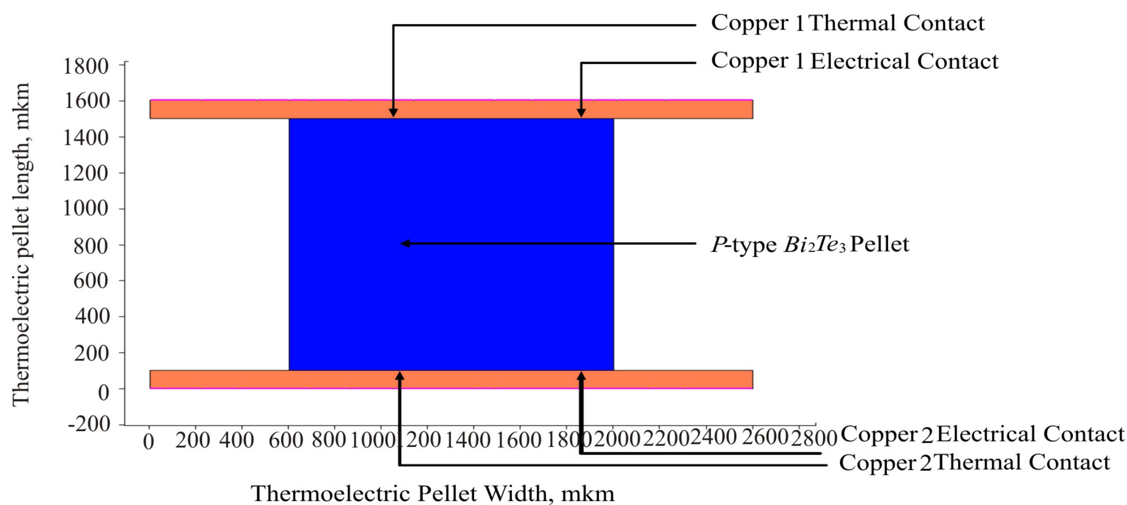

a)

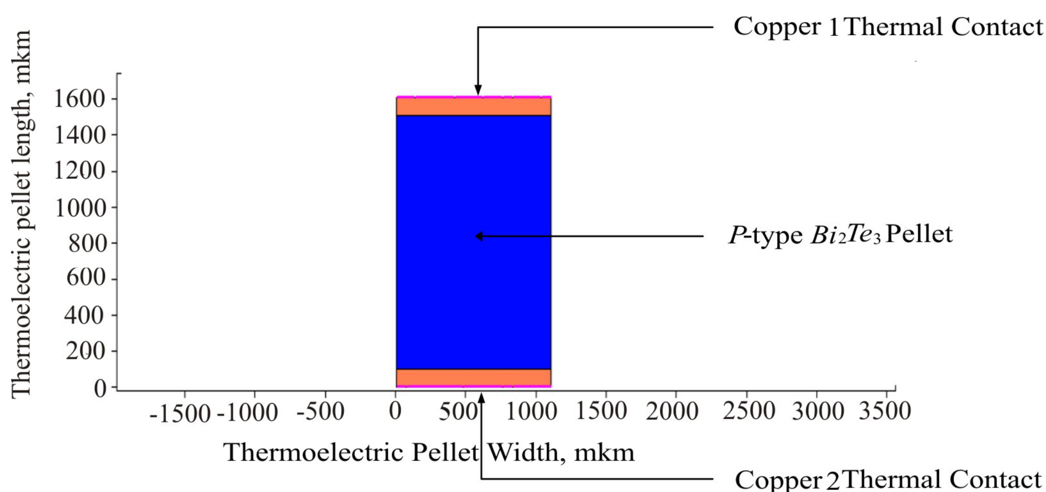

b)

Fig. 3. A cut-through in the Z-direction of the p-type Bi_2Te_3 pellet model highlighting the electrical and thermal connections (a) and a cut-through in the X-direction of the p-type Bi_2Te_3 pellet model highlighting the pellet depth in the Z-direction of 1100 micron metres (b).

Table 2

Sentaurus Device (TCAD) Bi_2Te_3 thermoelectric pellet model parameters at different average temperatures T_{avg} obtained from simulation

T_{avg} K	α_p μV	α_n μV	R_p mΩ	R_n mΩ	K_p mW	K_n mW
300.5	215	–212	9.57	9.31	1.51	1.61
312.5	222	–216	10.99	10.07	1.51	1.61
325.0	229	–220	11.01	10.90	1.51	1.61
337.5	236	–224	11.77	11.78	1.51	1.61
350.0	243	–228	12.58	12.71	1.51	1.61

Synopsys TCAD modelling and simulation of a single Bi_2Te_3 thermoelectric couple

A single Bi_2Te_3 thermoelectric couple has then been modelled in Sentaurus Structure Editor and is shown in Fig. 4(*a*). An electrode contact was made on the face of *Copper* 2 and *Copper* 3 to simulate the negative and positive electrical connections to the couple, and a thermal contact was made on the face of *Copper* 1, *Copper* 2, and *Copper* 3 in order to allow the temperature of each contact to be specified or calculated. The dimensions of the thermoelectric couple, along with the electrical and thermal contacts, are shown in Fig. 4(*b*), with the depth of the couple in the *Z*-direction equal to 1100 micron metres (1.1 mm). The simulation model is considered to be an 'ideal' representation of a thermoelectric couple, and assumes that there is no thermal resistance between the thermoelectric couple hot side T_H and the heat source, or the thermoelectric couple cold side T_C and the heat sink. Therefore, all of the heat flow between the source and sink takes place within the thermoelectric couple, and that the thermal radiation and losses by conduction and convection through the surrounding medium is considered to be negligible. The thermoelectric couple was simulated as a TCAD mixed-mode simulation, and a TCAD compact model of a load resistor R_L was connected between the output terminals *Copper* 2 and *Copper* 3 of the device in order to calculate the electrical power generated at the load. The temperature of the thermal contact on *Copper* 1 was increased from steady state conditions of 300 K to 301 K, whilst the temperature of the other two thermal contacts, *Copper* 2 and *Copper* 3, were kept at 300 K. This creates a 1 K temperature difference between both sides of the couple. The load resistance R_L was increased from 0.001 Ωs through to 0.030 Ωs, in 0.001 Ω steps, in order to establish where maximum power transfer occurs. The voltage V_L and current I_L at the load was recorded using the simulation program, and the electrical power generated at the load calculated using the equation $P_L = V_L \times I_L$. The electrical power generated at the load is shown in Fig. 5 and reaches a peak value of 2.61 μW with a load resistance of 0.017 Ωs, where maximum power transfer is observed.

The couple was then tested with the temperature of the thermal contact on *Copper* 1 increased from 301 K to; 325 K; 350 K; 375 K; and 400 K. The temperature of the other two thermal contacts, *Copper* 2 and *Copper* 3, were kept at 300 K. This creates a temperature difference between both sides of the couple of; 25 K; 50 K; 75 K; and 100 K respectively. The power generated at the load, shown in Fig. 6, can be seen to increase as the temperature gradient increases, and peaks at 22.67 mW with a load resistance of 0.025 Ωs and a temperature of 400 K applied to the thermal contact *Copper* 1 located at the top of the device.

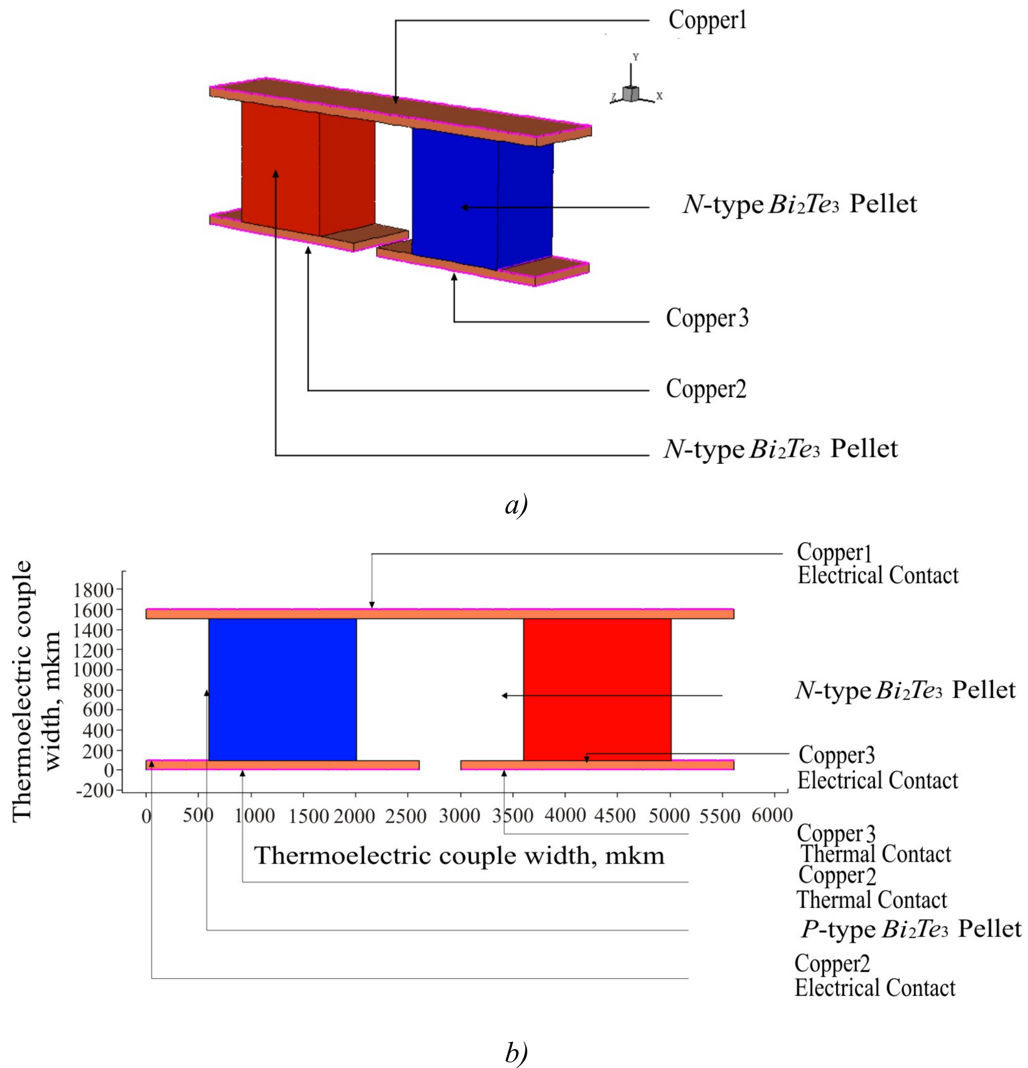

b)

Fig. 4. A Bi_2Te_3 thermoelectric couple modelled in Sentaurus Structure Editor (a) and a cut-through in the Z-direction of the Bi_2Te_3 thermoelectric couple model highlighting the electrical and thermal connections (b).

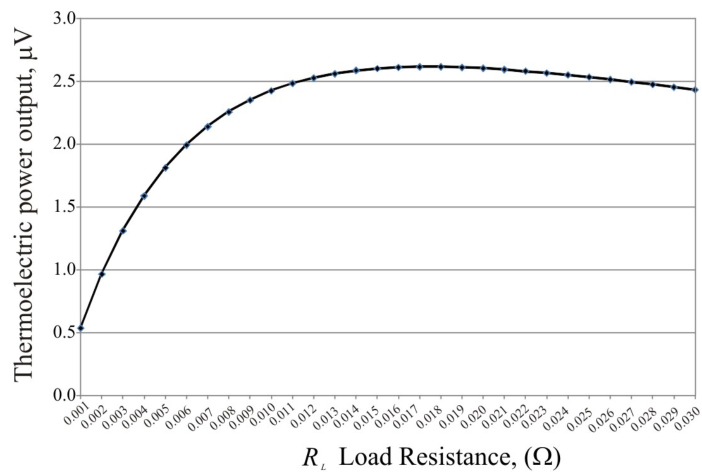

Fig. 5. The thermoelectric output power generated at the load when the Bi_2Te_3 thermoelectric couple is subjected to a 1 K temperature gradient (Simulation result).

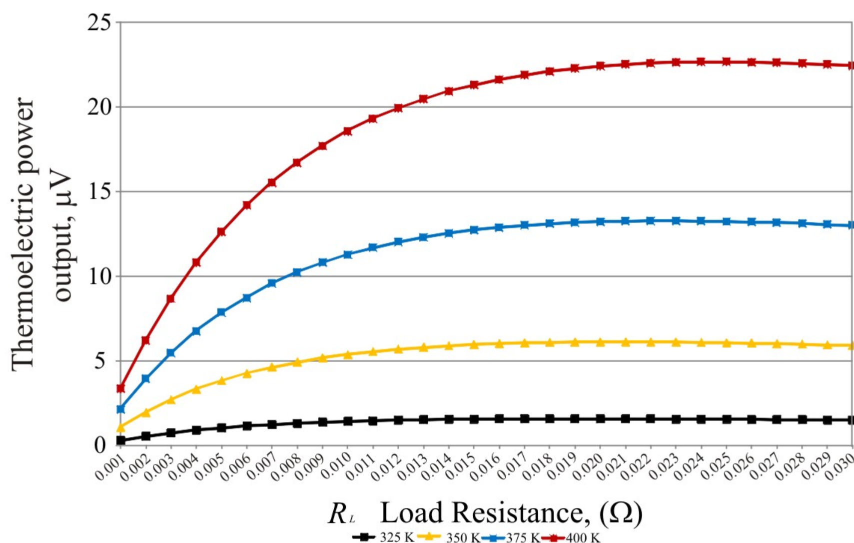

Fig. 6. The thermoelectric power generated at the load when the thermal contact Copper 1 located at the top of the device is set to 325, 350, 375, and 400 K, creating a temperature gradient of 25, 50, 75 and 100 K respectively across the device (Simulation result).

Numerical analysis of a single Bi_2Te_3 thermoelectric couple

In order to validate the TCAD simulation results, an analysis can be made to compare the simulation results obtained in TCAD, which uses in-built semiconductor physics equations that calculate, amongst others, the; electrostatic potential; thermodynamic carrier transport; the lattice, electron, and hole temperatures; and the electron and hole absolute thermoelectric powers; with the results obtained by numerical calculation using a different set of equations published in thermoelectric literature that describes the behaviour of a single thermoelectric couple when it is subjected to a temperature gradient. According to [24], if we consider that no other heat arrives at the cold side T_c other than through the two thermoelectric legs, the thermoelectric couple open-circuit voltage V_{oc} can be found by:

$$V_{oc} = \left(\alpha_p - \alpha_n\right)\left(T_h - T_c\right) \quad , \tag{8}$$

where α_p and α_n is the Seebeck coefficient of the p-type and n-type pellets of the thermoelectric couple respectively, T_h is the surface temperature of the hot side of the thermoelectric couple, and T_c is the surface temperature of the cold side of the thermoelectric couple, measured in K. The electrical resistivity ρ of each pellet can be found and/or measured, and the resistance R_p of the p-type pellet can then be calculated using:

$$R_p = \frac{L_p \rho_p}{A_p} \quad , \tag{9}$$

where ρ_p is the electrical resistivity of the pellet in Ωs/cm, L_p is the length of the pellet in cm, and A_p is the cross-sectional area of the pellet in cm^2 found by:

$$A_p = \text{width} \times \text{depth} . \tag{10}$$

Similarly, the resistance of the *n*-type pellet R_n can be found. The thermoelectric couple resistance R_c, ignoring the resistance of the copper interconnects, is the addition of the resistance of the two thermoelectric pellets:

$$R_c = R_p + R_n . \tag{11}$$

The resistance of the copper interconnects is typically in the mΩ region, and compared with the resistance of the Bi_2Te_3 thermoelectric pellets, which tends to be in the milli ohm region, is significantly smaller in value and hence can be considered as negligible. The thermal conductivity λ of each pellet can be found and/or measured, and the thermal conductivity K_p of the *p*-type thermoelement calculated by:

$$K_p = \frac{\lambda_p A_p}{L_p} , \tag{12}$$

where λ_p is the thermal conductivity of the pellet in W/cm·K, L_p is the length of the pellet in cm, and A_p is the cross-sectional area of the pellet in cm^2. Similarly, the thermal conductivity of the *n*-type pellet K_n can be found. The current I can be expressed as:

$$I = \frac{V}{R_T} , \tag{13}$$

where V is the closed-circuit voltage, and R_T is the total resistance of the thermoelectric couple and the load. It is possible to find R_T using:

$$R_T = R_p + R_n + R_L . \tag{14}$$

As the load resistor R_L is connected across the output terminals of the couple, the load current I_L is the same as the circuit current I, and the voltage generated at the load V_L can be found by:

$$V_L = I_L \times R_L . \tag{15}$$

the electrical power generated at the load can be found by:

$$P_L = V_L \times I_L \tag{16}$$

The efficiency η of a thermoelectric couple can be found by:

$$\eta = \frac{\text{Energy supplied to the load}}{\text{Heat energy absorbed at the hot junction}} . \tag{17}$$

The electrical power supplied to the load is P_L, and according to [24], the cooling power at the hot side of the thermoelectric couple Q_h can be found by:

$$Q_h = (\alpha_p - \alpha_n) I T_h - (T_c - T_h)(K_p + K_n) - \frac{I^2 (R_p + R_n)}{2} \tag{18}$$

Hence, the efficiency of the thermoelectric couple η can now be found by equation (17), and written as:

$$\eta = \frac{P_L}{Q_h} . \tag{19}$$

In thermoelectricity, efficiency is expressed as the dimensionless figure-of-merit Z, or more commonly, expressed as a function of the temperature over which the device is operated Z_T, which can be found by:

$$Z_T = \frac{\alpha^2 \sigma}{\lambda}, \tag{20}$$

where α is the Seebeck coefficient, σ is the electrical conductivity, and λ is the thermal conductivity of the couple at a specific operating temperature. The Bi_2Te_3 thermoelectric couple TCAD simulation results have been summarised in Table 3 for ease of comparison, and demonstrate good agreement between the expected result obtained by numerical calculation using equations (8 – 20), and the results obtained by TCAD simulation that uses a different set of in-built semiconductor equations that include, amongst others, equations (1 – 7).

Table 3

A summary of the Bi_2Te_3 thermoelectric couple TCAD simulation results

	T_H K	T_C K	ΔT K	V_{oc} mV	I_L mA	V_L mV	P_L mW	R_L Ω	Efficiency η %	Z_T
Calculated	301	300	1	0.427	11.31	0.21	0.00242	0.019	0.05	3.10×10^{-3}
TCAD	301	300	1	0.427	12.41	0.21	0.00262	0.017	0.06	3.44×10^{-3}
Calculated	325	300	25	10.95	260	5.48	1.42	0.021	1.25	2.77×10^{-3}
TCAD	325	300	25	10.96	289	5.49	1.59	0.019	1.36	2.78×10^{-3}
Calculated	350	300	50	22.45	512	11.23	5.75	0.022	2.50	2.67×10^{-3}
TCAD	350	300	50	22.49	540	11.35	6.13	0.021	2.63	2.67×10^{-3}
Calculated	375	300	75	34.50	733	17.25	12.64	0.024	3.67	2.48×10^{-3}
TCAD	375	300	75	34.50	760	17.48	13.20	0.023	3.78	2.48×10^{-3}
Calculated	400	300	100	47.10	931	23.55	21.93	0.025	4.77	2.31×10^{-3}
TCAD	400	300	100	47.04	952	23.80	22.67	0.025	4.90	2.31×10^{-3}

Synopsys TCAD simulation of a Bi_2Te_3 thermoelectric couple with ceramic outer plates

A single thermoelectric couple with ceramic outer plates of thermal conductivity 0.3 W/cm·K has been simulated, shown in Fig. 7(*a*) and Fig. 7(*b*). The top and bottom faces of the two ceramic plates have been used as the thermal contacts of the device, and are labelled *Ceramic Top* and *Ceramic Bottom* respectively. Otherwise, the construction of the device is the same as shown for a single thermoelectric couple without ceramic outer plates. If the top of the device, where the thermal contact *Ceramic Top* is located, is set to 301 K, and the thermal contact *Ceramic Bottom* is maintained at 300 K, creating a 1 K temperature gradient, the electrical power generated at the load peaks at 2.48 mW with a load resistance of 0.017 Ωs, which is slightly lower than the 2.61 mW obtained without the ceramic outer plates. The ceramic outer plates absorb heat energy changing the temperature gradient, and the temperature gradient within the thermoelectric pellet has been reduced, resulting in less electrical power generated at the load. However, the ceramic plates are necessary in practical devices in order to create electrical isolation and provide a foundation to mount the thermoelectric couple. Further simulations have been performed with a temperature difference between both sides of the couple of; 25 K; 50 K; 75 K; and 100 K respectively, with the power generated at the load shown in Fig. 8. The electrical power generated at the load peaks at 21.50 mW with a load resistance of 0.025 Ωs, and a temperature gradient of 100 K maintained across the couple.

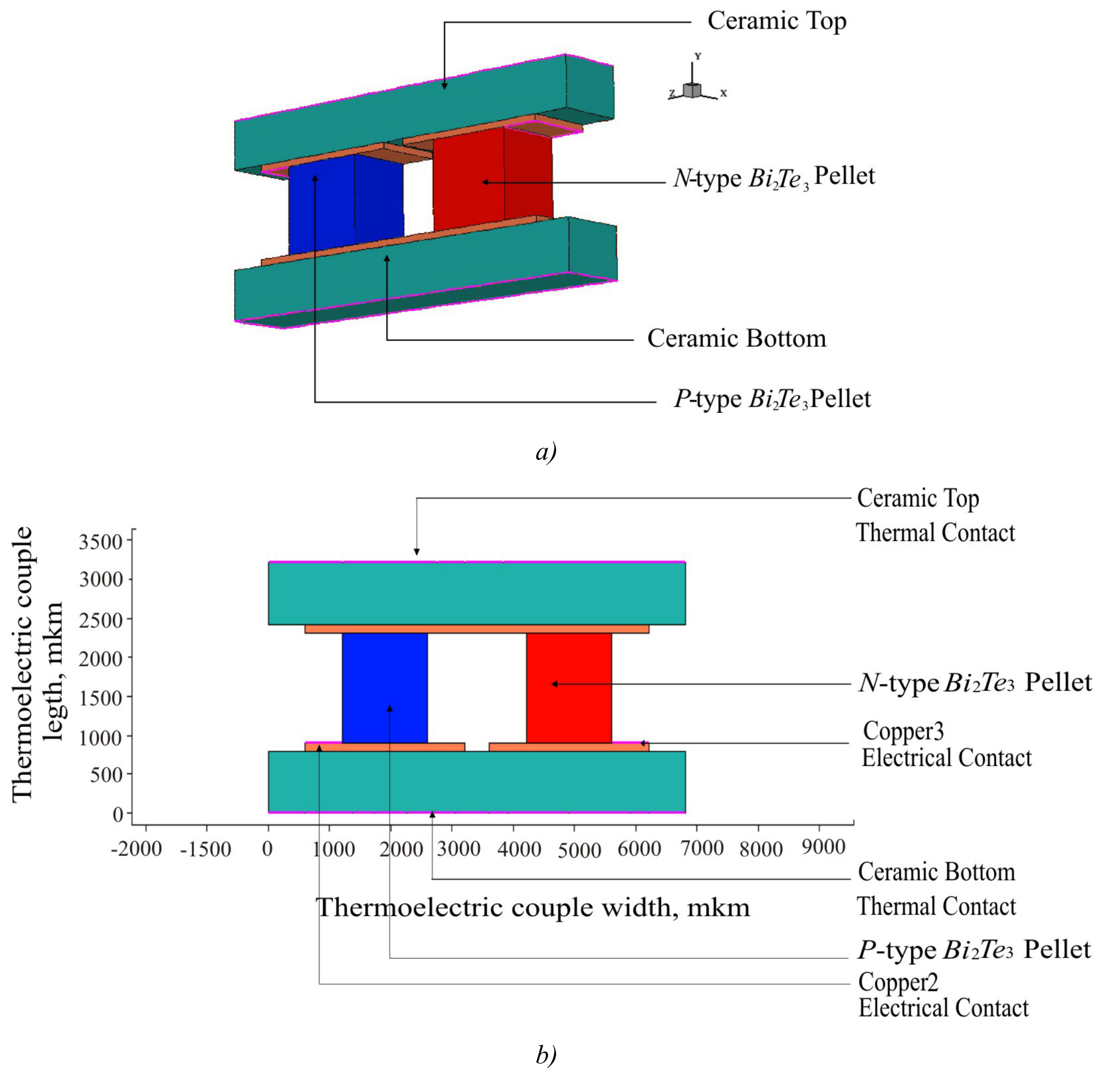

Fig. 7. A Bi_2Te_3 thermoelectric couple with ceramic outer plates modelled in Sentaurus Structure Editor (a) and a cut-through in the Z-direction, highlighting the electrical and thermal contacts (b).

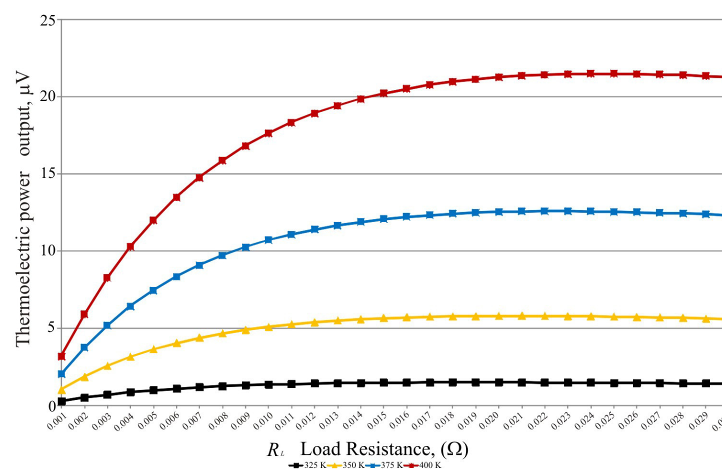

Fig. 8. The thermoelectric power generated at the load when the thermal contact Ceramic Top is set to 325 K, 350 K, 375 K, and 400 K, creating a temperature gradient of 25, 50, 75 and 100 K respectively across the device (Simulation result).

Synopsys TCAD modelling and simulation of a seven couple Bi_2Te_3 thermoelectric module

A seven couple Bi_2Te_3 thermoelectric module with ceramic outer plates has also been successfully modelled and simulated, and is shown in Fig. 9 through to Fig. 11. The top and bottom faces of the two ceramic plates have been used as the thermal contacts of the device, and are labelled *Ceramic Top* and *Ceramic Bottom* respectively. When the temperature of the thermal contact *Ceramic Top* is set to 301 K, and the temperature of the thermal contact *Ceramic Bottom* is set to 300 K, creating a one K temperature gradient, the electrical power generated at the load peaks at 19.2 μW with a load resistance of 0.11 Ωs. If we compare this with the power output for a single Bi_2Te_3 thermoelectric couple with ceramic outer plates, the electrical power generated at the load was 2.48 μW with a load resistance of 0.017 Ωs. The seven couple Bi_2Te_3 module generates over seven times as much power as the single thermoelectric couple model. This is as expected as the voltage output of each couple due to the Seebeck effect is connected electrically in series to one another, and hence the total voltage output will be the summation of each of the individual couples output. The resistance of the seven couple thermoelectric module has also increased approximately seven times, and is in-line with expectations.

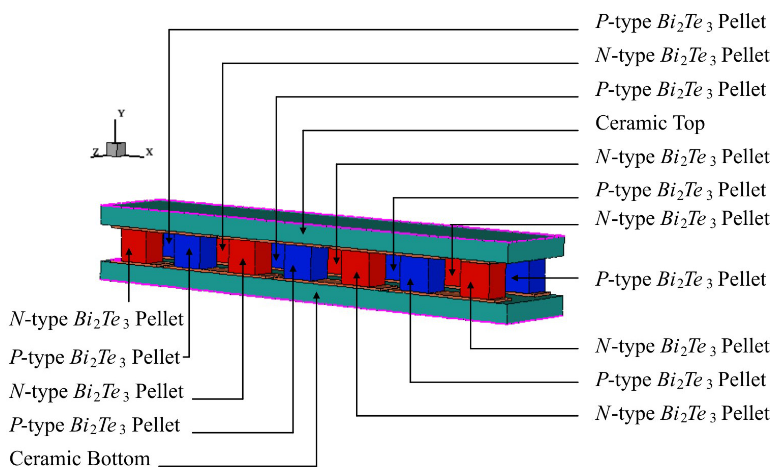

Fig. 9. A seven couple Bi_2Te_3 thermoelectric module with ceramic outer plates modelled in Sentaurus Structure Editor

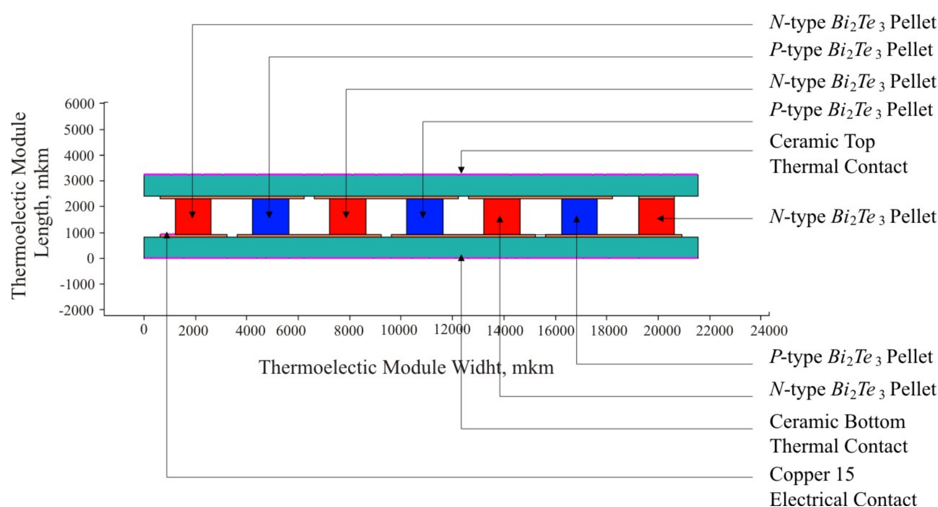

Fig. 10. A cut-through in the Z-direction of the seven couple Bi_2Te_3 thermoelectric module, highlighting the electrical and thermal contacts on one side of the module.

Fig. 11. A cut-through in the Z-direction of the seven couple Bi_2Te_3 thermoelectric module, highlighting the electrical and thermal contacts on the other side of the module.

Increasing the temperature gradient across the seven couple Bi_2Te_3 module, shown in Fig. 12, results in an increase in electrical power generated at the load as expected. The seven couple Bi_2Te_3 thermoelectric module now generates 162.17 mW at 0.16 Ωs with a temperature gradient of 100 K.

Fig. 12. - The thermoelectric power generated at the load when the thermal contact Ceramic Top is set to 325, 350, 375, and 400 K, creating a temperature gradient of 25, 50, 75 and 100 K respectively across the device (Simulation result).

Discussion

The aim of this work has been to develop Synopsys TCAD simulation models of a Bismuth Telluride (Bi_2Te_3) thermoelectric couple and a seven couple thermoelectric module. This has been successfully achieved and the TCAD simulation models demonstrate very good correlation with expected behaviour and theory. Focusing on the single Bi_2Te_3 thermoelectric couple simulation model, when the couple is subjected to a temperature gradient, a small amount of electrical power is generated at the load. This is in-line with expected behaviour, and a comparison between the results obtained in the TCAD simulation, which are based on the simulation programs use of in-built semiconductor physics models and equations that calculate, amongst others, the; electrostatic potential; thermodynamic carrier transport; the lattice, electron, and hole temperatures; and the electron and hole absolute thermoelectric powers; with the results obtained by numerical calculation using a different set of equations published in thermoelectric literature are in close agreement.

Similarly, the simulation model highlights that the amount of electrical power generated at the load is dependent on the level of temperature difference that exists between both sides of the couple. It can be demonstrated that a 100 K temperature difference across the couple generates far more electrical power at the load than can be observed with a 1 K temperature difference. Again, this is as expected, as the Seebeck effect, which has the most influence in thermoelectric power generation, is temperature dependent. The development of a single Bi_2Te_3 thermoelectric couple with ceramic outer plates highlights that the ceramic plates absorb heat energy changing the temperature gradient, resulting in the temperature gradient within the thermoelectric pellets reducing, and slightly less electrical power is generated at the load when compared to the thermoelectric couple without ceramic outer plates. However, the ceramic plates are necessary to create electrical isolation and provide a foundation to mount the thermoelectric couple. The TCAD seven couple Bi_2Te_3 thermoelectric module simulation results correctly demonstrate that by connecting several thermoelectric couples together electrically in series, and thermally in parallel, the module will generate approximately seven times more electrical power at the load than can be obtained from a single Bi_2Te_3 thermoelectric couple.

This is in-line with expected behaviour and, similar to the single Bi_2Te_3 thermoelectric couple model, a comparison between the results obtained in the TCAD simulation with the results obtained through numerical calculation by applying a different set of theoretical equations is in close agreement. Future work will provide further validation of the TCAD simulation results with practical test samples. A seven couple Bi_2Te_3 thermoelectric module was developed in Synopsys TCAD as this size of module is relatively straightforward for a thermoelectric manufacturer to produce, and test samples with the same dimensions and material properties used in the TCAD simulation model will be manufactured and subjected to the same test methodology. In this way, the Synopsys TCAD simulation results can be triangulated with the results obtained from testing a physical thermoelectric module and by calculated theory, with a full set of test results published.

Employing Synopsys TCAD to model and simulate thermoelectric generators has several advantages. It is an ideal platform to rapidly design, model, and simulate the behaviour of novel thermoelectric device structures and materials at a range of different temperature gradients, including the next generation of thermoelectric modules based on thin-film and nanotechnology. The simulation package is extensively used in the wider electronics semiconductor industry to model and simulate the behaviour of VLSI devices, and can support very small device geometry sizes. When a thermoelectric material has been defined in the materials database, in this case Bi_2Te_3, and a one, two, or three dimensional thermoelectric device structure is created, a series of simulations can be automatically executed at different temperatures of interest, and TCAD will calculate the key thermoelectric parameters, including the Seebeck coefficient, as the program executes each discrete temperature step. Furthermore, it is possible to model and simulate a thermoelectric couple or module as a single device, or as a mixed mode simulation, where the thermoelectric device can be connected to external components, for example, a load resistor or capacitor connected across the thermoelectric module's output terminals, or several different thermoelectric modules that have been designed in TCAD can be connected together in series or in parallel as part of a system. It is also possible to set-up a relatively complex simulation strategy that automatically modifies key variables in order to obtain a series of simulation results at different set-points. An additional capability within Synopsys TCAD is the ability to model and simulate the semiconductor manufacturing process, i.e. deposition, diffusion, and photolithography, which can be integrated with the TCAD device modelling and simulation tool sets. Future work will investigate

applying TCAD's semiconductor process simulation capability to thermoelectric devices and the results will be published.

Conclusions

A single Bi_2Te_3 thermoelectric couple, and a seven couple Bi_2Te_3 thermoelectric module, have been successfully modelled and simulated in Synopsys TCAD semiconductor design and simulation software. The simulation results obtained for thermoelectric power generation are in agreement with expected behaviour, with the model correctly demonstrating that when a temperature gradient is applied to a thermoelectric device, electrical power is generated at the load due to the Seebeck effect, with the amount of generated power dependent on the level of temperature gradient that exists across the device. It can also be observed that by connecting several thermoelectric couples together electrically in series, and thermally in parallel, a thermoelectric module will generate higher levels of electrical power at the load than can be obtained from a single thermoelectric couple. A comparison between the results obtained in the TCAD simulation, which are based on the simulation programs use of in-built semiconductor physics models and equations, and that obtained by applying a different set of thermoelectric equations, are also in close agreement and can be used to validate the simulation results. The Synopsys TCAD thermoelectric model can be developed in the future to investigate the effect of different thermoelectric device structures, and will enable new thermoelectric materials to be investigated, within the framework of the simulation environment, in an attempt to improve the performance, efficiency, and cost of thermoelectric devices.

References

1. S. Lineykin, S. Ben-Yaakov, "Analysis of Thermoelectric Coolers by a Spice-Compatible Equivalent-Circuit Model", *IEEE Power Electronic Letters*, Vol. 3, No. 2, June 2005, pp. 63 – 66
2. J. A. Chavez, J. A. Ortega, J. Salazar, A. Turo, M. J. Garcia, "SPICE model of Thermoelectric Elements Including Thermal Effects", *Proc. 17th IEEE Instrumentation and Measurement Conference*, May 2000, Vol. 2, pp. 1019 – 1023
3. P. Dziurdzia, A. Mirocha, "From Constant to Temperature Dependent Parameters Based Electrothermal Models of TEG", *Proc. 16th International Conference Mixed Design of Integrated Circuits and Systems*, June 2009, Lodz, Poland, pp. 555 – 559
4. S. Lineykin, S. Ben-Yaakov, "Spice Compatible Equivalent Circuit of the Energy Conversion Process in Thermoelectric Modules", *Proc. 23rd IEEE Convention in Electrical and Electronic Engineers in Israel*, September 2004, pp. 346 – 349
5. M. Chen, J. Gao, Z. Kang, J. Zhang, Q. Du, R. O. Suzuki, "Design Methodology of Large-scaleThermoelectric Generation: A Hierarchical Modeling Approach in SPICE", *IEEE Industry Applications Society Annual Meeting (IAS),* 2011, October 2011, pp. 1 – 7
6. S. Lineykin, S. Ben-Yaakov, "Modeling and Analysis of Thermoelectric Modules", *IEEE Transactions on Industry Applications*, Vol. 43, No. 2, March/April 2007, pp. 505 – 512
7. E. Antonova, D. Looman, "Finite Elements for Thermoelectric Device Analysis in ANSYS", *Proc. International Conference on Thermoelectrics (ICT2005)*, South Carolina, USA, 19th – 23rd June 2005, pp. 215 – 218
8. M. A. Soto, R. Venkatasubramanian, "ANSYS-based detailed Thermo-mechanical Modeling of Complex Thermoelectric Power Designs", *Proc. International Conference on Thermoelectrics (ICT2005)*, South Carolina, USA, 19th – 23rd June 2005, pp. 204 – 206
9. S. Li, C. Liu, C. Hsu, M. Hsieh, M. Dai, S. Wu, "Thermo-mechanical analysis of Thermoelectric

Modules, *Proc. 5th International Microsystems Packaging Assembly and Circuits Technology (IMPACT)*, 20th – 22nd October 2010, Taipei, Taiwan, pp. 1 – 4

10. C. LaBounty, A. Shakouri, G. Robinson, P. Abraham, J. Bowers, “Design of Integrated Thin Film Coolers” , *Proc. 18th International Conference on Thermoelectrics (ICT1999)*, Aug 29th to Sept 2nd, 1999, Baltimore USA, pp. 23 – 26
11. R. McCarty, “High Performance from Multiphysics Coupled Simulation”, *ANSYS Advantage*, 2008, Vol. 2, Issue 2, pp. 26 – 28
12. M. Jaegle, “Multiphysics Simulations of Thermoelectric Systems – Modeling of Peltier cooling and Thermoelectric Generation”, *Proc COMSOL Conference*, 2008, Hanover, pp. 1 – 7
13. S. Yushanov, L. Gritter, J. Crompton, K. Hoppenhoefer, “Multiphysics Analysis of Thermoelectric Phenomena”, *Proc COMSOL Conference*, 2011, Hanover, pp. 1 – 3
14. Synopsys, “Sentaurus Device User Guide”, *Synopsys*, Version D-2010.03, March 2010
15. Synopsys, “Electrostatic Potential”, Sentaurus Device User Guide, *Synopsys*, Version D-2010.03, March 2010, pp. 181
16. Synopsys, “Thermodynamic Model for Current Densities”, Sentaurus Device User Guide, *Synopsys*, Version D-2010.03, March 2010, pp. 189
17. Synopsys, “Introduction to Temperature Equations”, Sentaurus Device User Guide, *Synopsys*, Version D-2010.03, March 2010, pp. 181
18. Synopsys, “Thermoelectric Power (TEP)”, Sentaurus Device User Guide, *Synopsys*, Version D-2010.03, March 2010, pp. 701 – 702
19. Synopsys, “Thermodynamic Model for Lattice Temperature”, Sentaurus Device User Guide, *Synopsys*, Version D-2010.03, March 2010, pp. 197
20. S.B. Riffat, X. Ma, “Thermoelectrics: a review of present and potential applications”, *Applied Thermal Engineering*, 2003, vol. 23, pp. 913 – 915
21. C.M. Bhandari (2006), “Thermoelectric Transport Theory”, in *CRC Handbook of Thermoelectrics*, edited by D.M. Rowe, CRC Taylor and Francis Group, 1995, ISBN 978 – 0 – 8493 – 2264 – 8, pp. 27 – 42
22. D.M. Rowe (2006), “General Principles and Basic Considerations”, in *Thermoelectrics Handbook: Macro to Nano*, edited by D.M. Rowe, Boca Raton: CRC Press, Taylor & Francis Group, ISBN 978 – 0 – 8493 – 2264 – 8, pp. 1 – 14
23. K. Simpson, “Thermoelectric Module Materials Data”, *European Thermodynamics Ltd*, (Unpublished), 2008
24. H.J. Goldsmid (2010), *Introduction to Thermoelectricity (Springer Series in Materials Science)*, Berlin: Springer-Verlag, ISBN 978 – 3 – 642 – 00715 – 6

Submitted 22.08.2015

V.Ya.Mykhailovsky, M.V.Maksimuk

Institute of Thermoelectricity of the NAS and MES of Ukraine, 1, Nauky Str., Chernivtsi, 58029, Ukraine

V.Ya. Mykhailovsky

M.V. Maksimuk

RATIONAL POWERS OF THERMOGENERATORS FOR STARTING PRE-HEATERS OF VEHICLES

The main technical characteristics of starting pre-heaters for different kinds of vehicles are given. The electric parameters of thermogenerators necessary for the autonomous operation of such pre-heaters and the opportunities of power supply to other automobile equipment, including battery recharge, are defined.

Key words: starting pre-heater, thermoelectric generator.

Introduction

At the present time, the problem of startup of internal combustion engines of vehicles at low ambient temperatures is solved by using starting pre-heaters commercially produced by a number of companies, namely Eberspächer, Webasto, Truma (Germany), Ateso (Czech Republic), Teplostar (Russia), Mikuni (Japan). Such pre-heaters run on different kinds of fuel and are used in the cars, trucks, buses, yachts and boats [1 – 6].

Depending on application, there are air pre-heaters for heating of cabins and compartments of vehicles and liquid pre-heaters, which, in addition to heating, assure preliminary warm-up of internal combustion engine. Liquid pre-heaters are more efficient, as long as start heating of internal combustion engine assures its reliable startup and essential reduction of fuel consumption during the first kilometers of automobile trip. It is also important to reduce harmful emission to environment at automobile engine startup, since today the European Union standards, apart from total norm of emission for heated engine already regulate the amount of emission at its startup. It is established that the use of start heating can increase engine service life by 50-60 thousand km per year and reduce emission of toxic substances by a factor of 5, saving 90 – 150 l of fuel during one winter season. Moreover, comfortable conditions assured by start heating of automobile exclude completely the possibility of accidents because of the influence of cold on the driver [7].

Nevertheless, despite wide opportunities, staring pre-heaters have not found wide use yet, in particular, on the cars and microbuses. Even in the Nordic countries autonomous starting pre-heaters are installed only on one of thousand automobiles. One of the main reasons for this is a need in electric energy for power supply to heater components: fuel pump, fan for air delivery to combustion chamber, circulation pump for pumping of liquid heat carrier. Preliminary studies have shown that in operation of liquid heater with thermal power 4 kW and electric power consumption 60 W, a battery with capacity 60 A·hour within 4.5 hours will lose 50% of capacity. This leads to battery discharge and creates essential difficulties at engine startup [8].

The problem defined above can be solved through use of a thermoelectric generator which operates from the heater and supplies power to its components. Moreover, the excess electric energy of thermal generator can be used for battery recharge and power supply to other automobile equipment (standard

heating fan, warning systems, etc) [8 – 10]. Under these conditions, a relevant task is to create general-purpose thermoelectric converters that that would not only assure independent operation of each heater type, but would also find wide application as additional source of electric energy in different kinds of vehicles.

So, the purpose of this paper is to determine the electric characteristics of thermoelectric generators (TEG) for start heating of vehicular engines at low ambient temperatures.

TEG for liquid starting pre-heaters

In Table 1 are listed technical characteristics of liquid starting pre-heaters that are used for the preliminary warm-up of vehicular engines.

Table 1

Technical characteristics of liquid starting pre-heaters for vehicles

Manufacturer	Model	Fuel	Maximum thermal power, kW	Electric power requirement, W	Vehicle type
Webasto [1]	Thermo Top Evo 4	diesel	4	35	With engine displacement up to 2.5l. (compact and subcompact cars)
		petrol			
	Thermo Top E	diesel	4	36	
		petrol			
Eberspächer [2]	Hydronic 4W SFL	diesel	4.3	35	
		petrol			
	Hydronic 4W SC	diesel	4.3	48	
		petrol			
Webasto [1]	Thermo Top Evo 5	diesel	5	47	With engine displacement 2.5 – 4 l (medium and executive cars, off-road vehicles, microbuses)
		petrol			
	Thermo Top C/P/Z	diesel	5.2	40	
		petrol			
	Thermo Pro 50	diesel	5.2	46	
		petrol			
Eberspächer [2]	Hydronic 5W S	diesel	5	53	
		petrol			
	Hydronic 5W SC	diesel	5	50	
		petrol			
Teplostar [5]	Binar 5	diesel	5.5	70	
		petrol			
	Binar 5-SV	diesel	5	45	
		petrol			
Webasto [1]	Thermo Pro 90	diesel	9.1	90	With engine displacement 4 – 10 l (buses, freight transport, motor homes, custom vehicles)
		petrol			
	Thermo Pro 90 ST	diesel			
		petrol			

Table 1(continued)

Eberspächer [2]	Hydronic D 8 W	biodiesel	8	80	With engine displacement 4 – 10 l (buses, freight transport, motor homes, custom vehicles)
	Hydronic D 10 W	diesel	9.5	86	
			12	120	
	Hydronic M		9.5	125	
Teplostar [5]	14TC-10-12	diesel	12	100	
	14TC-10		15	132	
	15TCГ	natural gas	12	128	
Webasto [1]	DBW 160	diesel	16	204	With engine displacement more than 10 l (freight transport with carrying capacity more than 10 t, trains, locomotives)
	DBW 230		23	214	
	DBW 300		30	204	
	DBW 350		35	195	
	NGW 300	natural gas	30	214	
	LGW 300	propane-butane		204	
	Thermo 230	diesel	23	169	
	Thermo 300		30	214	
	Thermo 350		35	244	
Eberspächer [2]	Hydronic L 16	diesel	16	164	
	Hydronic L 24		24	184	
	Hydronic L 30		30	209	
	Hydronic L 35		35	224	
Teplostar [5]	20 TS	diesel	20	200	
	20 TS-D38		20	210	

From Table 1 it follows that autonomous operation of starting pre-heaters of thermal power 4 kW for vehicles with engine displacement up to 2.5 l requires on the average 40 W of electric energy (power supply to air fan, fuel and circulation pumps, electronics 13.0; 12 – 14; 16; 0.5 – 1.0 W, respectively); ~50 W of electric energy for heaters of vehicles with engine displacement 2.5 – 4 l. For liquid starting pre-heaters used in vehicles with engine displacement 4 – 10 and more than 10 l the electric power of thermogenerators should be about 100 W and 200 W, respectively.

Apart from power supply to starting pre-heater components, thermoelectric generator can be also used as additional electric energy source for vehicle itself, in the first place for power supply to a standard fan of heating system. For instance, to warm up passenger compartment of cars and trucks, jeeps and microbuses, one should connect a 15 – 30 W standard fan of heating system. If part of electric energy (15 – 20 W) is provided for battery recharge, then total electric power output of thermal generator for vehicles with engine displacement up to 4 l should be 70 – 90 W, and for vehicles with engine displacement 4 – 10 l and more than 10 l it should be 130 – 150 W and 230 – 250 W, respectively.

TEG for air starting pre-heaters

In some cases the use of liquid starting pre-heaters is impossible (automobiles with air cooling of engine) or unreasonable – for instance, for heating of bus passenger compartments, sailboat cabins,

truck cabins during parking and camping. For such cases, autonomous air heaters of passenger compartments are created, whose technical characteristics are given in Table 2.

Table 2

Technical characteristics of air starting pre-heaters for vehicles

Manufacturer	Model	Fuel	Maximum thermal power, kW	Electric power requirement, W	Vehicle type
Webasto [1]	Air Top 2000 ST	diesel	2	29	With passenger compartment (cabin) volume up to 5 m^3 (microbuses, custom vehicles, cars and freight transport, trailers, small boats).
		petrol			
Eberspächer [2]	AIRTRONIC	diesel	2.2	34	
			3	24	
Teplostar [5]	PLANAR-4DM	diesel	3	42	
Truma [4]	Trumatic E2400	propane-butane	2.4	20	
	Trumatic E4400	propane-butane	3.7	30	
Ateso [6]	Breeze III	diesel	2	35	
		biodiesel			
Webasto [1]	Air Top Evo 3900	diesel	3.9	40	With passenger compartment (cabin) volume 5-8 m^3 (trucks, buses, rescue technique, custom vehicles, isothermal vans, yachts).
		petrol			
	Air Top Evo 40	diesel	4	40	
		petrol			
Eberspächer [2]	AIRTRONIC M	diesel	3.8	40	
		petrol	4	40	
Teplostar [5]	PLANAR-44D	diesel	4	62	
Pramotronik [11]	Pramotronic-4D	diesel	4	40	
Ateso [6]	Wind III	diesel	3.8	40	
Webasto [1]	Air Top Evo 5500	diesel	5.5	95	With passenger compartment (cabin) volume more than 8 m^3 (containers, cargo bays, trailers, buses, ships, custom vehicles).
	Air Top Evo 55	petrol			
	HL9	diesel	9	110	
Eberspächer [2]	AIRTRONIC L	diesel	5.5	80	
		petrol			
	AIRTRONIC D8LC	diesel	8	115	
Teplostar [5]	PLANAR-8DM	diesel	7.5	90	
Ateso [6]	X-7	diesel	8.2	100	

As is evident from Table 2, for vehicles with passenger compartment (cabin) volume up to 5 m^3 air heaters of thermal power 2 – 3 kW are overwhelmingly used. In so doing, their autonomous operation

requires on the average 35 W of electricity. Air heaters used in the vehicles with passenger compartment (cabin) volume 5 – 8 m^3 and more than 8 m^3 consume ~ 40 W and 100 W of electric energy, respectively. If another 20 – 30 W is provided for battery recharge and other requirements (for instance, power supply to on-board control panel, warning systems), total electric power output of thermal generator for air starting heaters will be about 50 – 70 W for the volume up to 8 m^3 and 130 – 150 W for vehicles with passenger compartment (cabin) volume more than 8 m^3. It is noteworthy that in case of air starting pre-heaters there is no need in power supply to standard vehicle heating fan, as long as hot air is fed to compartment by heater fan of its own.

TEG for start heating of ambulance cars

Among special-purpose vehicles, ambulance cars are especially noteworthy. It is due to the fact that start heating in the first place provides for temperature conditions in vehicle passenger compartment necessary for patient transportation.

According to international EN1789 and the National Standard of Ukraine DSTU 7032: 2009, ambulance cars are divided into three main classes [12, 13]:

“A” class vehicles are intended exclusively for patients that do not call for urgent help during transportation. Therefore, in such vehicles a set of medical equipment is minimum, namely medicines, bandaging materials, oxygen inhaler and bronchial aspirating means.

“B” class vehicles are intended for short-distance transportation of patients with a simultaneous emergency medical treatment. Vehicles of this class are stocked with the necessary equipment for intensive therapy and reanimation, namely oxygen-breathing, defibrillator, with a mandatory availability of cardiograph.

“C” class vehicles – reanimation ambulance cars – are intended for rendering aid to very ill patients: intensive therapy and reanimation by the efforts of medical team. Medical equipment is similar to that in “B” class ambulance cars.

Table 3

Electric power of medical equipment of B and C class ambulance cars

Medical equipment	Model	Electric power, W
Defibrillator	PRIMEDIC DEFI-B [14]	20
	PRIMEDIC XD [14]	18
	MASTER IC-9000A [15]	24
	DKI-N-04 [16]	22
	Cardio-Aid 200 [17]	21
Cardiograph	Heart Screen 80 GL [18]	18
	ECG-101 G [19]	22
	Cardipia 800 [20]	15
	Ucard 100 [21]	15
	ЕК 12Т-01 «Р-Д» [22]	10
	Heaco 300 G [23]	27
Artificial respirator	A-IVL/VVL-TMT [24]	12
	DAR-200 [24]	10
	Sirio S2T [25]	5
	Fasa-5-01 [26]	9.5

Table 3 lists the electric powers of some medical equipment models stocked for “B”, “C” class ambulance cars according to requirements of DSTU 7032: 2009.

Thus, the electric power requirement of the necessary minimum of medical equipment stocked for ambulance cars is 45 – 55 W.

Moreover, the above standards establish the requirements to temperature conditions in passenger compartment and power supply to medical equipment for all classes of ambulance cars [3, 4]:

Temperature conditions:

- the temperature in compartment should be at least 20°C. The time of reaching the temperature in compartment should not exceed 30 minutes at the ambient temperature -25°C and 60 minutes at -40°C.

- medical compartments of “B” and “C” class ambulance cars should be equipped with air conditioning system that must provide for air temperature reduction by 10°C within at least 30 minutes at ambient temperature 40°C.

- thermostatic control of heating system must assure temperature variation not more than ± 5°C.

Power supply:

- “B” and “C” class ambulance cars should be equipped with a start battery (12V, 80A·h) and supplementary battery (12V, 63 A·h) for power supply to medical instruments;

- a system that allows power supply from external grid 220V for medical equipment of corresponding voltage and batteries discharge during parking is a mandatory requirement;

- “B” and “C” classes must be stocked with voltage converter 12/220V for power supply to medical equipment of voltage 220 V and power from 250 to 500 W;

- vehicle electric system must be adapted for storage of electric energy necessary for resumption of engine operation.

On the whole, total electric energy requirement of equipment used for ambulance car, with regard to lighting (20 – 30 W), ventilation (3 – 5 W) and vehicle heater (30 – 40 W) is 140 – 150 W.

With intensive operation of ambulance car for 4 – 5 hours, the capacity of start and supplementary batteries is reduced by about 40 – 50 %. This not only creates difficulties of engine starting, but also impairs efficient operation of ambulance cars in general.

So, the use of thermoelectric generator for autonomous start heating of ambulance cars and additional power supply to medical equipment is particularly promising and relevant.

Moreover, the use of such sources of heat and electricity will provide for heating of passenger compartment and battery recharge with an idle engine or at parking place, which is necessary to perform the functions of ambulance cars and their reliability enhancement.

Conclusions

1. It is shown that total electric power of thermal generator for starting pre-heaters of vehicles with engine displacement up to 4 l should be 70 – 90 W, for vehicles with engine displacement 4 – 10 l and more than 10 l – 130 – 150 W, 230 – 250 W, respectively. Such electric powers of thermal generator will provide for not only autonomous operation of starting pre-heaters, but also allow power supply to standard vehicle heating fan and battery recharge.
2. It is established that total electric power output of thermal generator for air starting heaters used in the vehicles with passenger compartment (cabin) volume up to 8 m^3 should be within 50 – 70 W and 130 – 150 W for vehicles with the volume more than 8 m^3. Apart from autonomous operation of air heater components, the excess electric energy of thermal generator can be used for battery recharge and power supply to other automobile equipment (on-board control panel, warning systems).
3. For ambulance cars the use of starting pre-heater allows creating the necessary temperature

conditions in the passenger compartment. The use of a 60 – 90 W thermoelectric generator will assure autonomous operation of such heaters and additional power supply to the necessary minimum of medical equipment in the cars (cardiograph, defibrillator, artificial respirator). Moreover, the use of such combined heat and electricity sources will assure heating of passenger compartment in a car and allow recharging of supplementary and starter batteries with an idle engine or at parking places.

References

1. http://www.webasto.com/ua/
2. http://www.eberspaecher.ua
3. http://www.mikuni.co.jp/e/
4. http://www.trumatic.ru
5. www.teplostar.com.ua/
6. www.brano.eu/
7. .V.S.Naiman, All about Starting Pre-Heaters (Moscow: ACT, 2007), p. 213.
8. V.Ya.Mykhailovsky, M.V.Maksimuk, Automobile Operating Conditions at Low Temperatures. The Necessity of Applying Heaters and the Rationality of Using Thermal Generators for their Work, J.Thermoelectricity 3, p.18 – 27 (2015)
9. Patent UA № 72304, InCl: F01N 5/00; H01L35/00. Automobile Heater with Thermoelectric Power Source /L.I.Anatychuk, V.Ya.Mykhailovsky. Publ.10.08.2012, Bul. № 15, Application u2012 02055 of 23.02.2012.
10. Patent UA for Invention № 102303, InCl F01N 5/00 H01L 35/00. Thermoelectric Power Source for Automobile / L.I.Anatychuk, V.Ya.Mykhailovsky. Publ. 25.06.2013, Bul. № 12, Application u2011 13957 of 28.11.2011.
11. www.pramotronic.ru
12. CEN/TC 239 N 354, Medical Vehicles and their Equipment - Road Ambulances.
13. DSTU 7032:2009, Ambulances and their Equipment, Technical Requirements and Method.
14. www.primedic.com/
15. http://www.smsstayer.ru/products/?ELEMENT_ID=445
16. www.axion-med.ru/
17. http://cardiomc.com.ua
18. www.innomed.hu/
19. www.biomed.ua/
20. www.trismed.com/
21. www.medion.com.ua/
22. www.medrk.ru/
23. www.heaco.ua/
24. www.medplant.ru/
25. http://www.siare.it/it/index.php
26. http://www.medsooo.ru

Submitted 2.09.2015

L.I. Anatychuk, R.V. Kuz, D.D. Taschuk

Institute of Thermoelectricity of the NAS and MES of Ukraine,
1 Nauky str., Chernivtsi, 58029, Ukraine

DIFFERENTIAL THERMOELECTRIC AC CONVERTER IN THE NON-SIMULTANEOUS COMPARISON MODE

Computer simulation was used to obtain potential and temperature distributions in a differential thermoelectric measuring converter in the non-simultaneous comparison mode. The error of alternating current conversion was calculated. The results of simulation were compared to the data deduced from experiments. The results of simulation were satisfactorily proved by the experimental data.
Key words: differential alternating current converter, computer simulation.

Introduction

The accuracy and reliability of modern standards, electric measuring instruments and set-ups for determination of effective (root - mean - square) value of alternating current, voltage, power and power coefficient over a wide range of frequencies to a large extent depends on the parameters and characteristics of measuring converters that serve the basis for these instruments.

From experience of international comparisons of AC standards it is known that measurement of AC voltage and power in a wide frequency range can be brought up to date using direct current thermoelectric comparison methods. So, metrological centres in many countries pursue active development of new thermoelectric measurement instruments and means for their metrological assurance using thermoelectric comparison [1 – 3].

The basic element of thermoelectric method for measurement of AC voltage and power is a measuring thermal converter wherein the energy of measured current is converted into thermal energy which is released in a resistive heater and again converted into electric energy with the aid of a thermoelement. In the case of known relationships between the value of alternating current and thermoelement thermopower, alternating currents can be measured by direct current equipment [4].

To improve the accuracy of conversion, in modern AC metrology wide acceptance has been gained by converters based on thermopiles [5, 6]. In such thermal converters the heater is in thermal contact to the junctions of a large number of thermocouples (50 – 120 pcs) that are series-connected into a thermopile. The use of thermopile converters makes it possible to improve considerably the accuracy of current conversion (due to reduced impact of the Thomson effect), to reduce the operating temperature of the heater and, hence, to minimize the impact of temperature coefficients of heater and thermocouple material parameters on the quadratic volt-ampere characteristic and to increase overload capacity.

Converters based on thermopiles are manufactured by thin - film technique. Because of their low efficiency film thermocouples must be used in big quantities, which increases thermopile resistance to several tens of kΩ, the noise and the electric capacity between the heater and thermocouple, which restricts the high-temperature range of their application.

Differential thermoelectric converters (DTC) are free from the above mentioned disadvantages. DTC are intended for simultaneous comparison instruments when creating standard and calibration means for metrological assurance of transmitting information on electric measurement units from state standards to working standards and alternating voltage and current measures, analog and digital measurement instruments. However, there are cases when DTC are used in the non-simultaneous comparison mode [7]. Essential use of computer design methods is quite rare. Particularly interesting is computer simulation with the use of differential converters under non-steady-state operating conditions.

The purpose of the work is development of computer-aided method for studying converters and realization of this method on a DTC working under specific conditions.

The object for study is a differential thermoelectric converter DTPT - 6 developed at the Institute of Thermoelectricity.

The subject for study is temperature and electric potential distributions in the heaters and thermocouple legs.

Physical model of a differential thermoelectric measuring converter

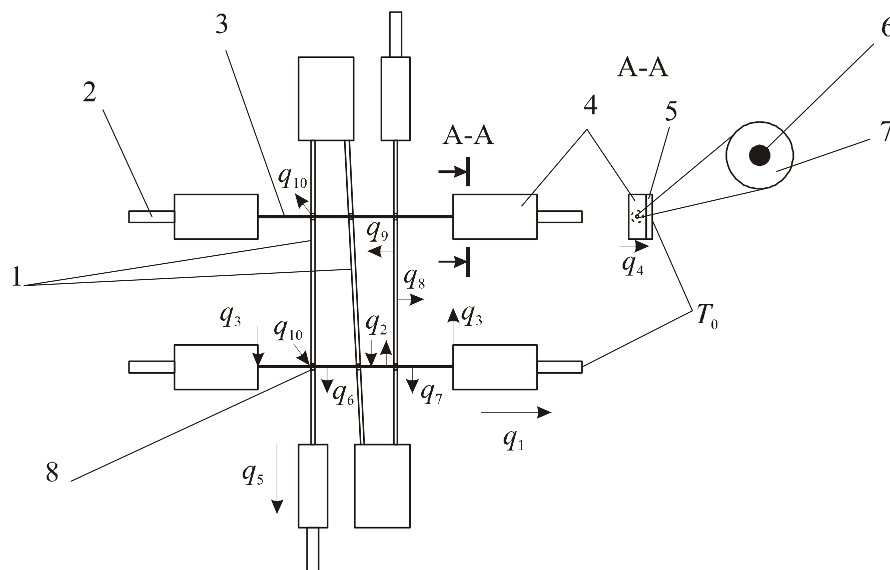

Fig. 1. Physical model of a differential thermoelectric measuring converter.
1 – differential thermocouple legs, 2 – current leads, 3 –heater in glass insulation, 4 – solder layer, 5 – copper contact plate, 6 – manganin heater, 7 – glass insulation of heater, 8 – thermocouple junction.

A differential thermoelectric measuring converter comprises a manganin wire heater in glass insulation 3 attached to current leads 2 by means of solder 4, a differential thermocouple 1 attached to current leads 2 by means of solder 4 and being in thermal contact to the heater at junction points 8.

Current flowing through the heater causes heat release which through the contact at junction points is passed to the thermocouple where thermopower is created. Due to losses through thermal conductivity from the heater q_1 and thermocouple q_2, radiation q_6 and q_8, and convection q_7 and q_9, not all the heat released by the heater is spent on warm-up of thermocouple junctions. Also, the Peltier effect works on the heater junctions with current leads, which manifests itself in the release or absorption of heat q_3, and the Thomson effect works in the bulk of the heater, as a result of which heat q_2 is released or absorbed. The Peltier and Thomson effects cause the origination of asymmetry error

in measurement – with the identical root-mean-square values of AC and DC current the thermopower output will be different. Current generated by the thermocouple causes the origination of the Peltier effect on thermocouple junctions which leads to release or absorption of some amount of heat q_{10}.

Mathematical model of a differential thermoelectric measuring converter

A physical model of a differential thermoelectric converter is described by systems of equations (1) and (2)

$$\begin{cases} \nabla\left(k\nabla T\right)+Q_j=0 \\ \nabla j=Q_j \\ j=\sigma E+j_e \\ E=-\nabla V \end{cases}, \tag{1}$$

$$\begin{cases} \nabla\times\vec{E}=-\dfrac{\partial\vec{B}}{\partial t} \\ \nabla\times\vec{H}=\vec{j}+\dfrac{\partial\vec{D}}{\partial t} \\ \nabla\cdot\vec{D}=\rho \\ \nabla\cdot\vec{B}=0 \end{cases}, \tag{2}$$

where Q_j is thermal flux due to the Joule effect, T is absolute temperature, k is thermal conductivity coefficient, D is electric induction, B is magnetic induction, E is electric field intensity, H is magnetic field intensity, j is current density, σ is electric conductivity, V is potential, T is absolute temperature, k is thermal conductivity coefficient.

Equation systems (1) and (2) are solved with the boundary conditions (3) and (4):

$$\begin{cases} T\big|_{z=0}=T_{amb} \\ q\big|_{z\neq0}=\alpha(T_{amb}-T)+\varepsilon\sigma_Б(T_{amb}^4-T^4) \end{cases}, \tag{3}$$

$$\Big\{ V\big|_{\substack{x=a\\y=b}}=0\,, \tag{4}$$

where q is heat flux density, T is absolute temperature, T_{amb} is ambient temperature, α is heat exchange coefficient, ε is emissivity factor, $\sigma_Б$ is the Boltzmann constant, V is potential, I is rated current through the heater.

Computer model of a differential thermoelectric measuring converter

In order to obtain temperature and potential distributions, a three - dimensional computer model of a differential thermoelectric measuring converter was created. Computer model was built with the use of Comsol Multiphysics applied program package that allows solving equations by finite element method. Fig. 2 shows finite element method mesh.

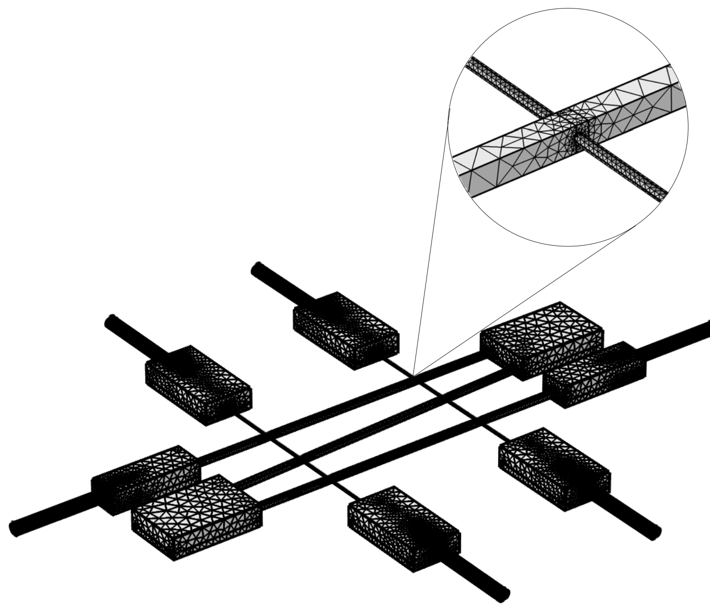

Fig.2. Finite element method mesh.

In the model, the measuring DTC was assumed to be in the air.

For direct current, calculations have shown that at a rated current $I = 7$ mA the output thermopower is $E = 23.000004$ mV, which corresponds to experimentally established data. Also, the distributions of temperature (Fig. 3, 4) and potential (Fig. 5) in the measuring differential thermoelectric converter (DTC) were obtained.

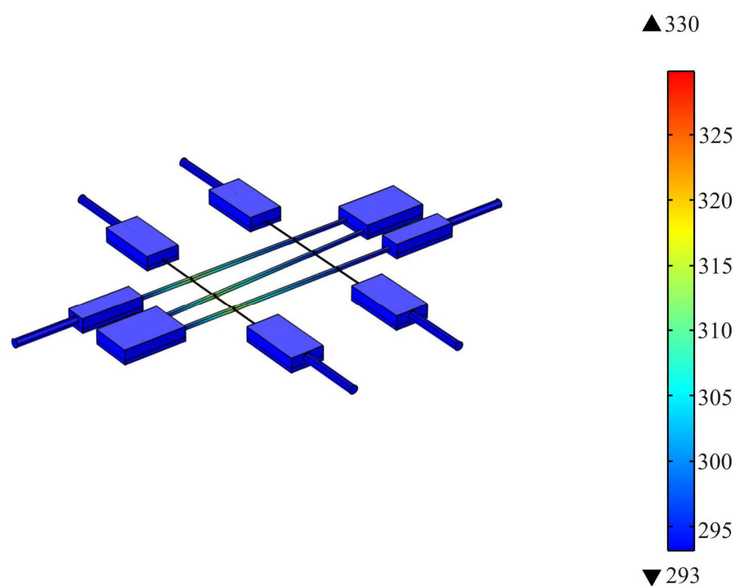

Fig. 3. Temperature distribution in DTC under study.

The use of alternating current in the model necessitated the use of calculation module consisting of two steps. *Heat transfer in solids* module does not work with *frequency domain* calculation module, so calculations of the electric part were made in *frequency domain*, and then the results were transferred to *heat transfer in solids* module which was calculated in *stationary domain* module.

Maximum temperature to which the heater is heated in the process of measurement affects its

overload capacity. At a temperature above 373 K, irreversible changes appear in a manganin microwire with a negative effect on thermal converter's characteristics. Fig. 4 shows temperature distributions in the heaters of the measuring DTC.

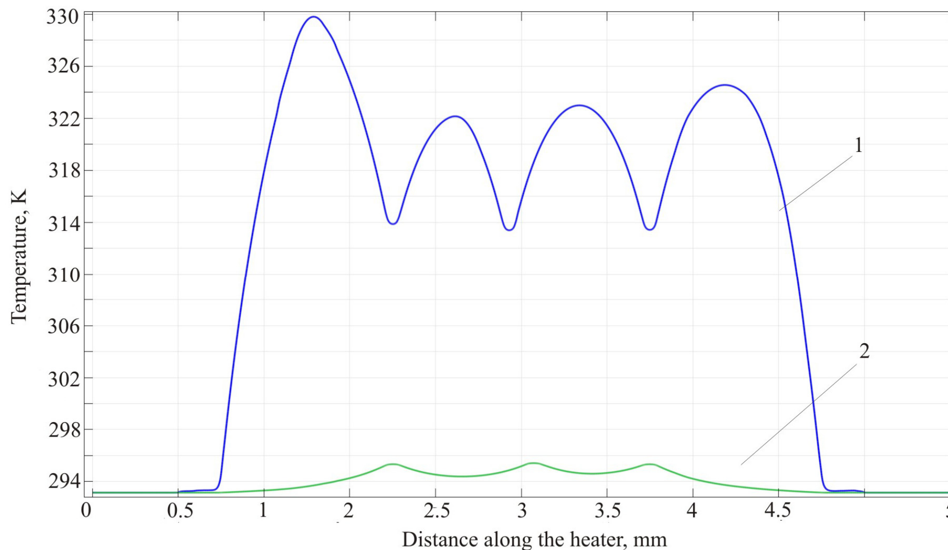

Fig. 4. Temperature distributions: 1 – in a heater with direct current flow, 2 – in a heater without current flow.

From Fig. 4 it is seen that at no heater point the temperature exceeds 330 K, hence no irreversible changes take place in the heater material both at DC and AC that can lead to degradation of DTC performance.

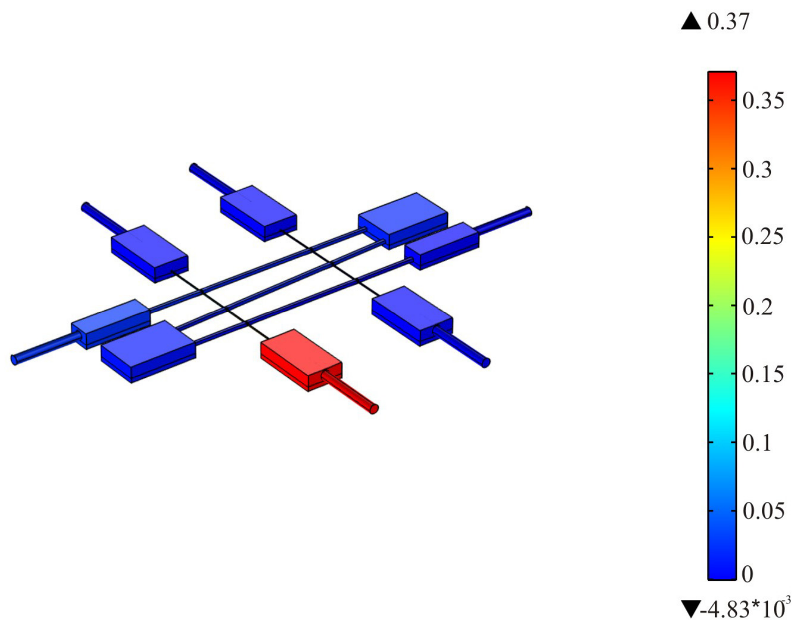

Fig. 5. Electric potential distribution in DTC under study.

Fig. 6 gives a comparison of calculated error of AC conversion in the frequency range of 1 kHz – 30 MHz to the experimental data.

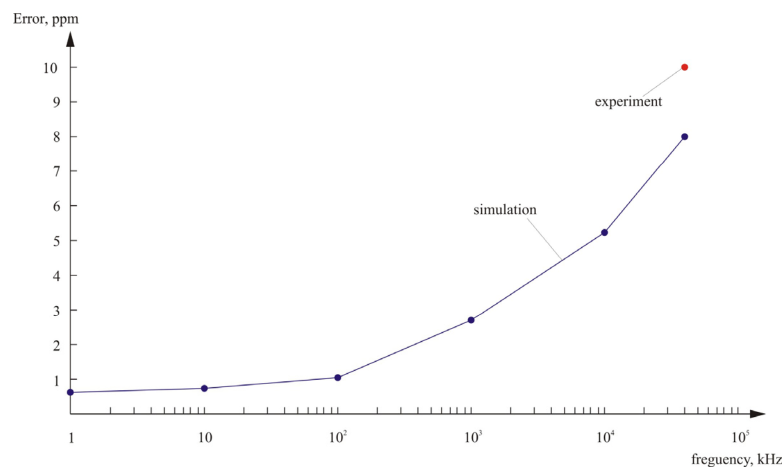

Fig. 6. Calculated conversion error versus measured signal frequency.

For AC frequency 30 MHz calculations have shown that with the effective current value $I = 7$ mA the thermopower output $E = 23.000184$ mV. In so doing, conversion error is 8 ppm, which correlates satisfactorily with the data deduced from experiments.

Conclusions

1. Computer model was built and potential and temperature distributions were obtained in a differential measuring converter in the non-simultaneous comparison mode.
2. It is shown that at a rated current of 7 mA the heater temperature does not exceed 330 K, leading to no performance degradation of the heater material.
3. The calculated error of DTPT alternating current conversion differs from the experimental data not more than by 20%.
4. The elaborated model can be used in the design of new thermal converters with the alternative geometry of elements.
5. The represented results were used in the development of Military secondary reference standard of alternating voltage.

References

1. T.F Wunsch., J.R. Kinard, R.P. Manginell, O.M. Jr. Solomon, T.E. Lipe, and K.C. Jungling, *IEEE Transactions on. Instrumentation and. Measurement* (2001), p.330.
2. J.R. Kinard, T.E. Lipe, and T.F. Wunsch, *Digest of the Conference on Precision Electromagnetic Measurements* (Canada, 2002), p.364.
3. T.E. Lipe, C.D. Reintsema, and J.R. Kinard, *CPEM 2002 Conference Digest* (Canada, 2003), p.108.
4. L.I.Anatychuk, *Thermoelements and Thermoelectric Devices: Reference Book* (Kyiv: Naukova Dumka, 1979), 768 p.
5. M.Klonz, H.Laiz, and E.Kessler, Development of Thin-Film Multijunction Thermal Converters at PTB/IPHT, *IEEE Transactions on Instrumentation and Measurement* 50(6), 1490 – 1498 (2001).
6. Y.H.Lee, S.W.Kwon, K.J.Kim, S.I.Park, and Y.E..Ihm, Performance Improving of KRISS Micromachined Multijunction Thermal Converter, IEEE Transactions on Instrumentation and Measurement. P 591 – 592 (2004)
7. Yu.M.Tuz, M.V.Dobrolyubova, Yu.V.Artyukhova, Yu.A.Strunina, V.I.Bodnaruk, and D.D.Taschuk, AC Voltage Unit Standard Based on Thermoelectric Converters, *J.Thermoelectricity* 3, P 76 – 86 (2012).

Submitted 17.08.2015

L.I.Anatychuk[1], M.V.Havrylyuk[1], V.V.Lysko[1], V.A.Tyumentsev[2]

[1]Institute of Thermoelectricity of the NAS and MES of Ukraine,
1 Nauky str., Chernivtsi, 58029, Ukraine,
[2]NPO “VLANT”, str. Matrosov, 20, Chernivtsi, 58001, Ukraine

AUTOMATED EQUIPMENT FOR MEASUREMENT OF PROPERTIES OF THERMOELECTRIC MATERIAL RODS

The paper presents the results of development of equipment for measurement of electric conductivity and thermopower distributions along thermoelectric material rods. The deviations of a real physical model of measuring equipment from the ideal model of measuring method, as well as the results of calculation of measurement errors caused by these deviations are analyzed. The method for measurement of thermal conductivity of rods is developed. A description of measuring equipment design with automation of measurement process to increase the rapidity of action and eliminate human errors is given. The use of such equipment in the manufacture of thermoelectric modules allows reducing thermoelectric material consumption to ~ 10% with a simultaneous quality enhancement of thermoelectric products by ~ 8 - 15%.

Key words: electrical conductivity, thermal conductivity, thermalEMF error thermoelectric material, automation.

Introduction

General characterization of the problem. In the production of thermoelectric modules it is important to assure step-by-step quality control of thermoelectric materials. No less important is selection of material with specified properties, optimized for each particular task. The first step of such control is measurement of properties of thermoelectric material rods.

Analysis of the literature. The electric conductivity of rods is successfully measured by a two-probe method [1]. In [2 – 5], a detailed analysis of the sources of errors of this method is given and the ways for their minimization are proposed.

To determine the Seebeck coefficient of rods, a hot probe method is generally used [6] allowing to find the local value of thermopower at probe contact point.

In [7], a description of experimental setup for determination of electric conductivity and thermopower of probes developed by the Institute of Thermoelectricity (Ukraine) is given. The measurement errors of this setup are ~ 1% for electric conductivity and ~ 2% for the Seebeck coefficient. The disadvantageous feature of this equipment is manual mode of measurement and processing of the results.

The purpose of this work is to develop equipment for measurement of properties of thermoelectric material rods through use of automation of measuring probes travel, measured results processing and plotting the distribution of material properties in the rod.

Physical, mathematical and computer models of the method

A physical model for the development of methods for determination of electric conductivity and the Seebeck coefficient of rods is given in Fig. 1. The electric conductivity was measured with the use

of a two-probe method, and the Seebeck coefficient – with the use of a hot probe method. The physical model takes into account cooling and heating of the opposite ingot edges due to the influence of the Peltier heat Q_1, the release of the Joule heat Q_2 in the ingots and current conductors, as well as heat exchange between the ingot, current conductors and measuring probes and the environment ($Q_3 - Q_{11}$).

For calculation of the errors and optimization of measurement method it is necessary to find the distributions of electrical potential φ and temperature T in the ingot that can be obtained from the laws of conservation of electrical charge and energy written as:

$$\begin{cases} -\nabla\left(\left(\kappa_j+\alpha_j^2\sigma_j T+\alpha_j\varphi\sigma_j\right)\nabla T\right)-\nabla\left(\left(\alpha_j\sigma_j T+\varphi\sigma_j\right)\nabla\varphi\right)=0, \\ -\nabla\left(\sigma_j\nabla\varphi\right)-\nabla\left(\sigma_j\alpha_j\nabla T\right)=0, \end{cases} \quad (j=1..10), \qquad (1)$$

where α_i, is the Seebeck coefficient, σ_i is an electric conductivity and κ_i is a thermal conductivity of the elements of physical model.

The boundary conditions for such a physical model:

– the lateral surfaces of the ingot and current conductors are electrically insulated

$$\mathbf{n}\cdot\mathbf{j}=0;$$

– current of I flows through current conductors

$$\mathbf{n}\cdot\mathbf{j}=I/S_{cm.};$$

– the ends of current conductors are thermostated at ambient temperature T_0

$$T=T_0;$$

– the lateral surfaces of the ingot, measuring probes and current conductors are in a state of heat exchange with the environment

$$\mathbf{n}\cdot\mathbf{q}=h_n(T_0-T),$$

where h_n are heat transfer coefficients.

This problem was solved with the use of computer object-oriented simulation with application of finite element method implemented in Comsol Multiphysics package of applied programs.

The main sources of errors in the measurement of electric conductivity:

– current density inhomogeneity in the ingot due to current supply to ingot end only at points of contact to current conductors, rather than uniformly along its entire surface;

– non-isothermal conditions caused by the influence of the Peltier and Joule effects, as well as by heat exchange with the environment.

It was established that the errors due to current density inhomogeneity near the ends can be considerable – more than 45% – in the case when current supply to the ingot is done by one point current conductor on each end (Fig. 2).

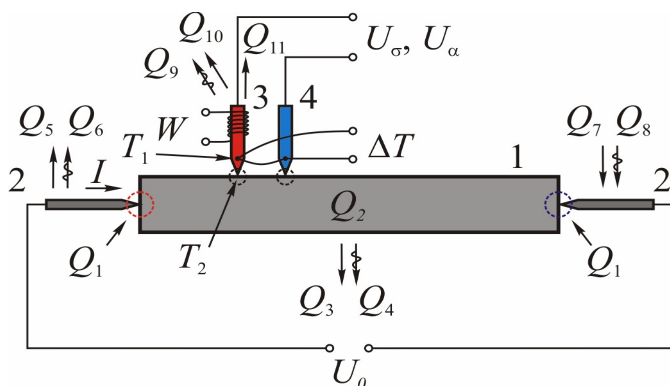

Fig. 1. Physical model of measuring the electric conductivity and Seebeck coefficient of ingots. 1 - ingot, 2 – current conductors 3, 4 – measuring probes.

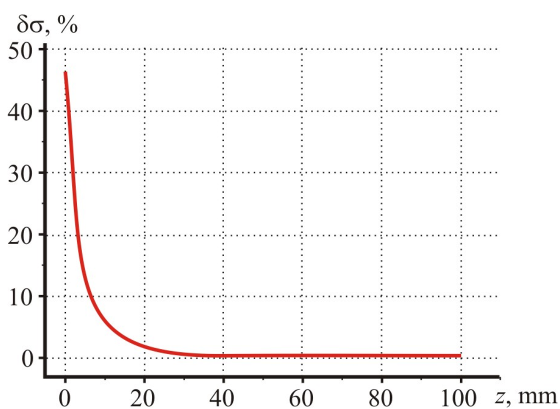

Fig. 2. Dependence of electric conductivity measurement error due to current density inhomogeneity on the distance z from the probes to ingot edge.

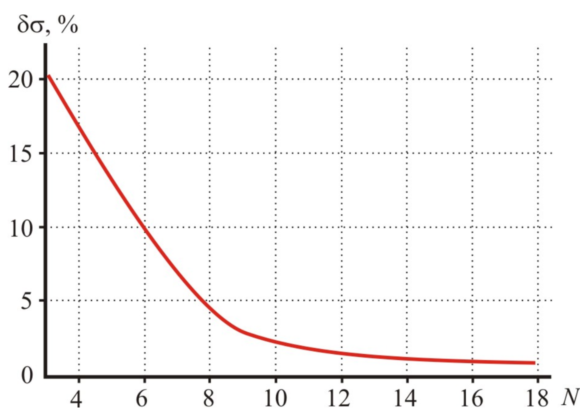

Fig. 3. Dependence of electric conductivity measurement error due to current density inhomogeneity on the number of current contacts N.

The situation is improved with increasing the number of current conductors (Fig. 3). For the case of three points the error is about 20%. Computer simulation made it possible to determine the optimal number of contact points – 16 on each end. Measurement error due to current density inhomogeneity is reduced here to 0.9%.

A method eliminating the influence of the Peltier effect by using optimal current through the ingot was also developed, whereby cooling action of the Peltier effect is compensated by the Joule heat. The error in this case is reduced from 6 to 0.3% (Fig. 4).

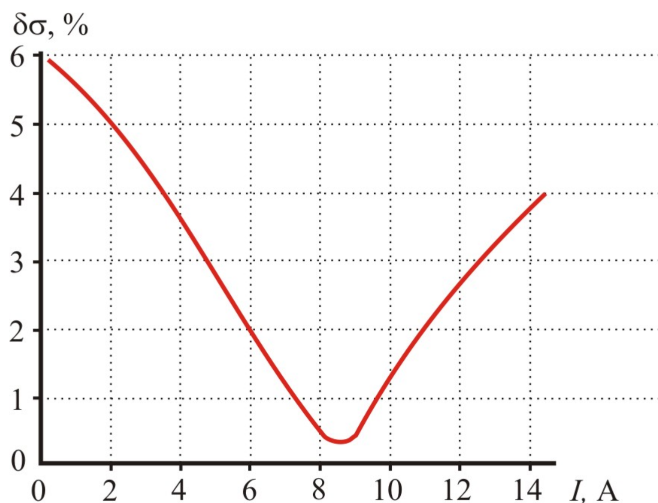

Fig. 4. Dependence of electric conductivity measurement error due to the Peltier effect on the distance from current through the ingot.

Total error of electric conductivity measurement with regard to instrumental errors is 1.5%. Thus, using the elaborated methods the accuracy of electric conductivity measurement near the ends has been increased more than a factor of 15.

The errors in the determination of the Seebeck coefficient are caused by the difference between temperature T_1 at point of thermocouple location on the probe and temperature T_2 at point of probe contact with the rod surface. Computer simulation was used to obtain the dependences of correction factor K on measuring probe geometry in order to take this temperature difference into account in the calculation of the Seebeck coefficient

$$\alpha = \frac{U_\alpha}{K\left(T_1 - T_0\right)}.$$

The probe with a cone-shaped tip was used. The probe base diameter was d_1, the probe tip diameter - d_2. Figs. 5, 6 show the dependences of correction factor K on probe dimensions for the cases of copper (1) and tungsten (2) tip.

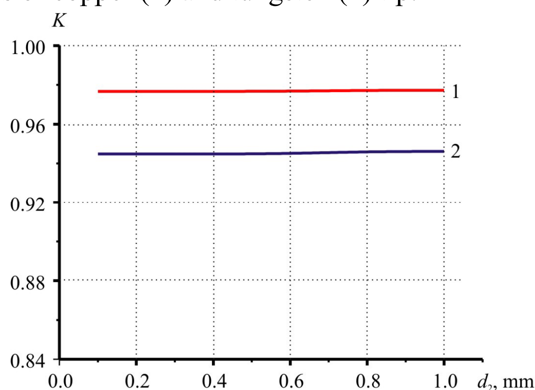

Fig. 5. Dependences of correction factor for calculation of the Seebeck coefficient of ingot on probe tip diameter.

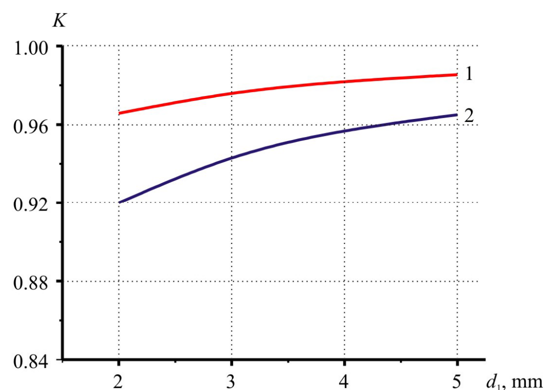

Fig. 6. Dependences of correction factor for calculation of the Seebeck coefficient of ingot on probe base diameter.

A method for measuring thermal conductivity of ingots was developed, too. For this purpose a computer model was studied that allows finding temperature distribution in the ingot at an arbitrary time moment. An ingot of thermoelectric material was considered having on one of its end faces an electric heater. The temperature distribution equation is of the form:

$$\rho C\frac{\partial T}{\partial t} + \nabla\left(-\kappa\nabla T\right) = 0, \qquad (2)$$

where ρ is a density, C is heat capacity, κ is a thermal conductivity of ingot material.

Solving of Eq. (3) with the boundary conditions that take into account heat exchange between the ingot and the environment yielded calibration curves for determination of thermal conductivity of material from the time of reaching given temperature difference between two points on the surface of the ingot (Fig. 7).

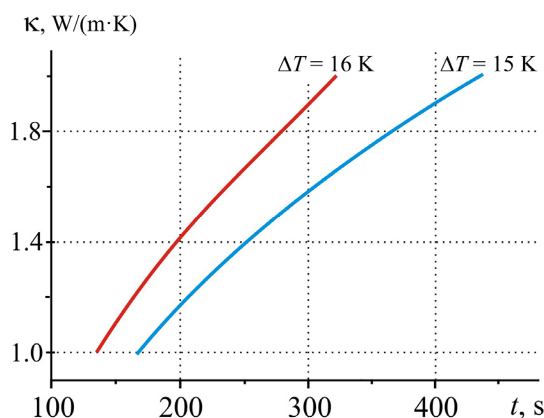

Fig. 7. Calibration dependences for determination of thermal conductivity of the ingot.

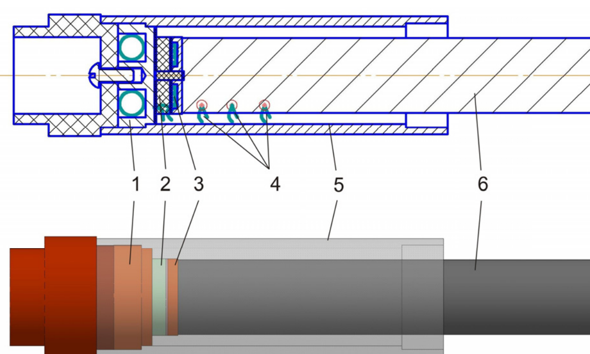

Fig. 8. Design of device for measuring thermal conductivity of ingots.

Device for determination of thermal conductivity and its external appearance is shown in Fig. 8. It comprises a reference heater 3, thermocouples-probes 4, a screen heater 1, a differential “zero

thermocouple” 2 and a screen tube 5. Thermal conductivity is determined by the rate of reaching given temperature difference between thermocouples.

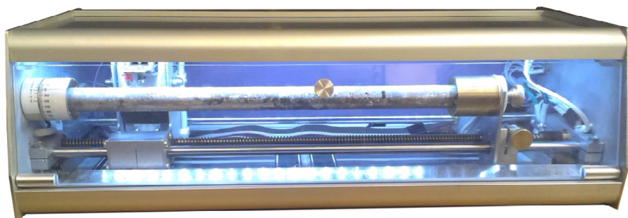

Fig. 9. External appearance of ingot holder.

The above described methods were used to develop equipment for investigation of properties of ingots whose external appearance is given in Fig. 9. The equipment is fully automated, including travel of probes and rotation of ingot about its axis, as well as the process of measurement and processing of results.

Jointly with the state enterprise “Chernivtsi Regional Scientific-Production Centre for Standardization, Metrology and Certification” (State Enterprise “Bukovinastandartmetrologiya”) the methods for metrological certification of this equipment have been developed and tests have been performed that confirmed its high precision and reproducibility of results: the error of electric conductivity measurement not more than 0.5% and the error of thermopower measurement not more than 1%; the error of thermal conductivity determination not more than 10%.

The elaborated equipment for determination of properties of rods can be helpful in the production of thermoelectric modules. It yields material saving of about 10% and improves the quality of modules by 8 – 15%.

Conclusions

1. Computer simulation methods have been used to determine the influence of various errors on the accuracy of measuring electric conductivity and thermopower of thermoelectric material rods. Conditions for minimization of the influence of these errors have been found.
2. Based on the results of computer simulation, an automated setup has been developed for measuring electric conductivity and thermopower of rods, as well as automatic processing of measurement results. The error of electric conductivity measurement is ~ 0.5%, of thermopower - ~1%.
3. Measuring setup is equipped with a device for determination of thermal conductivity of the rod in dynamic mode. The error of thermal conductivity determination is ~10%.
4. The use of the above described measuring equipment in production practice for the manufacture of cooling modules allows reducing thermoelectric material consumption up to 10% and improving quality of modules up to 8 – 15%.

References

1. L.I.Anatychuk, *Thermoelements and Thermoelectric Devices* (Kyiv: Naukova Dumka, 1978), 768 p.
2. V.V.Razinkov, Equipment for Measuring Parameters of Thermoelectric Material Ingots, *J.Thermoelectricity* 4, 70 – 79 (2002).
3. V.V.Lysko, Research on the Errors in Measuring the Electric Conductivity of Thermoelectric Material Rods, *J.Thermoelectricity* **4**, 49 – 54 (2006).
4. L.I.Anatychuk, V.V.Lysko, High Precision Method for Measuring the Electric Conductivity of Thermoelectric Material Rods, *J.Thermoelectricity* **1**, 70 – 75 (2008).
5. L.I.Anatychuk, V.V.Lysko, Measurement of Thermoelectric Parameters on Rods, *Proc. of XI*

Interstate Workshop "Thermoelectrics and Their Applications" (Russia, Saint-Petersburg, 2008), p. 464 – 469.

6. A.S.Okhotin, A.S.Pushkarsky, R.P,Borovikova, and V.A.Simonov, *Methods for Measuring Characteristics of Thermoelectric Materials and Converters* (Moscow: Nauka, 1974), 167p.
7. L.I.Anatychuk, N.V.Havrylyuk, and V.V.Lysko, Methods and Equipment for Quality Control of Thermoelectric Materials, *J.Electronic Materials* **41**(6), 1680 – 1685 (2012).

Submitted 10.09.2015.

R.R. Kobylianskyi

R.R. Kobylianskyi[1,2], I.A. Moskalyk[1]

[1]Institute of Thermoelectricity of the NAS and MES of Ukraine, 1 Nauky str., Chernivtsi, 58029, Ukraine;
[2]Yu. Fedkovych Chernivtsi National University, 2, Kotsyubinsky str., Chernivtsi, 58012, Ukraine.

I.A. Moskalyk

THE PROSPECTS OF USING THERMOELECTRICITY FOR HUMAN HEAD CRYOTHERAPY

The paper presents the analysis of current status of using human brain cooling in medical practice. The operating principle of currently available devices for brain hypothermia, their advantages and shortcomings are briefly described. The prospects of using thermoelectricity for human head cooling are determined.
Key words: *thermoelectricity, human head cooling, local hypothermia, brain hypoxia.*

Introduction

General characterization of the problem. Brain hypoxia is one of the relevant problems in medical practice [1 – 8]. It is present at cerebrovascular accidents, shock states, acute cardiovascular insufficiency, complete atrioventricular heart block, head injuries, carbon monoxide poisoning and asphyxia of different origin. Brain hypoxia can be a complication of cardiac surgery and vascular procedures, as well as in the early postoperative period. It is accompanied by various neurologic syndromes and mental disorders.

With oxygen starvation for more than 3 – 4 minutes rehabilitation of brain activity becomes impossible. However, it is known that local hypothermia of brain reduces its oxygen requirement, increases resistance to hypoxia, as well as reduces or even removes the danger of temporary brain ischemia, thus increasing permissible duration of oxygen starvation [9 – 10]. Thus, for instance, cooling by as low as 5°C increases brain lifetime by several times. Hypothermia is recommended with various head injuries, cardiac surgeries, as well as in the postoperative period – with hypoxic brain edemas, intoxication and central nervous system injuries.

Generally, the existing equipment for human head cooling includes large-size stationary devices based on compressor refrigerating units. Though in recent times devices based on thermoelectric cooling become available which, despite obvious advantages, have not found widespread application.

Therefore, *the purpose of the work* is to determine the prospects of using thermoelectricity for human head cooling.

Effect of cooling on human brain activity

Low temperatures as one of the physical factors of influence on human organism with a curative purpose are widely used in medical practice as a method for reducing organism reaction to surgical intervention, prevention of severe hypoxia progression and increasing brain resistance to oxygen starvation. Craniocerebral hypothermia method is used for complex treatment of various hypoxic and posthypoxic states. For instance, with craniocerebral injuries, when disturbed cerebral circulation and gas exchange result

in brain edema, craniocerebral hypothermia offers the opportunity to prevent increase in intracranial pressure and brain edema by head cooling to temperature 30°C.

The methods for therapeutic hypothermia in emergency medicine are based on the following principles of heat removal: external cooling of large body areas, cooling of organ cavities (stomach, rectum), extracorporal and intravenous blood cooling. Of special note is craniocerebral hypothermia method (brain cooling through head skin cover with a view to improve its resistance to oxygen starvation). There are the following types of craniocerebral hypothermia: moderate hypothermia 37 – 35°C (characterized by adaptation of organism to cooling and development of compensatory functions aimed at preservation of thermoregulation), medium hypothermia 34 –30°C (characterized by instability of organism functions and increased generation of heat) and deep hypothermia 29 – 24 °C (minimization of vital organism functions – some acquired reflexes disappear, peripheral nerve conductivity, pulmonary ventilation and O_2 utilization by organism tissues are reduced, moreover, heartbeat rhythm is also reduced by 64 % and blood pressure is decreased).

Besides, craniocerebral hypothermia is an efficient method for increasing biological tissue resistance to oxygen starvation, as long as in this case there is neurovisceral system block. With craniocerebral hypothermia the temperature of the head is reduced 2 – 3 times quicker than with a general cooling of the body. The advantages of this method include quick onset of neurovisceral block that cannot be achieved in time by means of medicines. A moderate depth of craniocerebral hypothermia is achieved in 20 – 25 minutes at rectal temperature 37 – 35°C. With a deep craniocerebral hypothermia that comes in 25 – 30 minutes, rectal temperature reaches 30 – 24°C, and cerebral temperature – 25°C. Moderate craniocerebral hypothermia is an unstable cooling phase, whereas with a deep hypothermia the changes in the organs and tissues are stabilized. Thus, at the stage of a deep craniocerebral hypothermia arterial blood pressure is reduced to 51.5%, minute volume of blood is as low as 59.5%, arterial blood pressure and blood flow in liver are halved.

Note that during the first minutes of brain oxygen starvation thousands of cells die away, that can lead to irreversible changes, so it is important to minimize mass death of human brain cells. It is done due to local hypothermia of human head that brings about suppression of metabolic processes, reduction of oxygen consumption and increase of resistance to hypoxia. In medical practice it has been established that optimal temperature of cold carrier (water, air) that contacts the surface of human head is +2°C. Lower temperatures are dangerous for human organism because of frostbite of skin cover. In so doing, the temperature of patient' body is measured at several points (inside acoustic meatus at the level of ear drum, in nasal pharynx, esophagus and rectum). The temperature inside acoustic meatus at the level of ear drum corresponds to the temperature of cerebral cortex at the depth of 25 mm from the inner scull cap. Cooling continues till the temperature in rectum becomes at least equal to 33 – 32°C, in esophagus – 32 – 31°C. After craniocerebral hypothermia it is recommended to actively warm the patient to temperature not higher than 35°C, further warming of the patient should be gradual [1 – 10].

Currently available devices for human head cooling

So far, more than ten experimental devices have been developed for human brain hypothermia through external skin cover or upper air passages [17 – 30]. Such devices are based on refrigeration apparatus (generally compressor type) for cold carrier cooling and a hydraulic system that assures forced circulation of cold carrier through cryoapplicator. As cold carrier, the majority of devices employ water at a temperature of +5 °C. Control of cooling modes of such devices is done by regulation of cold carrier circulation rate through cryoapplicator on achievement of given level of temperature reduction of the biological tissue of cooled area.

It should be noted that surface heat removal at local hypothermia is mainly due to thermal conductivity and must be more energetic than own thermal production of human organism. In so doing, it is necessary to overcome heat inleak from the organism thermal centre which requires rather long cooling period.

There are known developments of devices whose operating principle lies in human brain cooling through upper air passages (Figs. 1 – 5) [29 – 36]. Such devices comprise catheters that are inserted into patient's nostrils into which cooled normal saline is poured or cooled air is blown. However, the main disadvantage of such devices is impossibility of their use with craniocerebral injuries, nasal bone fractures and respiratory diseases, which restricts considerably the areas of their application.

There are also developments of devices for human head cooling through the external skin cover (Figs. 6 – 12) [17 - 23]. These devices include cooling helmet for human head and refrigerating unit for cold carrier (air, water, alcohol solution, etc). However, it should be noted that up to now there is no experimental proof of human brain temperature reduction to the necessary temperature +30 ÷ 32°C with the aid of the above developments.

In the overwhelming majority of cases the existing equipment for human head cooling through the external skin cover includes large-size stationary devices based on compressor cooling units. Only 2 developments of devices are known that are based on thermoelectric cooling [26 – 28]: thermoelectric device in the form of a helmet for human head cooling (Fig. 11) and Olympic Cool-cap thermoelectric system for cooling of newborns (Fig. 12).

Thermoelectric device for human head cooling is made in the form of a motorcycle helmet (Fig. 11). Cooling helmet comprises 120 thermoelements connected thermally in parallel and electrically in series. Refrigerating capacity of this device is 200 W, but the main disadvantage of such development is large weight of cooling helmet - 9 kg, creating certain discomfort during use of this device in medical practice. Moreover, this device is a mere development, and no data is available on its medical test.

Unlike previous development, Olympic Cool-cap thermoelectric system for cooling of newborns [24, 25] (Fig. 12) is mass-produced and used in medical practice for prevention or considerable reduction of neurological disorders related to hypoxic ischemic encephalopathy of newborns. The device cooling helmet is composed of a cap (having a network of channels with water circulating from cooling device), cap holder and external insulation cap. The device assures a regular and controlled cooling of newborn child head to +32 °C. To maintain the necessary temperature of cooling helmet, the external cap is thermally isolated and copper foil clad [26, 27]. The minus side of this device is its large weight-size parameters, namely cooling unit dimensions are (132 × 44 × 57) cm, and its weight – 52 kg.

However, today there are no analogous thermoelectric devices for brain cooling of adults. Thus, in order to develop up-to-date portable devices for brain cooling of adults, it is necessary to determine the prospects of using thermoelectricity for human brain cooling.

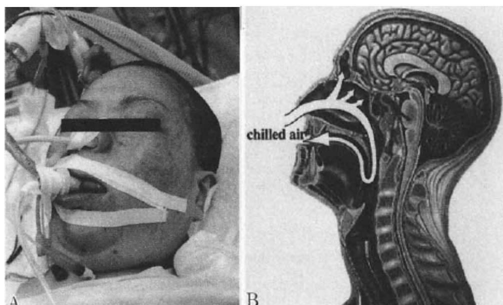

Fig.1. Device for human brain cooling through upper air passages (Japan) [29 - 31]

Fig.2. Quick hypothermia device (USA) [34]

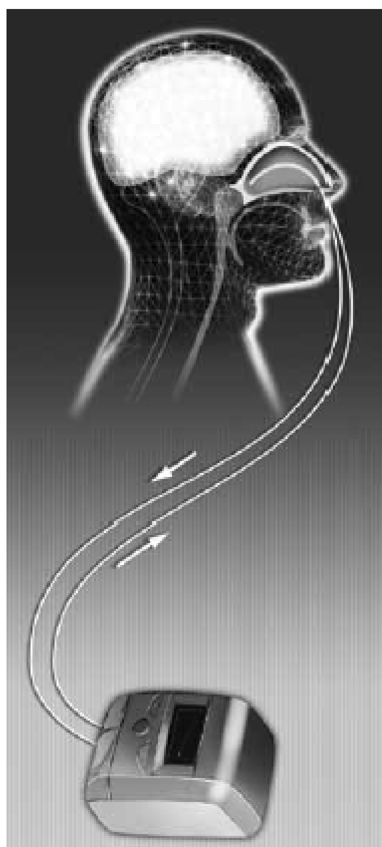

Fig.3. QuickCool intranasal system (Sweden) [35]

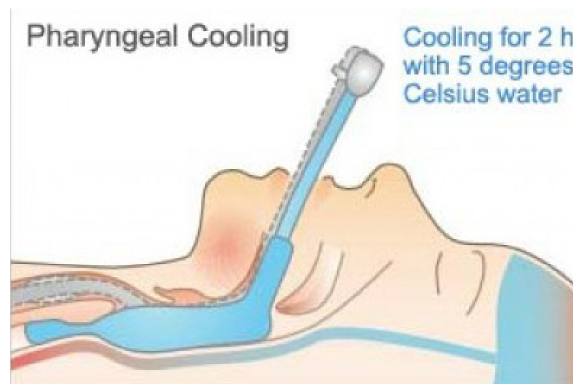

Fig.4. Pharyngeal cooling cuff (Japan) [36]

Fig.5. RhinoChill human brain hypothermia device (USA) [32, 33]

Fig.6. Curative hypothermia apparatus (Russia) [23]

Fig.7. "Kholod 2F" hypothermia device (Russia) [17 - 19]

Fig.8. Blanketrol- II craniocerebral cooling device (USA) [20]

Fig.9. CoolSystem cerebral hypothermia device for treatment of severe craniocerebral injuries [21]

Fig.10. Sovika GmbH Device for human head cooling (Germany) [22]

Fig.11. Helmet-shaped thermoelectric device for human head cooling (Turkey) [28]

Fig.12. Olympic Cool-cap thermoelectric system for cooling of newborns (USA) [26, 27]

Comparative analysis of currently available devices for head cooling is given in Table 1.

Table 1.

Comparative analysis of currently available devices for head cooling [17 – 36]

№	Device name	Weight, kg	Dimensions, cm	Power consumption, W	Refrigerating capacity, W	Manufacturing country	Note
Devices for human head cooling through upper air passages							
1.	Device for human brain cooling through upper air passages [29 – 31]	–	–	–	–	Japan	Development
2.	Quick hypothermia device [34]	–	–	–	–	USA	Development
3.	QuickCool intranasal system[35]	–	–	–	–	Sweden	Development
4.	Pharyngeal cooling cuff [36]	–	–	–	–	Japan	Development
5.	RhinoChill human brain hypothermia device [32, 33]	4.8	39×26×16	–	–	USA	Serial production
Devices for human head cooling through external skin cover							
6.	Curative hypothermia apparatus [23]	65	94 × 45 × 52	–	–	Russia	Development
7.	"Kholod 2F" hypothermia device [17 – 19]	–	–	–	–	Russia	Development
8.	Blanketrol- II craniocerebral cooling device [20]	67	43 × 43 × 95	–	–	USA	Serial production
9.	CoolSystem cerebral hypothermia device for treatment of severe craniocerebral injuries [21]	–	–	–	–	USA	Development
10.	Sovika GmbH human head cooling device [22]	–	–	–	–	Germany	Serial production
11.	Helmet-shaped thermoelectric device for human head cooling [28]	–	–	–	200	Turkey	Development
12.	Olympic Cool-cap thermoelectric system for cooling of newborns [26, 27]	52	132× 43× 57	500 – 700	–	USA	Serial production

On thermoelectric cooling efficiency

From the above analysis of works [17 – 36] it is seen that in the overwhelming majority of cases the existing equipment for human head cooling includes large-size stationary devices based on compressor refrigerating units. The average weight of such devices is 50 ÷ 70 kg with the volume of 0.2 ÷ 0.3 m^3, power consumption 500 – 700 W and refrigerating capacity nearly 200 W (Table 1). In so doing, the devices can be powered only from 110 ÷ 220 V of AC mains. This, in turn, restricts the use of such devices under non-stationary treatment conditions (for instance, in medical transport – automobiles, helicopters, airplanes, etc).

It can be easily verified that on the basis of thermoelectric cooling one can create a portable thermoelectric device for human head cooling that will have much lower weight-size characteristics as compared to existing analogs. To do this, we will perform simple calculation.

Let us consider a model of thermoelectric device for human head cooling (Fig. 13).

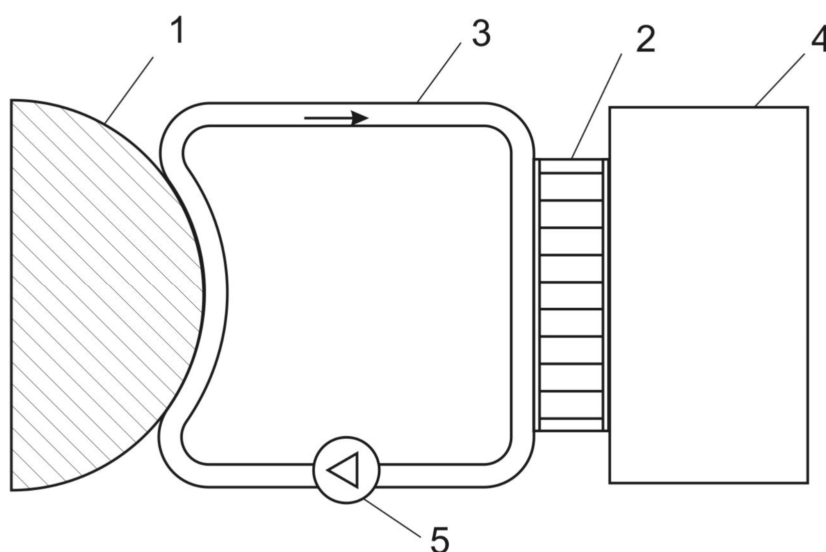

Fig.13. A model of thermoelectric device for human head cooling:
1 – human head, 2 – thermoelectric cooling system, 3 – liquid heat exchange system,
4 – liquid (or air) heat exchanger (радіатор), 5 – circulation pump.

From the medical requirements it is known [1 – 10] that minimum permissible temperature of human head surface is +2°C. The average ambient temperature in healthcare facilities, as a rule, is +20°C. Heat transfer from human head 1 to thermoelectric cooling system 2 is done by means of liquid heat exchange system 3. In so doing, heat transfer from thermoelectric cooling system 2 to environment can take place in two ways – liquid or air. For the best liquid heat exchangers temperature losses make 7 ÷ 8°C [41, 42], in the case of using the best air heat exchangers – 10 ÷ 20°C [41, 43]. With regard to losses, temperature difference on thermoelectric modules will be from $\Delta T \approx 30$°C with the use of both liquid heat exchange systems to $\Delta T \approx 45$°C with the use of liquid and air heat exchange systems. Best suited to this task are thermoelectric modules Altec - 011, specially developed by Institute of Thermoelectricity, that are characterized by increased value of maximum temperature difference [44]. Loading characteristics of such modules are given in Fig. 14.

From Fig. 14 it is seen that at given temperature difference on thermoelectric module $\Delta T \approx 30 \div 45$°C with optimal electric current the refrigerating capacity of one module will be $Q \approx 20 \div 30$ W. Hence it appears that to assure the above mentioned refrigerating capacity of device 200 W, it is necessary to have 7 – 10 pcs thermoelectric modules. With regard to heat exchange system the volume of such device will make 10 – 15 liters, and weight is 5 – 7 kg.

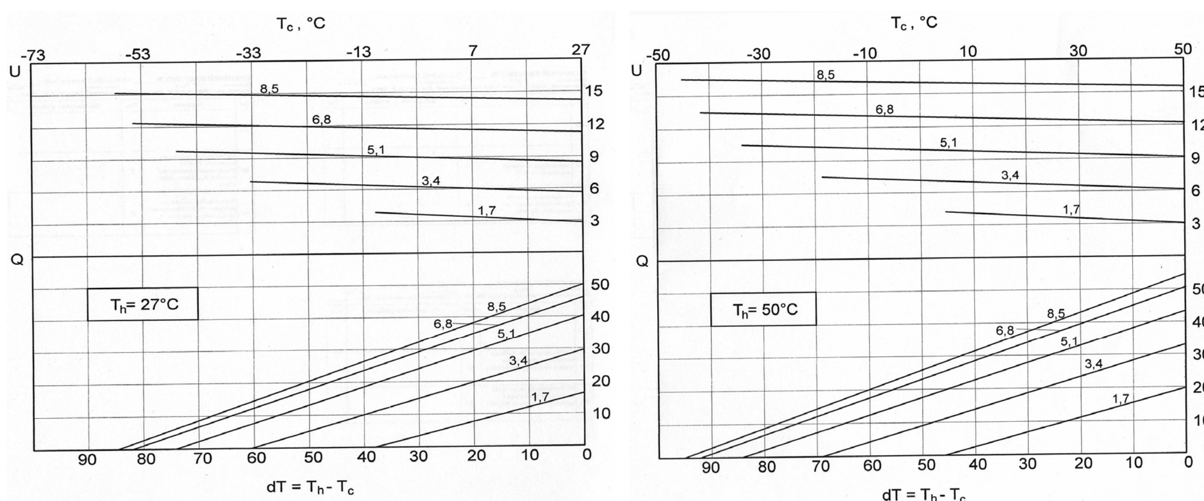

Fig.14. Load characteristics of thermoelectric modules Altec-011.

Moreover, thermoelectric cooling device can be easily adapted to power supply from the vehicle on-board mains 12 – 24 V DC. Thus, thermoelectric devices for human head cooling offer undeniable advantages over traditional compressor units (the weight and volume are 10 and 20 times lower, respectively, and power consumption is 2.5 – 3 times lower), providing the necessary refrigerating capacity 200 W.

When designing a device for human head cooling it is necessary to take into account the specific thermophysical processes in human organism. Investigations of human head cooling through external skin cover performed in [37 – 39] have shown that this method of human brain cooling is not efficient enough, since the temperature of near-surface brain layer is reduced only to +36°C. Besides, work [40] is known which demonstrates more efficient cooling of human brain (to +34°C) by cooling of neck in the area of passage of carotid arteries. It is evident that the use of both brain cooling methods will be most efficient. Therefore, for this purpose the device must comprise both head cooling helmet and neck cooling cuff.

The above analysis testifies that one can really create a portable thermoelectric device for human head cooling that will have lower weight and volume as compared to the existing analogs based on compressor refrigerating units. Such devices have a good potential for a wide practical use in medicine, which will increase the efficiency and quality of emergency medicine treatment in health care system.

Conclusions

1. Currently available devices for human head cooling (generally based on compressor refrigerating units) provide completely the necessary temperature conditions. However, large dimensions and high power consumption complicate their use under non-stationary treatment conditions (for instance, in medical transport – cars, helicopters, airplanes, etc).
2. It is established that one can really create a portable thermoelectric device for human head cooling that will have much lower weight-size characteristics (10 and 20 times lower weight and volume, respectively, as well as 2.5 – 3 times lower power consumption) as compared to the existing analogs based on compressor refrigerating units.
3. It is established that to increase the efficiency of human brain cooling, thermoelectric device must comprise both head cooling helmet and neck cooling cuff. Such devices can have a good outlook for emergency medicine (with blood strokes, heart attacks, cerebral circulation disorders, acute cardiovascular insufficiency, head injuries and human brain hypoxia).

References

1. V.A.Negovsky, *Reanimation and Artificial Hypothermia* (Moscow: Medgiz Publ, 1960), 302 p.
2. V.A.Bukov, *Cold and Organism. Issues of General Deep Cooling of Animals and Human* (Leningrad, 1964), 216 p.
3. V.M.Ugryumov, *Severe Closed Craniocerebral Injury* (Moscow: Medicine, 1974).
4. T.M.Darbinyan, A.N.Zirakadze, S.M.Zolnikov, P.Ya.Kintraya, B.A.Komarov, S.N.Kopshev, N.P.Kupin, and L.D.Chachava, *Artificial Hypothermia* (Moscow: Sov. Encyclopedia Publ, 1989).
5. E.I.Ivaschenko, Change in Constant Potential Level in the Brain of Patients with Acute Cerebrovascular Accident on Exposure to Local Craniocerebral Hypothermia During the First Hours of Blood Stroke, *Proc. of Laboratory of Age-Specific Physiology, Brain Research Institute, RAS* (Moscow, 1995), p. 23.
6. The Hypothermia after Cardiac Arrest Study Group. Mild Therapeutic Hypothermia to Improve the Neurologic Outcome after Cardiac Arrest, *NEJM* 364(8), 549 – 556 (2002).
7. M.N.Prandini, Filho A. Neves, A.J.Lapa, and J.N.Stavale, Mild Hypothermia Reduces Polymorphonuclear Leukocytes Infiltration in Induced Brain Inflammation, *Arq. Neuropsiquiatr*. **63**(3B), 779 – 784 (2005).
8. L.V.Usenko, A.V.Tsarev, Artificial Hypothermia in Modern Resuscitation, *General Resuscitation* **V**(1), 21 – 23 (2009).
9. A.M.Belous, V.I.Grischenko, *Cryobiology* (Kyiv: Naukova Dumka, 1994), 431 p.
10. O.A.Shevelev, A.V.Butrov, Curative Hypothermia Techniques in Intensive Therapy and Resuscitation, *Emergency Medicine* 3, 45 – 49 (2010).
11. S.N.Kopshev, *Craniocerebral Hypothermia in Obstetrics* (Moscow: Medicine, 1985), 111 p.
12. G.M.Savelyeva, R.I.Shalina, A.A.Smirnova, Zh.Yu.Kunyakh, O.P.Yevstratova, and M.A.Simukhina, Infantile Asphyxia. Complex Therapy with the Use of Craniocerebral Hypothermia, *Obstetrics and Gynecology*, 2015.
13. *Reference Book on Psychiatry, Second Ed. Revised and Enlarged, Ed. by A.V.Snezhnevsky* (Moscow: Medicine, 1985).
14. I.K.Sosin, G.A.Babiychuk, Ya.L.Gurevich, M.K.Filatov, and T.B.Zgonnikova, Clinical Results of Using Craniocerebral Hypothermia for Treatment of Addicts, *Cryobiology* 4, 36 – 41 (1990).
15. A.P.Chepkiy, A.I.Traschinsky, *Curative Hypothermia* (Kyiv: Zdorovya, 1969), 203 p.
16. A.M.Karaskov, V.N.Lomivorotov, V.L.Zelman, and V.G.Postnov, Brain Protection during Cardiosurgical Operations under Deep Hypothermal Circulatory Arrest, *Proc. of "Heart-Brain" Symposium at the Congress of Cardiologists and Cardiosurgeons of Siberian Federal District*, p.66 – 68.
17. B. Harris, P.J.D. Andrews, G.D. Murray, J. Forbes, O. Moseley. Systematic review of head cooling in adults after traumatic brain injury and stroke. Health Technology Assessment 2012; Vol. 16, No. 45.
18. O.Smirnov, Novel Method of Body Cooling (or Heating) and Device for Craniocerebral Hypothermia, *Biomedicine* 2,343 – 347 (1968).
19. O.Smirnov, Method for Efficiency Improvement of Air Hypothermia and Brain Cooling Device, *Biomedicine* 3, 257 – 260 (1969).
20. Cincinnati Sub-Zero. [Http://Www.Cszmedical.Com/].
21. O.A.Harris, C.R.Muh, M.C.Surles, Y.Pan, G.Rozycki, J.Macleod, et al., Discrete Cerebral Hypothermia in the Management of Traumatic Brain Injury: a Randomized Controlled Trial, *J Neurosurg* 110, 1256 – 1264 (2009).
22. *Patent US 20100168825 A1*, Device for Cooling a Body Part/ Ingrid Barbknecht.-2010.
23. http://www.cmed-plus.ru/atg.html.
24. L.I.Anatychuk, *Thermoelements and Thermoelectric Devices: Reference Book* (Kyiv: Naukova Dumka, 1979), 768 p.

25. E.A.Kolenko, *Thermoelectric Cooling Devices. 2-nd ed* (Leningrad: Nauka, 1967), 283 p.
26. "Cool-Cap System Gets FDA Nod". Medgadget.com. Retrieved 2009 – 10 – 13.
27. "Cool-Cap System – Children's Hospital – Scott & White – Central Texas". Sw.org. Retrieved 2009 – 10 – 13.
28. R.Ahiska, I.Guler, A.H.Yavuz, and A.Toprak, Fuzzy Logic Controlled Thermoelectric Brain Cooler, *J.Thermoelectricity* 2, 64 – 70 (2008).
29. K.Dohi, H.Jimbo, T.Abe, and T.Aruga, Positive Selective Brain Cooling Method: a Novel, Simple and Selective Nasopharyngeal Brain Cooling Method, *Acta Neurochirurg Suppl*. 96, 409 – 412 (2006).
30. A.Shuaib, R.Kanthan, G.Goplen, R.Griebel, H.el-Azzouni, H.Miyashita, et al., In-vivo Microdialysis Study of Extracellular Glutamate Response to Temperature Variance in Subarachnoid Hemorrhage, *Acta Neurochir Suppl* 67, 53 – 58 (1996).
31. K.Dohi, H.Jimbo, Y.Ikeda, K.Matsumoto, Pharmacological Brain Cooling (PBC) by Indomethacin; a Non-selective Cyclooxygenase (COX) Inhibitor in Acute Hemorrhagic Stroke, *Nosotchu* 22, 429 – 434 (2000).
32. G.Sung, M.Torbey, and A.Abou-Chebl, Rhinochill: a Novel Brain Hypothermia Delivery Device, *Neurology* 72, A75 (2009).
33. http://www.benechill.com.
34. http://eng.jhu.edu/wse/cbid/page/RHID-rapid-hypothermia-induction-device.
35. L.Covaciu, *Intranasal Cooling for Cerebral Hypothermia Treatment. PhD Thesis* (Uppsala: Uppsala University; 2010).
36. Y.Takeda, K.Fumoto, H.Naito, and N.Morimoto, Development of a Pharyngeal Cooling System that Enables Brain Temperature to be Immediately Reduced, *Crit Care Med* 37,506 (2009).
37. Kalpana Pathak, Nansen Yu, Andrew Shoffstall, Laura Zheng, Modeling Heat-Transfer of the Olympic Cool-Cap System, *BEE 453 Final Project*, p. 1 – 23.
38. F.E.M. Janssen, G.M.J. Van Leeuwen, and A.A.Van Steenhoven, Modelling of Temperature and Perfusion during Scalp Cooling, *Phys. Med. Biol*. **50**, 4065 – 4073 (2005).
39. Brian H. Dennis, Robert C. Eberhart, George S. Dulikravich, and Steve W. Radons, Finite Element Simulation of Cooling of Realistic 3-d Human Head and Neck, *J.Biomechanical Engineering*, January 2004.
40. E.Kelle, R.Mudra, C.Gugl, M.Seule, S.Mink, and J.Fröhlich, Theoretical Evaluations of Therapeutic Systemic and Local Cerebral Hypothermia, *J. Neurosci Methods* Apr. 15, 178(2):345 – 9 (2009). doi: 10.1016/j.jneumeth.2008.12.030. Epub 2009 Jan 9.
41. Heat Exchange Devices and Systems for Thermoelectricity, *Report on Research Work*: Institute of Thermoelectricity, 2012, 164p.
42. L.I.Anatychuk, A.V.Prybyla, The Effect of Heat Exchange Systems on the Efficiency of Thermoelectric Devices, *J.Thermoelectricity* **3**, 39 – 44 (2012).
43. L.I.Anatychuk, R.V.Kuz, and A.V.Prybyla, The Effect of Heat Exchange System on the Efficiency of Thermoelectric Air Conditioner, *J.Thermoelectricity* **1**, 75 – 81 (2013).
44. http://inst.cv.ua.

Submitted 10.07.2015.

ARTICLE PREPARATION RULES

The article shall conform to the journal profile. The article content shall be legible, concise and have no repetitions.

The article shall be submitted to the editorial board in electronic version.

The text shall be typed in text editor not lower than MS Word 6.0/7.0.

Page setup: "mirror margins"- top margin – 2.5 cm, bottom margin – 2.0 cm, inside – 2.0 cm, outside– 3.0 cm, from the edge to page header – 1.27 cm, page footer – 1.27 cm.

Graphic materials, pictures shall be submitted in color or, as an exception, black and white, in .opj or .cdr formats, .jpg or .tif formats being also permissible. According to author's choice, the tables and partially the text can be also in color.

The article shall be submitted in English on A4 paper sheets; the number of pages shall not exceed 12. By agreement with the editorial board, the number of pages can be increased.

To accelerate publication of the article, please adhere to the following rules:

- the authors' initials and names are arranged in the centre of the first page at the distance of 1 cm from the page header, font Times New Roman, size 12 pt, line spacing 1.2;

- the name of organization, address (street, city, postal code, country) – indent 1 cm below the authors' initials and names, font Times New Roman, size 11 pt, line spacing 1.2, center alignment;

- the title of the article is arranged 1 cm below the name of organization, in capital letters, semi-bold, font New Roman, size 12 pt, line spacing 1.2, center alignment. The title of the article shall be concrete and possibly concise;

- the abstract is arranged 1 cm below the title of the article, font Times New Roman, size 10 pt, in italics, line spacing 1.2 ,center alignment;

- key words are arranged below the abstract, font Times New Roman, size 10 pt, line spacing 1.2, justified alignment. The title "Key words" – font Times New Roman, size 10 pt, semi-bold;

- the main text of the article is arranged 1 cm below the abstract, indent 1 cm, font Times New Roman. size 11 pt, line spacing 1.2, justified alignment;

- formulae are typed in formula editor, fonts Symbol, Times New Roman. Font size is "normal" – 12 pt, "large index" – 7 pt, "small index" – 5 pt, "large symbol" – 18 pt, "small symbol" – 12 pt). The formula is arranged in the text, centre aligned and shall not occupy more than 5/6 of the line width, formulae are numbered in round brackets right;

- dimensions of all quantities used in the article are represented in the International System of Units (SI) with the explication of the symbols employed;

- figures are arranged in the text. The figures and pictures shall be clear and contrast; the plot axes – parallel to sheet edges, thus eliminating possible displacement of angles in scaling;

- tables are arranged in the text. The width of the table shall be 1 cm less than the line width. Above the table its ordinary number is indicated, right alignment. Continuous table numbering throughout the text. The title of the table is arranged below its number, center alignment;

- references should appear at the end of the manuscript. References within the text should be enclosed in square brackets. References should be numbered in order of first appearance in the text. Examples of various reference types are given below.

- L.I. Anatychuk, *Thermoelements and Thermoelectric Devices: Handbook* (Kyiv: Naukova Dumka, 1979), p.766. (Book)
- T.M. Tritt, Thermoelectric Phenomena, Materials, and Applications, *Annual Review of Materials Research* **41**, 433 (2011). (Journal paper)
- U. Ghoshal, *Proceedings of the XXI International Conference on Thermoelectrics* (N.Y., USA, 2002), p. 540. (Proceedings Conference)

The article should be supplemented by:

• letter from the organization where the work was performed or from the authors of the work applying for the publication of the article;

• information on the author (authors): last name and initials; full name and postal address of the institution where the author works; academic degree; position; telephone number; E-mail;

• author's (authors') photo in color or, as an exception, in black and white. With the number of authors more than two their photos are not given;

• author's application to the following effect:

We, the undersigned authors, … transfer to the founders and editors of "Journal of Thermoelectricity" the right to publish the article…in Ukrainian, Russian and English. This is to confirm that the present publication does not violate the copyright of other persons or organizations.

Date Signatures